



Generation of 3D representative volume elements for heterogeneous materials: A review

Swantje Bargmann^{a,*}, Benjamin Klusemann^{b,c}, Jürgen Markmann^{c,d}, Jan Eike Schnabel^c, Konrad Schneider^e, Celal Soyarslan^a, Jana Wilmers^a

^aChair of Solid Mechanics, University of Wuppertal, Germany

^bInstitute of Product and Process Innovation, Leuphana University of Lüneburg, Germany

^cInstitute of Materials Research, Materials Mechanics, Helmholtz-Zentrum Geesthacht, Germany

^dInstitute of Materials Physics and Technology, Hamburg University of Technology, Germany

^eInstitute of Continuum Mechanics and Material Mechanics, Hamburg University of Technology, Germany

ARTICLE INFO

Article history:

Received 10 August 2017

Received in revised form 6 February 2018

Accepted 6 February 2018

Available online 26 March 2018

Keywords:

Representative volume element

RVE generation

Microstructure

Polycrystal

Matrix-inclusion composite

Nanocomposite

Metamaterial

Porous media

Lamellar

Fiber reinforced composite

Nanoporous metal

Open cell structure

Closed cell structure

Aggregate

Agglomerate

ABSTRACT

This work reviews state of the art representative volume element (RVE) generation techniques for heterogeneous materials. To this end, we present a systematic classification considering a wide range of heterogeneous materials of engineering interest. Here, we divide heterogeneous solids into porous and non-porous media, with $0 < \text{void volume fraction} < 1$ and void volume fraction = 0, respectively. Further subdivisions are realized based on various morphological features. The corresponding generation methods are classified into three categories: (i) experimental methods targeting reconstruction through experimental characterization of the microstructure, (ii) physics based methods targeting simulation of the physical process(es) responsible for the microstructure formation and evolution, and (iii) geometrical methods concentrating solely on mimicking the morphology (ignoring the physical basis of the microstructure formation process). These comprise of various mathematical tools such as digital image correlation, tessellation, random field generation, and differential equation solvers. For completeness, relevant up-to-date software tools, used at various stages of RVE generation – either commercial or open-source – are summarized. Considered methods are reviewed based on their efficiency and predictive performance with respect to geometrical and topological properties of the microstructures.

© 2018 The Authors. Published by Elsevier Ltd. This is an open access article under the CC BY-NC-ND license (<http://creativecommons.org/licenses/by-nc-nd/4.0/>).

Contents

1. Introduction	323
2. Non-porous solids	325
2.1. Polycrystals	325
2.1.1. Grain microstructures	327
2.1.2. Lamellar microstructures	334
2.1.3. Other polycrystalline microstructures	338

* Corresponding author.

E-mail address: bargmann@uni-wuppertal.de (S. Bargmann).

<https://doi.org/10.1016/j.pmatsci.2018.02.003>

0079-6425/© 2018 The Authors. Published by Elsevier Ltd.

This is an open access article under the CC BY-NC-ND license (<http://creativecommons.org/licenses/by-nc-nd/4.0/>).

2.2.	Bicontinuous composites	338
2.2.1.	Microstructure reconstruction from experimental data	339
2.2.2.	Physics based microstructure generation	339
2.2.3.	Geometrical methods	339
2.3.	Matrix-inclusion composites	341
2.3.1.	Microstructure reconstruction from experimental data	342
2.3.2.	Physics based microstructure generation	345
2.3.3.	Geometrical methods	346
3.	Porous solids	354
3.1.	Fabrics	354
3.1.1.	Woven structures	355
3.1.2.	Non-woven structures	360
3.2.	Agglomerates	361
3.2.1.	Cellular structures	362
3.2.2.	Matrix-dilute pore systems	368
3.3.	Aggregates	370
3.3.1.	Microstructure reconstruction from experimental data	370
3.3.2.	Physics based microstructure generation	370
3.3.3.	Geometrical methods	371
4.	Summary	371
	Acknowledgements	372
	References	372

1. Introduction

Materials science is often concerned with understanding structure–property relationships in materials. At a small enough scale, all natural and synthetic materials are heterogeneous. That is, they are either composed of domains of different materials, such as a composite, or the same material in different states, such as a polycrystal. The properties of a heterogeneous material depend on microstructural features (adapting [1]), which are often controlled by fabrication, alloying, and processing, e.g., heat treatment, for instance:

- properties of the constituent(s),
- geometry of the constituent(s): their distribution, orientation, shape and volume fraction,
- nature and characteristics of the interfaces (resp. interphase) between different constituents.

In this work, we discuss modeling related issues pertaining to the second one, that is, the geometric arrangement of the constituents. If the geometry and/or properties of the constituents govern the mechanical response of the heterogeneous materials, we refer to them as materials with microstructure or microstructured materials. The scale at which the microstructure emerges simply relates to the average domain size. It does not necessarily have to be the microscale. It can equivalently be at nanometer-, millimeter-, or meterscale, see Fig. 1.

The classical continuum approximation does not account for microstructural details within the material. Micromechanics, on the other hand, allows a detailed modeling of the internal structural arrangement of a heterogeneous material by treating each constituent as a continuum. While doing so, it relies on the concept of a representative volume element (RVE) or repeating unit cell. In unit cells, the microstructure is approximated as periodic. However, the majority of microstructures in engineering materials are non-periodic.

An RVE is a material volume whose effective behavior is representative of that of the material as a whole [2]. Defining an RVE is possible for statistically homogeneous materials. The macroscopic stress and strain fields at a material point, as resultants of a boundary value problem (at the microscale), devising the fictitious homogeneous medium, are the averages of the microscopic stress and strain fields over any RVE centered at the same point. For this to hold, the condition of separation of scales $\mathcal{L}^\mu \ll \mathcal{L}^{\text{RVE}} \ll \mathcal{L}^{\text{M}}$ is to be satisfied [3–5], where \mathcal{L}^μ , \mathcal{L}^{RVE} and \mathcal{L}^{M} denote the characteristic length associated with the microstructural features (e.g., inclusion size in matrix-inclusion composites or ligament diameter in bicontinuous composites), the RVE size and the characteristic size of the macroscopic body or the length scale associated with the fluctuations of the mechanical loading applied. Although the size of the RVE is irrelevant for a homogeneous fictitious material, in order to satisfy statistical representativeness the RVE must contain a sufficiently large volume for heterogeneous materials. The correct size of an RVE has been discussed in many contributions (cf. [5–20]) and strongly depends on the characteristics of the material such as number of phases and their spatial distribution.

There exist various analytical or computational techniques for the aforementioned averaging, which is also known as homogenization, from micro to macro. In the following, we provide the reader with a synopsis of each approach. For further details, the reader is referred to, e.g., [2–5,21–34], among others.

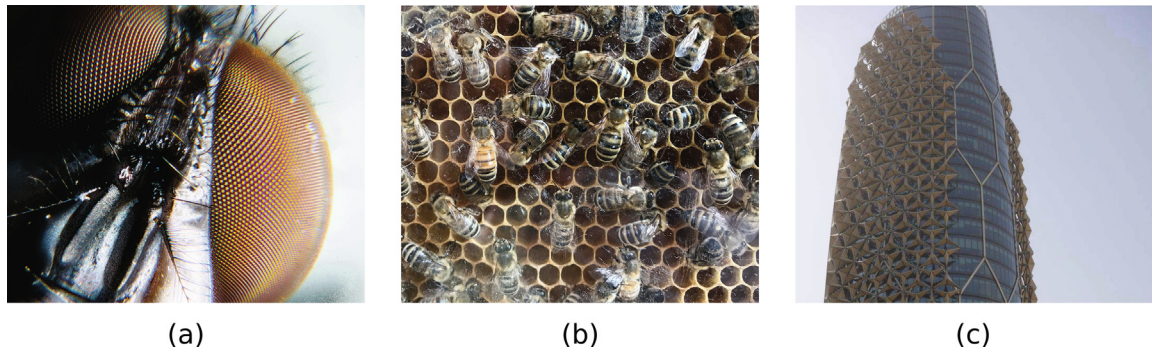


Fig. 1. Functional structures with a honeycomb microstructure across scales: (a) compound eye of an insect, arranged in a micrometer scale honeycomb cell structure, (b) wax honeycomb built by honey bees, (c) high rise buildings (Al Bahr tower, Abu Dhabi, UAE) composed of honeycomb outer shell where an edge of each honeycomb is several meters long.

Analytical methods encapsulate effective-medium approximations which are also referred to as mean field methods. Initial representatives of this class of methods were proposed before the advent of computers. Due to the closed-form nature of the sought solution of the boundary value problem, these methods consider the immersion of smooth inclusions in an infinite matrix or an effective medium with simple microstructural information such as volume fraction and mean morphology of the inclusion. In this sense, an a priori satisfaction of the conditions of an RVE is implied. Thus, an explicit account for a finite- and ideally minimal-sized RVE is not given.

Mean field homogenization techniques commonly rely on Eshelby's average strain concentration tensor estimation for a system consisting of an ellipsoidal inclusion embedded into an infinite medium [35], which is valid if interactions among inclusions can be neglected. As the concentration of the embedded inclusions increases, their interactions should be considered. This is for instance realized in the Mori-Tanaka mean field scheme by taking the effective field acting on each heterogeneity as the field average over the matrix [36,37]. For the same reason, the self-consistent method, which was originally proposed for aggregates of crystals by [38,39], replaces the problem of the interaction among many particles by the problem of one particle embedded in an unbounded effective domain [40,41].

Since mean field approaches are devoid of a requirement for domain discretization they constitute highly efficient candidates for successive homogenization over several separated scales for microstructures with complex hierarchical organization. Thus, among other studies, they have been successfully applied to polycrystals [42,43], porous materials [44–47], particulate composites such as concrete [48–51], fiber reinforced composites [52–54], bicontinuous composites [55], or the ultrastructure of mineralized tissues [56] and interfaces [57,58].

However, these methods have to be used with care, as e.g. classical two-phase mean field homogenization methods based on spherical phase shapes may have constraints with respect to phase volume fractions and may only deliver successful results if low volume fractions are considered. For example, they are not quantitatively accurate for general situations, e.g., for 50% void volume fractions negative effective bulk and shear moduli may be produced by the self-consistent method, or, an unbounded effective bulk modulus may be predicted for rigid inclusions of any volume fraction [2,22]. In addition, all methods relying on the dilute solution, as in the case of Mori-Tanaka scheme, lack normal-shear coupling [2]. Moreover, these methods only allow relatively simple microstructural features to be modeled, and thus, mostly deliver crude approximations falling short of accurately reflecting, especially the strongly fluctuating, microfields at the RVE scale [21]. This shortcoming renders the understanding of damage and failure mechanisms as a challenge, calling for significant mathematical expenditures and intricacies.

A more direct approach to this problem is provided by computational homogenization approaches which comprise finite elements, fast Fourier transform methods¹, finite volumes, finite differences, boundary elements, etc. In computational homogenization methods, one cannot a priori claim the required size of the RVE. Since, for computational efficiency purposes, the smallest volume element size which allows computation of effective properties such as elastic stiffness, conductivity (thermal or electrical), permeability (magnetic or fluid) or mean survival time, without reverting to a modeling attempt of the whole material domain, is sought for, the identification of the RVE size relies on an a posteriori analysis based on a process referred to as successive sample enlargement.

In addition to RVEs of existing microstructured materials, there is a major need for RVEs of materials which have not yet been manufactured. More and more often, computational mechanics scientists work hand in hand with materials scientists in the development of tailor-made microstructured material systems. Having understood large portions of the influence of microstructural parameters on the mechanical response, nowadays it is possible to optimize custom-designed

¹ The fast Fourier transform (FFT) requires data to be sampled in a regular spaced grid. Thus, FFT-based approaches, first introduced in [59], allow a direct use of digital images carried out from experimentally developed 2D or 3D micrographs without an additional need for meshing. Moreover, they inherently use periodic boundary conditions which are known to provide converged effective properties at smaller volume element sizes. These make FFT methods especially attractive among other numerical methods [59,60].

microstructures. New materials are developed based on controlled variations of the microstructure - aiming at new categories of materials with optimized mechanical properties (e.g., improvement of strength-to-weight and stiffness-to-weight ratios of lightweight construction materials), multi-functionalized or even (in the case of metamaterials) unnatural properties. In these cases, there is a strong demand for the automatic generation of geometries in order to systematically vary geometrical features of the microstructure for a high throughput of simulations as neither sample production nor conducting experiments for a large number of specimens is an option.

This study reviews methods of generating 3D RVEs of microstructured materials for computational homogenization.² Computational homogenization relying on volume discretization can account for complex morphological microstructural features of the constituents in addition to various nonlinearity sources. Besides providing the user with a full resolution of the local fields at the RVE scale, computational techniques make it possible to investigate various localization, damage and failure mechanisms which are not accessible by mean field approaches.

A systematic treatment of the methods of generating 3D RVEs for microstructured materials requires undertaking a challenging task: a classification of heterogeneous materials. Since heterogeneous materials exist in countless forms and compositions, our attempt is inevitably pragmatic and practical rather than exhaustive. Our classification assumes the “space filling property” of the material domain to be the basis and divides the heterogeneous materials into non-porous and porous media,³ see also Fig. 2.

Non-porous materials are further divided into non-matrix materials, bicontinuous and matrix-reinforcement composites. Following the conventional practice, matrix-inclusion composites are split into particle and fiber reinforced composites.

Porous materials are divided into three main groups: fabrics, agglomerates and aggregates. With agglomerates, we take into account porous materials which are consolidated, existing as rigid, macroscopic bodies whose dimensions exceed those of the pores by many orders of magnitude. In contrast, aggregates represent unconsolidated, non-rigid, relatively loosely packed assemblages of individual particles where the particles are surrounded by a network of inter-particle pores. Agglomerates are stiff and withstand tensile loads whereas aggregates cannot unless interparticle cohesion is explicitly considered. Fabrics formed of a network of natural or artificial fibers can also withstand tensile loads but they are in general more flexible than agglomerates. Open and closed-cellular material systems and materials with dilute voids are considered as agglomerates whereas granular media, such as soil, sand, gravel or crushed stone are classified as aggregates. Fabrics are divided into two groups: woven and non-woven. The former is made by weaving, braiding, stitching or knitting whereas for the latter, fibers can be bonded mechanically as well as chemically or physically into a random web structure.

In the following, we review various RVE generation techniques separately for each class of microstructures. The corresponding generation methods are divided into three different approaches:

- experimental methods targeting reconstruction through experimental characterization of the microstructure,
- physics based methods targeting simulation of the physical process(es) responsible for formation of the microstructure, and
- geometry based methods concentrating solely on generation of the morphology (ignoring the physical basis of microstructural formation process).

This review provides a state of the art overview and benefits workers in various disciplines including mechanics, materials science, engineering, chemistry, physics, geophysics, biology, mathematics, and computer science who are conducting research on microstructured materials.

2. Non-porous solids

2.1. Polycrystals

A polycrystal is a space-filling solid composed of multiple grains, yielding a mosaic like microstructure, see for instance the two examples in Fig. 3. Grains, which are identical except in lattice or crystallographic orientation, are separated from

² The reader should note that any approximation to the effective medium property, either via analytical or computational homogenization techniques, should strictly satisfy upper and lower rigorous bounds. Theoretically, relating the statistical characterization of the structure to the changes in the effective response, an infinite set of correlation functions is required for an exact prediction of effective properties [61,4]. This set of correlation functions is known only for a few special cases [62]. Thus, usually the bounds are constructed using lower-order probability functions. The simplest of these bounds are due to Voigt [63] and Reuss [64] and they relate effective moduli to only the volume fraction and individual moduli of the constituents. In this sense, these bounds are one-point bounds. Based on variational formulations, Hashin and Shtrikman developed more accurate two-point bounds for effective elastic moduli [65]. Even tighter bounds for effective elastic moduli of random composites exist which devise three-point probability functions, e.g. the three-point Beran-Molyneux and three-point Milton-Phan-Thien bounds can be derived [66–68]. Finally, extension of the Hashin and Shtrikman variational principles to the case of nonlinear composites can be found in Willis and Talbot [69] and Ponte Castañeda [70]. In the present study, a detailed account of statistical characterization of the microstructural morphology and associated microstructure reconstruction methods for random heterogeneous materials is not given. For a comprehensive and recent survey of these methods, the reader is referred to [568].

³ Another classification of heterogeneous materials could be based on the number of constituents, which results in division into single- and multi-phase materials. In such a classification, pores are considered to be an additional phase. However, their penetrability, inability to transfer energy and propagate mechanical waves or mechanical loading and the emerging infinite mechanical property contrast have crucial consequences on the morphological properties of heterogeneous media. Thus, this line of classification is not pursued.

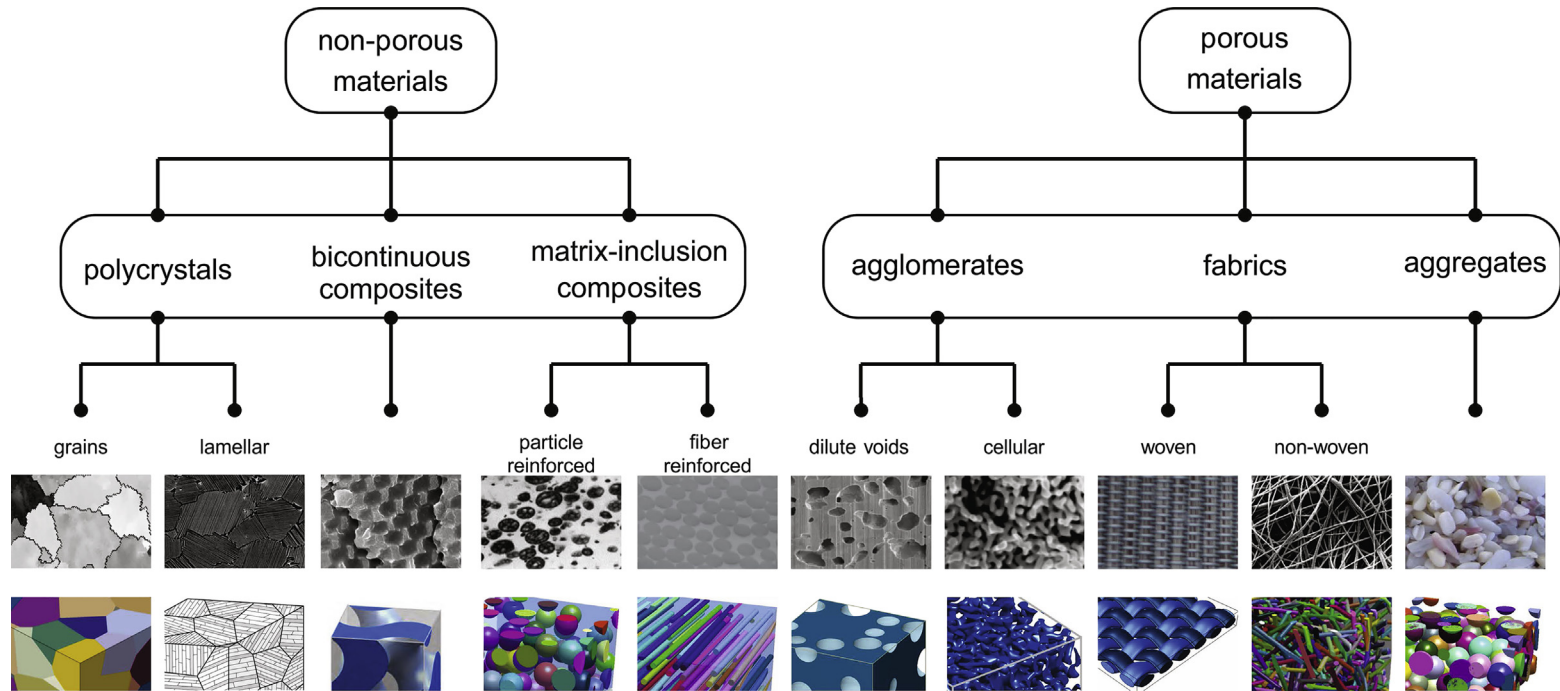


Fig. 2. Classification of heterogeneous solids into porous and non-porous media. Based on various morphological features, these categories are further subdivided into different microstructure classes. See acknowledgements for information on figure copyrights and permissions to reprints.

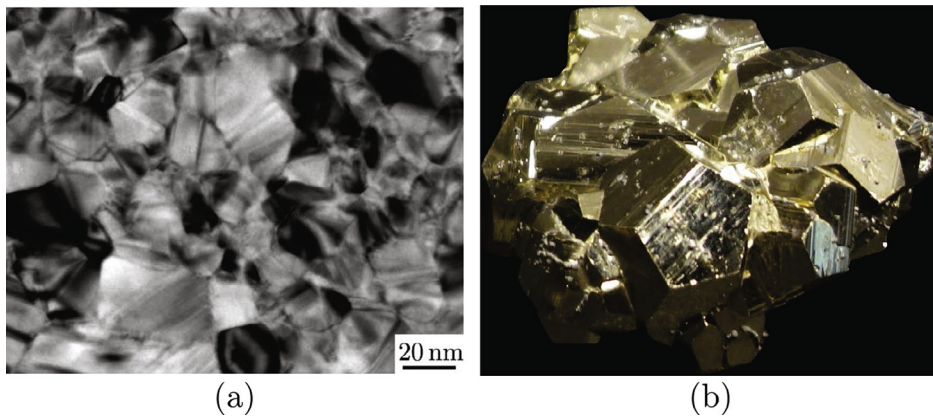


Fig. 3. Polycrystalline microstructures. (a) Nanocrystalline gold film. (b) Rock (mineral pyrite, FeS_2) with a crystal structure of a pentagonal dodecahedron. Specimen dimensions: $10 \text{ cm} \times 14 \text{ cm} \times 5 \text{ cm}$.

each other by grain boundaries. Famous representatives of materials showing a polycrystalline microstructure at some length scale are metals, their alloys as well as ceramic materials, but also rocks and ice. In the following, we discuss RVE generation for grain microstructures (Section 2.1.1) as well as lamellar polycrystals (Section 2.1.2). Other polycrystalline microstructures are briefly addressed in Section 2.1.3.

2.1.1. Grain microstructures

2.1.1.1. Microstructure reconstruction from experimental data. While it is tempting to consider an RVE reconstructed from experimental data to be a “perfect” or true microstructure representation, one has to keep in mind that like all experimental measurements, 3D reconstruction approaches are also subject to some uncertainty, thus, inaccuracies emerge. Moreover, disadvantages of experimentally generated RVEs are: (i) a full representation of the investigated structure with all details may complicate the identification of the significant features and (ii) access to (in most cases very expensive) equipment is needed. Whenever the material is still under development, RVEs need to be generated computationally. In addition, if a large number of, e.g., structural variations of one material needs to be examined, physics or geometry based RVE generation tools are the only reasonable options as experimental techniques are exceptionally time and cost intensive.

The experimental techniques to be employed depend on the heterogeneous material at hand and also on the kind of microstructural information of interest. Among other factors, such as specimen geometry, available equipment, time, etc., an optimal specimen contrast is of importance - if possible at material preserving conditions.

In general, one can distinguish between two types of experimental techniques that allow to study the 3D structure of a material:

- serial sectioning techniques (Fig. 4(a)) and
- imaging based on transmissive radiation, also known as tomography (Fig. 4(b)).

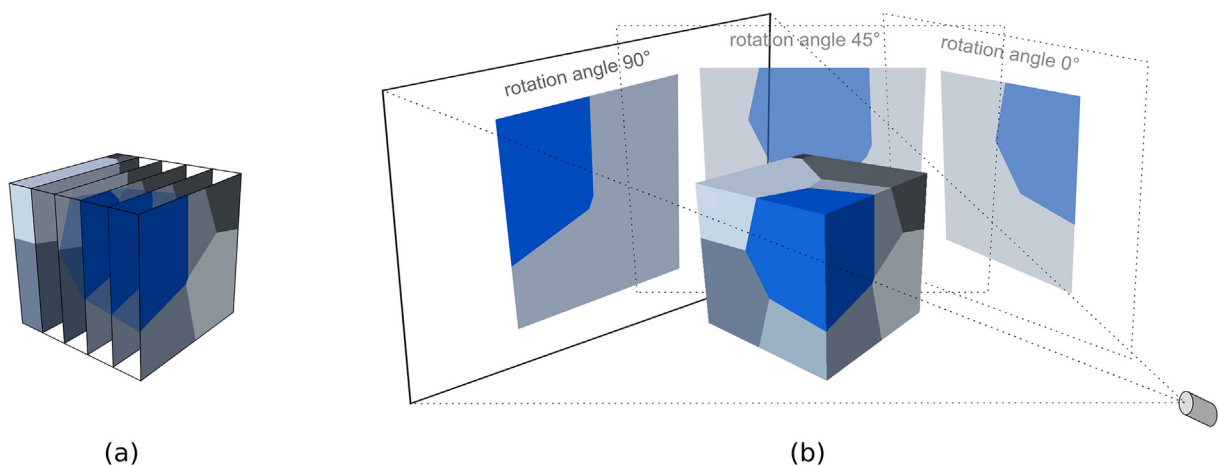


Fig. 4. Techniques for reconstructing a grain microstructure from experiments: (a) serial sectioning and (b) projection based imaging.

This classification is in fact closely related to the distinction between destructive and non-destructive methods, as serial sectioning in general involves mechanical cutting or etching of the specimen and imaging based on transmissive radiation is in principle non-destructive.

To fully characterize the microstructure of polycrystals, considering features such as size, shape, spatial orientation and distribution of grains and grain boundaries as well as crystallographic properties, elaborate experimental studies are necessary.

Imaging of morphologies on the micro- and nanoscale requires experimental techniques with high spatial resolution. In general, 2D microscopy methods provide the best resolution in a submicron range for optical microscopy. Scanning electron microscopy (SEM) and transmission electron microscopy (TEM) are able to resolve a few nanometers and lower length scales. 2D grain structures obtained from such methods can be used to construct 3D RVEs by expanding the structure into the third dimension, resulting in columnar formations, compare, e.g., [71,72]. For materials with coarse grain sizes, often referred to as oligocrystals, and specimen geometries in which the thickness is smaller than the grain diameter, this approach gives reasonable results but cannot be used to model polycrystalline structures which fully extend into three dimensions.

To fully recover 3D information from 2D imaging, serial sectioning techniques [73–78] are utilized. These are based on a sequential removal of thin layers from the bulk material of the specimen accompanied by imaging of the newly generated surfaces. These 2D images are then post-processed and used to recover 3D microstructure information.⁴ Post-processing involves aligning the slices in a stack and image enhancement (e.g., noise reduction, contrast enhancement) to facilitate segmentation, i.e., identification of the microstructure constituents.

As the slice thickness in general is greater than the in-plane image resolution, serial sectioning techniques can have a highly anisotropic resolution, and the missing information between the 2D images needs to be interpolated as depicted in Fig. 4(a). The simplest interpolation method is a straightforward interpolation of intensity values inbetween the slices. However, this results in blurring of edges which can obscure microstructure information [80,81] and is, thus, only suitable for microstructures that exhibit low curvature in the slicing direction. The most common alternative approach is shape-based interpolation [82] which requires identification of structure edges in the 2D slices but provides more accurate results than conventional intensity interpolation [83]. Different variants of shape-based interpolation are discussed in the literature, compare, e.g., [79–81,83,84], and the choice always depends on the studied material and the microstructure topology.

Image segmentation is further needed to identify and match microstructure constituents over adjacent slices. Manual image segmentation is still common, however, debilitatingly time consuming. Therefore, extensive research is carried out on algorithmical image segmentation, including algorithms working on already interpolated 3D sets [85,86] or ones in which the segmentation in 2D is the basis for a subsequent interpolation [87,88]. Depending on the studied material and the microstructure topology, very different combinations of interpolation techniques and segmentation algorithms are necessary and no “one-size-fits-all” approach exists.

Serial sectioning techniques are destructive, due to the mechanical removal of material slices inbetween the imaging steps. Non-destructive techniques such as confocal microscopy (which is based on optical sectioning [89]) exist, but are only applicable to certain material systems, e.g., transparent or highly porous materials (Section 3.2.1.1).

3D reconstruction of metallic materials using serial sectioning dates back to the idea of Forsman [90] in 1918 who sectioned a ferrous pearlite sample to obtain a series of 2D micrographs. Continuous improvement of instruments and methodologies since then has led to approaches allowing for a detailed view on nano- and microstructures.

Achievable resolutions in serial sectioning of polycrystals depend on the chosen slicing and imaging techniques. The most commonly available method is a combination of polishing or grinding and optical microscopy [91,92]. For optical microscopy, the resolution limit is commonly stated to be in the range of a few hundred nanometers. However, it is difficult to exactly control the removed material thickness in polishing and grinding. Furthermore, sequential material removal is extremely time-consuming and requires grinding and cutting techniques tailored to the studied material system. Therefore, different attempts at automation exist, e.g., Spowart et al. [78] introduced a fully automated robotic serial sectioning device which provides a resolution from 10 μm down to 0.1 μm slice thickness. Layers are removed by chemical etching, a method mostly suitable for metallic materials that has to be carefully tailored to the material at hand.

Modern advanced approaches are often based on focused ion beam (FIB) serial sectioning and imaging via scanning electron microscopy (SEM) [93–100]. State of the art dual-beam FIB/SEM machines carry out the sectioning and imaging steps within the same unit, superseding time-intensive manual transfers between machines and allowing fully automated serial sectioning. However, full automation is always limited to a single material system. For the characterization of another material with a similar (or even the same) underlying geometric structure, the parameters for the FIB/SEM tomography have to be adjusted.

The use of SEM imaging allows for increased resolution as compared to optical microscopy and also offers the possibility to utilize different types of imaging modes in addition to classical imaging based on backscattered electrons. Electron backscatter diffraction (EBSD), for instance, provides crystallographic information such as crystallographic orientation or lattice parameters [94,96,101–104] and energy-dispersive X-ray spectroscopy (EDS) allows for spatial element mapping and, therefore, the identification of different phases in the material (if they have a different chemical composition). To be able to utilize these techniques, the SEM has to be equipped with additional detection units.

⁴ Data acquired in z-direction is not continuous, as the region between the 2D images has to be interpolated, see e.g. [79]. To reduce interpolation errors, care has to be taken both during the experiment (slice thickness, specimen drift, etc.) and during post-processing (constituent identification, alignment of slices, etc.).

3D experimental characterization of polycrystalline materials is extremely laborious. Not only the conduction of experiments is extremely time consuming but also post-processing the huge amount of data generated requires tremendous effort. Reconstruction of 3D structures from serial sectioning, even when employing automated techniques, requires trained operators and different algorithms and methods for different materials. Groeber et al. [103,104] introduced a methodology that directly extracts the necessary information for an RVE from EBSD data. Newest developments provide complete software packages to process the huge amount of EBSD data, e.g., DREAM.3D [105].

Therefore, approaches combining experimental information with computational microstructure generation are developed. Statistical stereological techniques [106,107] are, roughly speaking, the experimental counterpart to computationally generated statistically similar RVEs discussed in Section 2.3.3 and gain insight into 3D aspects from statistical extrapolation of 2D plane cuts through the specimen. Zhang et al. [108] used data from serial sectioning to harvest statistical quantities like face numbers, volume and surface area of the grains. This information can then feed the generation process of artificial microstructures. Brahme et al. [109] used EBSD maps of only two orthogonal cross-sections as input for an involved algorithm to computationally generate polycrystalline microstructures.

Experimentally reconstructing materials on a much smaller scale is possible by atom probe tomography [110]. Single atoms are detached from the surface of a needle-shaped sample by extremely high electric fields and field gradients. This “electromagnetic lens” enables a precise localization of the evaporated atom that in turn can be identified by mass spectrometry. Recent approaches in combination with atomistic simulations, such as molecular statics, even reach a resolution on the atomic scale [111]. The reconstructed volumes are rather small (ca. 100 nm x 100 nm x 100 nm), which may yield useful RVEs for nanostructured systems in the future.

Serial sectioning techniques applicable to single-phase polycrystalline materials are destructive and, thus, cannot be used to carry out in situ studies or compare microstructures before and after any kind of experimental treatment. 3D imaging with transmissive radiation, such as X-rays or electrons, in principle offers this possibility. These tomographic techniques collect a series of 2D projection images of the microstructure under a variety of angles (a so called tilt series), compare Fig. 4(b). Using, e.g., algebraic reconstruction techniques, these 2D projections are computationally combined to reconstruct a 3D image of the material’s microstructure [102,112–114], see also Fig. 5.

The resolution of such a reconstruction directly depends on the number of projections in the tilt series as well as the range of tilt angles used. Ideally, projections over a range of 360° would be used. Due to experimental limitations, most reconstructions include artifacts resulting from missing information due to a limited tilt range [117].

In typical X-ray tomography (μ CT) setups [118–120], contrast in the projection images results from different degrees of X-ray absorption in different material regions. The degree of absorption is primarily a function of the electron density which correlates to the atomic number z . In single-phased polycrystals, however, the atomic number does not vary between different grains, making z contrast imaging impossible for all but a few specific crystalline materials (e.g., polycrystalline Al [115], where the grain boundaries were decorated with Sn which has a different X-ray adsorption as compared to Al, see Fig. 5). Even in cases like this, diffraction effects can significantly reduce contrast in these techniques.

However, it is possible to use X-ray diffraction [121] for imaging of grain structures based on contrast resulting from crystal size and orientation as employed in EBSD for surface measurements or differential-aperture X-ray microscopy (DAXM) allowing subsurface microstructure characterization [122–124]. The comparatively recently developed and not yet widely available high-energy X-ray diffraction microscopy (3DXRD) [125] and X-ray diffraction contrast tomography (DCT) [113] combine classical tomographic principles with diffraction measurements to reconstruct 3D grain shapes and orientations. With these methods also in situ studies of, e.g., grain growth and morphology evolution during deformation are possible [126]. These methods, however, rely on expensive laboratory equipment and high quality radiation sources which often are not readily accessible.

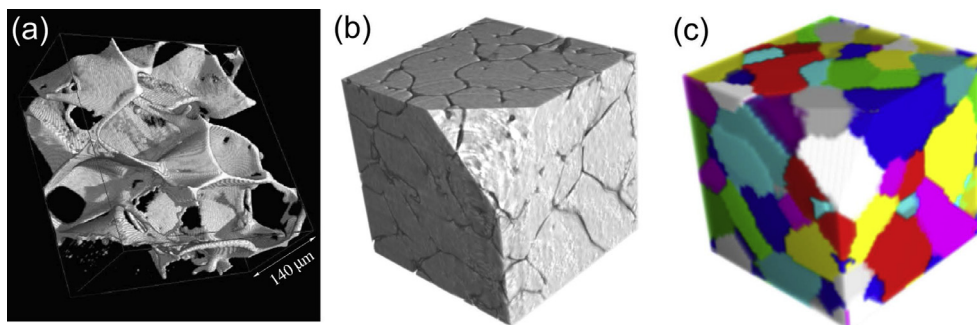


Fig. 5. Different stages of a tomographic 3D reconstruction of a polycrystalline aluminum microstructure with tin-decorated grain boundaries. (a) Grain boundary network made visible in X-ray attenuation contrast by tin-decoration. Artifacts due to incomplete decoration are visible. The tomographic data of a cubic volume element (b) served as a base for an algorithm which assigned each part of the volume inside the cube to its corresponding grain by a grain identification (c) and a consecutive phase field simulation procedure in order to treat residual unassigned volume ((a): Metallurgical and Materials Transactions A, Quantitative characterization of the three-dimensional microstructure of polycrystalline Al-Sn using X-ray microtomography [115], 35, 2004, 1953–1961, Döbrich et al. (original copyright notice as given in the publication in which the material was originally published). With permission of Springer. (b) and (c) reprinted from [116], with permission).

Even if using state of the art equipment, compromises need to be made in imaging accuracy, as increased spatial and angular resolution reduces the temporal resolution and vice versa [127]. Furthermore, these methods are highly sensitive to strain gradients in the material which significantly reduce their accuracy [113]. Spatial resolution in X-ray imaging using high quality synchrotron radiation is limited by beam size and precision of sample and/or detector movement. As X-ray diffraction produces additional signals for every illuminated grain, the sample size is limited in a way such that only a small number of grains is crossed by the incoming X-ray beam in order to be able to separate their contributions to the diffraction signal [113]. Possible specimen size is further limited by the radiation energy and the material of interest. For example, high energy X-rays from typical synchrotron sources can only penetrate specimens with a thickness of up to 4 cm for aluminum [127], 1 mm for steel [127] or several μm for gold.

Using coherent X-ray diffraction imaging (CDI), extremely high resolutions can be achieved [128] by measuring and directly inverting the specimen's diffraction pattern. For crystalline materials, especially Bragg CDI is of interest, as this method does not only allow to image the 3D shape of a single crystal but also the strain field within the crystal [129–131]. For best resolution, the crystals need to be smaller than the X-ray beam, so it is especially interesting for single nanocrystals, resulting in resolutions of a few ten nanometers, but with the potential for significant improvement [128,129] and, thus, giving insight into defect structures and deformation mechanisms at small scales.

Expensive laboratory equipment is required to obtain the needed data on the nano- and microscale and each method is limited to a certain range of length scales by the imaging resolution and not all methods are equally suitable for all types of materials and morphologies. In general, experimental RVE generation is so time and labor-intensive that only few samples can be investigated, often not enough for statistical analysis. In this case, systematically generated RVEs as presented in Section 2.1.1.3 are needed.

The open source software package Object Oriented Finite Element 3D (OOF3D) from the United States National Institute of Standards and Technology, an enhancement of the software OOF2 [132] to 3D, allows for RVE generation for microstructured materials (with strong focus on crystalline materials) based on experimental micrographs. The software package includes “methods for segmenting images, creating meshes of complex geometries, solving PDE's using finite element models, and visualizing 3D results” [133]. OOF is based on an image-based, adaptive meshing technique. For this, a data structure on the digitized image is built. OOF creates a FE-mesh which reflects the shape of the different phases by preserving a well-formed, space-filling mesh. The generated meshes can be used for further calculations in OOF and can also be exported to other finite element programs such as ABAQUS.

Remark on boundary conditions: For certain FE simulations, one might want to apply periodic boundary conditions which generally necessitate a periodic RVE. However, experimentally determined RVEs are never periodic for polycrystals. For non-periodic RVEs, one can apply approximate periodic boundary conditions [134–136].

2.1.1.2. Physics based microstructure generation. The most demanding approach of artificially generating polycrystalline microstructural information is the simulation of the actual physical process of grain formation and grain growth. All simulations are to a certain extent driven by minimization of the grain boundary energy. Various methods can be found in the literature, all describing the underlying physics of solidification and grain structure evolution.

The vertex method or dynamic vertex method, suggested by Kawasaki et al. [137], models the formation of polycrystalline patterns by reducing the complexity of a polycrystalline microstructure as it only considers points (vertices), rather than curved grain boundaries and is, therefore, the simplest physics based method. During the evolution process, these vertices move and, as a consequence, dictate the formation of the grains. Their movement is described by the equations of motion. Typically, these equations are derived from a potential function $\mathcal{F}(\mathbf{r}) = \int_{GB} \gamma(\mathbf{r}) da$ which is an integral over the grain boundaries and solely depends on the position \mathbf{r} . γ is the grain boundary energy density. \mathcal{F} acts as a driving force for the movement. Since the process is modeled as purely dissipative, a Rayleigh dissipation function $\mathcal{R}(\mathbf{v}, \mathbf{r})$ is introduced. Via the Lagrange formalism, the equations of motion are given by

$$\frac{\partial \mathcal{F}(\mathbf{r})}{\partial \mathbf{r}} + \frac{\partial \mathcal{R}(\mathbf{r}, \mathbf{v})}{\partial \mathbf{v}} = \mathbf{0}. \quad (1)$$

By discretizing the grain boundaries via triangles and evaluating the integrals, discrete forms of (1) are obtained and solved. However, as straightforward as this seems, various difficulties of discretizations or topological changes of the microstructures and treatment of vertices at junctions arise such as non-planar grain boundaries (if faces are defined by more than three vertices) [138] or vertex merging (collapsing nodes) and detaching grains [139,140]. Mora et al. [141,142] followed a different approach employing a vertex model by investigating the normal grain growth. In their model, the driving force \mathbf{F} is proportional to the grain boundary energy and related to the vertex velocity \mathbf{v} via $\mathbf{v} = m_{\text{eff}} \mathbf{F}$. The mobility m_{eff} depends on the position of the vertex (triple line, quadruple junction, etc.) which allows a more straightforward treatment of quadruple junction mobilities.

Whereas the vertex method takes only vertices into account, Brakke's surface evolver method [143] considers the entire grain boundary. This approach solves the entire system by a gradient descent method to minimize the overall surface energy (which might include surface tension, gravity or other quantities), where the surface energy itself is computed via surface integrals. The surface is represented by simplicial complexes, i.e., a union of triangles in the simplest case. Furthermore, geometrical constraints (e.g., position of vertices) can be taken into account. In the employed idealized model no disturbance of

grain growth by impurities or obstacles is allowed. The definition of the driving force follows $F = \gamma \left[\frac{1}{r_1} + \frac{1}{r_2} \right]$ with the grain boundary free energy γ (an isotropic constant) and the two principal surface curvatures r_1 and r_2 . Computing the gradient at a vertex yields the force which converts into a velocity vector for realizing the motion of the surface. Wakai et al. [144] computed an initial configuration with 1000 grains based on a constant volume constraint and a default mobility with arbitrary packing of grains with periodic boundary conditions. They assumed that a preliminary computation of grain formation can be replaced by Voronoi tessellated configurations since similar steady state structures were obtained by utilizing initially uniform grains (constant volume constraint). In the grain growth simulation, the mean grain size increased due to a decreasing number of non-convex grains and a subsequent minimization of the grain boundary energy. The network of grain boundaries approached a steady structure after incubation. The identification of the parabolic law in grain growth could only be identified in a region of a maintained steady structure.

Increasing the methods' complexities, cellular automata and Monte Carlo methods model the entire 3D grain geometry based on voxels resp. regular grids. Especially cellular automata have proved to be versatile and computationally efficient. The general concept dates back to the 1940's and is successfully applied to a variety of different fields whereas its application to microstructure evolution only developed during the past two decades. An overview of its historical evolution and the diverse applications (not only in materials science) can be found in [145–147]. The following brief summary of the basic ideas of cellular automata is motivated from a materials science perspective, thus, not detailing further applications.

Cellular automata predict the discrete spatial and temporal evolution of a given quantity based on a grid of cells. The current state of each cell is governed by a problem specific set of state variables (e.g., crystal orientation or dislocation density) that evolve as a function of the previous state(s) of the respective cell and its neighbors. The cells are usually arranged in a regular grid enabling simple identification of nearest neighbors (and, if required, next nearest neighbors), but random grids are possible as well [148,149].

The evolution of state variables from one discrete time step t to the next time step $t + \Delta t$ is described by so-called transformation (or switching) rules whose complexities depend on the underlying physics. The concept of these transformation rules is easiest explained by a simple 1D system with only one state variable κ that can either be $\kappa = 1$ or $\kappa = 0$ in each cell. Assuming that the current state $\kappa_{t=t_0+\Delta t}^x$ of a cell x is only a function of its previous state $\kappa_{t=t_0}^x$ and the previous states of its nearest neighbors $\kappa_{t=t_0}^{x+1}$ and $\kappa_{t=t_0}^{x-1}$, results in $2^3 = 8$ possible combinations of states of the three adjacent cells at $t = t_0$. Each of these combinations may trigger the investigated cell to switch its state either to 1 or to 0, resulting in $2^8 = 256$ possible transformation rules for this simple binary system. One possible transformation rule is shown in Fig. 6. In 3D, this would result in $2^7 = 128$ possible combinations of states and, thus, $2^{128} \approx 10^{38}$ possible transformation rules, if only nearest neighbors are considered. For simulation of, e.g., grain growth or recrystallization processes, the transformation rules are obviously more complex and usually functions of a possibly large number of physically motivated state variables. However, once a suitable transformation rule is derived, the state of the next time step is simply determined by evaluating it for every cell. This evaluation may be deterministic (like in the example system) or probabilistic (e.g., based on the switching probability of a cell in recrystallization simulations, see, e.g., [150]). Consequently, cellular automata are efficient. Fig. 7

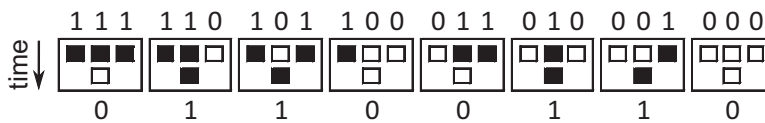


Fig. 6. Cellular automata: One of the 256 possible transformation rules of a 1D binary system. Empty square: state $\kappa = 0$; filled square: state $\kappa = 1$.

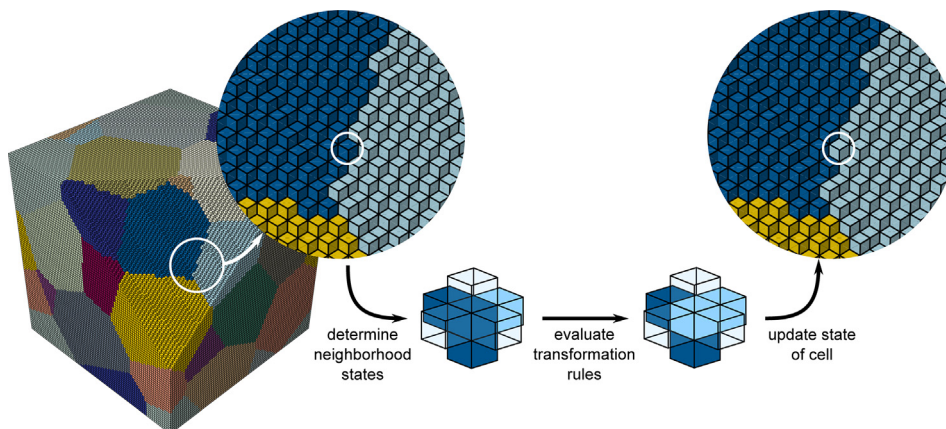


Fig. 7. Cellular automata: Schematic illustration of sequential state variable update based on the states of nearest neighbor cells.

schematically illustrates a sequential process as it might appear in a 3D grain growth simulation. So far, cellular automata are successfully used to model solidification (e.g., [151–157]), (dynamic) recrystallization (e.g., [148–150,158–167]), phase transformations (e.g., [158,168,167]) and grain growth (e.g., [148,169–171]).

Further, cellular automata work well alongside finite element simulations. On one hand, finite element results (e.g., from crystal plasticity simulations) may be mapped to a cellular automaton to serve as initial state for, e.g., microstructure evolution [146,164,165,168,172]. On the other hand, an evolved microstructure from a cellular automaton may be (re)transferred to a finite element geometry for further investigation [165,164,172], enabling sequentially coupled simulations.

Monte Carlo methods are based on the idea of repeated random sampling resulting in a quantitative probabilistic analysis of possible grain structures. A large number of simulations is run, each time using a different set of random states (crystallographic orientations) of a probability function. This leads to a set of possible outcomes providing information on the probability of occurrence of various grain distributions and with this a statistical distribution of the expected values (i.e., final grain distributions). Monte Carlo methods are well suited for grain growth simulations because they properly reproduce the statistical behavior of the microstructure. They only take into account the energy (and by this the thermodynamics of atomic interactions). Therefore, the grain evolution solely depends on the grain topology. Usually, a regular grid or discrete lattice such as voxelized cubes is used. The initial grain microstructure is then mapped onto the voxelization via their crystal orientations. Each grain is represented by a set of neighboring voxels with the same orientation. Grain boundaries are distinguished by two neighboring voxels with different crystal orientations. For each voxel, the energy is calculated based on its present crystallographic orientation and those of its neighbors. Subsequently, the voxel's crystallographic orientation is changed based on a probability function and the free energy is updated. Such an orientation switch is only admissible if the net energy change of the entire system is negative. Thus, the global energy decreases which corresponds to a curvature change of the grain boundary.

Anderson et al. [173] suggested a Monte Carlo approach based on an energy which incorporates nearest-neighbors or nearest-neighbor-plus-next-nearest-neighbor voxels that form the grain boundary. The authors investigated annealing treatment of polycrystalline materials and were able to produce formations remarkably similar to experimental findings of metals and ceramics subjected to grain growth. Furthermore, a power law describing the underlying kinetics was identified. Radhakrishnan et al. [174] examined grain growth in 0.5Mo-Cr-V steel in heat-affected zones (due to welding) and possible influences of temperature gradients. Those gradients are easily incorporated in simulations by spatial variations of mobilities of the voxels.

The most sophisticated common physics based method is the phase field method - an approach which solves interfacial problems and is frequently used to model grain evolution processes or solidification. General information on phase field methods is found in [175,176], for example. The key idea is to incorporate a diffuse interface between material phases. Possible boundary conditions between different subdomains are replaced by partial differential equations of phase evolution and additional (phase) field variables enter the system of unknown variables. The phase field often has two distinct values (0 and 1) in each of the phases. Its transition between phases can be smooth or sharp, while always possessing a finite width. This circumvents a direct treatment of grain boundaries which reduces the modeling effort and computational time. Consequently, even complex and large grain morphologies can be generated. Most frequently, microstructure evolution is investigated for metals [177–182], see also Fig. 8. Especially the grain growth during solidification is of great interest [178,183–186]. Typically, two phase-field approaches, both based on a large number of non-conserved phase fields, are applied: (i) the continuum phase field approach assumes phase fields to be independent; (ii) in multi-phase field approaches, the phase fields are constrained by the assumption that they represent volume fractions and, therefore, the sum of the phase fields equals 1 everywhere. Examples for the application of multi-phase field approaches are found in [183] and of the continuum phase field approach in [178]. Moelans et al. [185] compared the two approaches showing that both result in equally viable and remarkably similar outcomes.

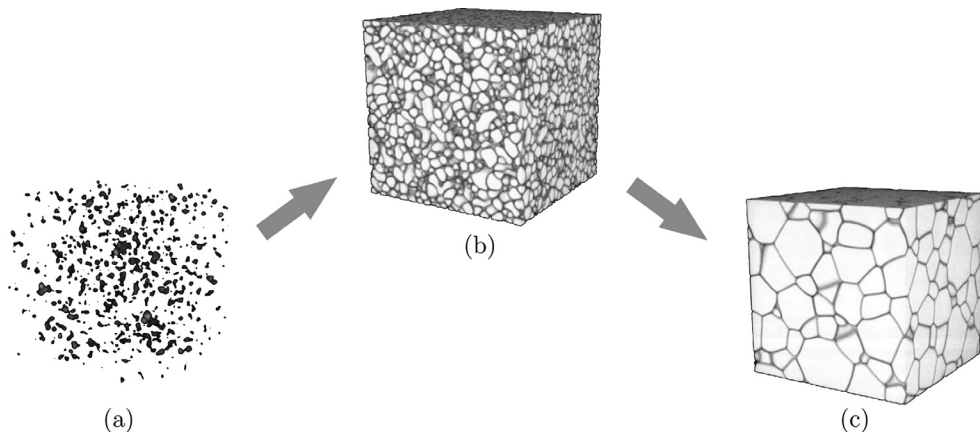


Fig. 8. Microstructure evolution of grain growth simulation using the phase field method at different simulation times: (a) beginning with no crystallized grain, (b) intermediate state with 5945 grains, (c) solidified state with 217 grains. Reprinted from Acta Materialia, 50(12), Krill III and Chen, Computer simulation of 3-D grain growth using a phase-field model [178], 3059–3075, Copyright (2002), with permission from Elsevier.

As an example of the general procedure of a phase field method, the continuum phase field approach followed by Krill et al. [178] is briefly summarized in the following. It is based on the minimization of the total free energy [187]. Ideal polycrystals with specified uniform mobilities and energies are assumed. The total free energy, which depends on the simulation time t , reads

$$F(t) = \int_V f_0(\eta_1(\mathbf{r}, t), \eta_2(\mathbf{r}, t), \dots, \eta_Q(\mathbf{r}, t)) + \sum_{q=1}^Q \frac{\kappa_q}{2} [\nabla \eta_q(\mathbf{r}, t)]^2 d\mathbf{r}. \quad (2)$$

The position in space is denoted by \mathbf{r} . A set of Q continuous order parameters η_q describes the local free energy contribution f_0 of the individual grains. κ_q are positive constants associated with the grain boundary energy whose contribution enters via the square gradient of the order variables. In this example, the order parameters η_q correspond to the local orientation of the grains and act as phase field variables ranging from 0 to 1. They are treated independent of each other classifying this method as a continuum phase field approach. Adjacent grains are defined by different η_q values. Depending on the material, a large number of order variables might enter the model at increased computational costs. The exact formulation of the local free energies is conducted in a way such that the total free energy is minimized, if the field variables reach the value 1 in one grain. Subsequently, a thermodynamic driving force is educible that minimizes the grain boundary area resp. increases the average grain size. The temporal evolution of the total free energy is described via a time-dependent Ginzburg-Landau type of equation, allowing the incorporation of material specific grain boundary mobilities. The computation of the order parameters at every node of the discretized domain at every time step is carried out iteratively. Initial conditions for the simulation mimics a super cooled liquid by assigning very small random values to each order parameters such that $|\eta_q| < 0.001$. This liquid then crystallizes in the course of the simulation time (see Fig. 8) until the local free energy densities f_0 reaches a minimum value, i.e., when only nodes at grain boundaries significantly contribute to the total free energy.

Linking experiments to simulations, Demirel et al. [188,189] combined gradient-weighted moving finite elements with topological reconnections on the evolving mesh to simulate the microstructure formation. Good agreement between the EBSD data and the grain growth simulations is stated.

Furthermore, Rios et al. [190] compared grain size distributions generated by the phase field method, the evolver method, the vertex and Monte Carlo approaches with experimental grain size distributions determined by serial sectioning. Good agreement between the different simulative approaches and the experimental data was found.

2.1.1.3. Geometrical methods. State of the art geometrical methods for generating polycrystalline microstructures are Voronoi tessellations. The resulting geometric setting possesses very similar properties to actual polycrystals: all Voronoi regions, which are interpretable as the grains, are convex polyhedra and space filling. Voronoi tessellations have a wide range of applications naturally originating from computational geometry. Good overviews of Voronoi tessellation algorithms and applications are given by, e.g., Aurenhammer [191], Preparata [192] and Okabe et al. [193]. Because of their convexity and space filling properties, Voronoi tessellations are quite popular to mimic polycrystals in general [194–198] or for specific materials such as metals [199–202], ceramics [203–206], rocks [207,208], or ice [209–211].

A Voronoi tessellation is a partitioning of a domain of arbitrary dimension n (for generating RVEs only $n = \{2, 3\}$ is of interest) into convex, polygonal regions based on distances between points. The points are often called germs, seeds or nucleation points and are specified before the generation process starts. They are combined in the set

$$\mathcal{G} = \{\mathbf{g}_1, \dots, \mathbf{g}_m\}, \quad \mathbf{g}_i \in \mathbb{R}^n. \quad (3)$$

Every point in space $\mathbf{x} \in \mathbb{R}^n$ is associated with the nearest germ \mathbf{g}_i . Thus, all points within a region (called Voronoi cell) are closer to the associated germ than to any other germ, see Fig. 9. Voronoi cells i are described by j corner points $\mathbf{p}_i^{(j)}$ or

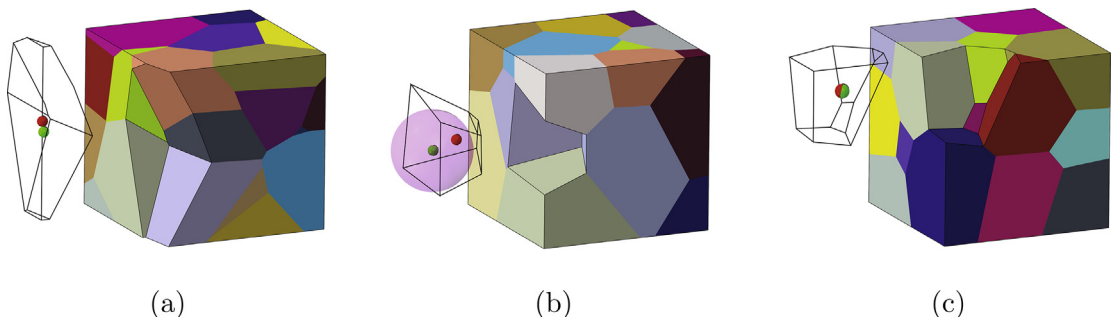


Fig. 9. RVEs with Voronoi tessellations based on different germ generation methods (20 germs). In each RVE one Voronoi region is extracted and its germ (green ball) and midpoint of the cell (red ball) are depicted. (a) Random germs approach. (b) Hardcore germs with hardcore radius 0.15 (30% hardcore volume fraction). Germs are placed via generation of non-intersection spheres (depicted in purple). Germs correspond to center of those spheres. (c) Centroidal Voronoi tessellation which enforces that germs and geometrical midpoints of the Voronoi cells coincide. It requires the most effort but yields the most realistic representation of grain microstructures.

intersections of half-spaces defined by a scalar $d_i^{(j)}$ and the normalized direction vector $\mathbf{n}_i^{(j)}$. Due to the convex nature of half-spaces and the fact that the regions are intersections of the half-spaces, all Voronoi cells are convex.⁵

The classical concept uses totally randomly positioned germs. This is also known as Poisson-Voronoi tessellation because the germs are generated with an underlying Poisson point process. However, a standard Voronoi tessellation generated from randomly placed germs is a rather coarse approximation for polycrystalline materials. In such a microstructure, the grain size distribution deviates from experimental findings [115,200]. Almost degenerated Voronoi regions that show rather extreme aspect ratios are also problematic. Furthermore, the average number of neighboring cells in a Poisson-Voronoi tessellation might be unrealistically large for polycrystalline materials⁶ [103,196].

Alternatively, there are several ways to restrict the randomness of germ positions. The hardcore Voronoi tessellation generates germs via random placements of non-intersecting spheres [199,201]. Germs then coincide with the center of those spheres, see Fig. 9(b). A requirement for the grains \mathbf{g}_i is

$$|\mathbf{g}_i - \mathbf{g}_j| \geq 2r \quad \forall i \neq j \quad (4)$$

with the hardcore radius r . Physically speaking, the hardcore process is motivated by a minimum size of viable grains during the grain-structure formation process. The minimal grain volume is $V_{G_{\min 3D}} = \frac{4}{3}\pi r^3$. As a result, the Voronoi cells are more regular without degenerated grains. With the gained advantage comes the challenge of generating a sphere placement. It is straightforward to utilize random sequential adsorption methods to place the non-intersecting spheres. However, a sphere volume fraction of approximately 35% is not exceeded with this method, limiting the number of Voronoi cells which can be generated for a fixed RVE volume and hardcore radius.

Another frequently used approach is a centroidal Voronoi tessellation, see Fig. 9(c). Here, germs and geometrical midpoints (centers of mass) of the Voronoi cells coincide [214]. To achieve such a Voronoi tessellation type, either regular germ patterns need to be utilized (honeycomb) or iterative approaches are necessary. Those iterative methods often start with randomly placed germs and successively reposition the germs to computed Voronoi cell midpoints. The resulting Voronoi cells are even more regular than the ones from the hardcore tessellation but still show a certain randomness.

The most involved germ generation approach is the so called Laguerre-Voronoi tessellation [197,215]. This approach assigns different weights or radii to each germ individually which can be fed by experimental measurements. Therefore, this method offers a good possibility to mimic experimental data via a Voronoi tessellation.

In computational homogenization, periodic RVEs have the advantage of minimizing the RVE size. A periodic Voronoi tessellation is established by copying the original germs around the RVE, see Fig. 10. The periodization requires 8 copies in 2D and 26 copies in 3D. This copying and subsequent new computation of the Voronoi tessellation results in increased computational costs. It does, however, not alter the beneficial properties of an always terminating Voronoi tessellation process. Even for a small Voronoi tessellation, the number of Voronoi cells significantly increases due to the periodization. Furthermore, very small cells near the RVE corners might lead to degenerated volumes. This can be avoided by moving the window of the RVE within the large window, see Fig. 10. Fig. 11 depicts different Voronoi tessellations for the 3D case. With computer resources and efficient software available today, the generation of these models is a matter of minutes.

Voronoi tessellations conform to real microstructures in terms of topology (distribution of faces, edges and vertices) [216,217]. One reason for the good agreement with experimental findings might be the parallelism to an isotropic grain growth starting from the germs with a constant growth velocity. From a computational viewpoint, some major advantages of Voronoi tessellations are that Voronoi tessellations are analytically well-defined and a generation process always succeeds. In the last few decades, stable and fast software emerged. Some of the most popular are QHULL by Barber et al. [218], VORO++ by Rycroft et al. [219] or NEPER by Quey et al. [201]. NEPER is well suited for generating Voronoi based polycrystalline RVEs. Various capabilities from including experimental data (grain-by-grain data, grain size distributions), utilizing multiscale microstructures (lamellar or n-scale tessellation) up to the subsequent regularization and discretization of the RVEs are covered.

In addition to Voronoi tessellation, simple approaches which do not require special tessellation exist. Those generate regular morphologies in a straightforward manner: Raabe et al. [220] utilized a voxelization combining the generation of geometric information and meshing in one step. Starting from a regular grid-like mesh, grain properties are assigned to the individual voxels (or Gauss points). Zhao et al. [221] and Ritz et al. [222] approached the problem in a more sophisticated way by introducing regularly assembled dodecahedral grains. Due to the regular arrangement, generation and discretization of the RVE is rather simple. However, these approaches have the drawback of poorly representing the varying shape and size distributions of the grains.

2.1.2. Lamellar microstructures

Lamellar microstructures can be obtained in numerous alloy systems (e.g., PbSn, TiAl, FeC, AlCu, CuAg) by alloying (e.g., near eutectics or eutectoids) and/or appropriate heat treatment. Prominent examples of commercial structural materials with lamellar microstructures are pearlitic steels, titanium aluminides and two-phase titanium alloys.

⁵ Dual to a Voronoi tessellation is the Delaunay triangulation. The edges of the triangulation define the normals of the faces of the boundary of Voronoi cells.

⁶ Average number of neighboring grains: e.g., 12.1 in Fe [108], 12.48 in Al-Sn alloy [212], 12.9 in nickel-base superalloy IN100 [213], but 15.5 for a microstructure generated by Poisson-Voronoi tessellation [103,144].

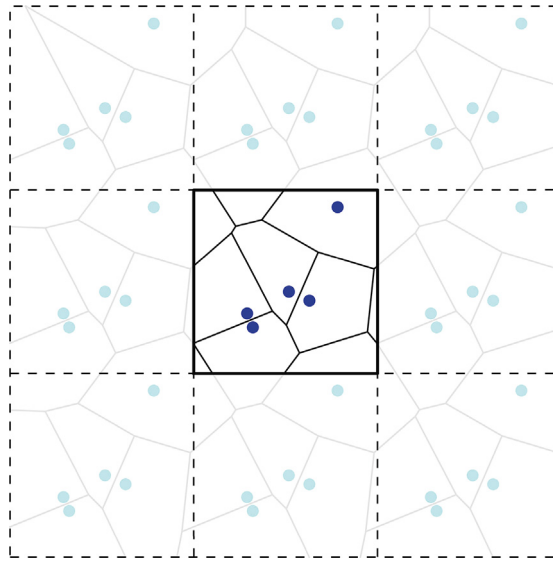


Fig. 10. A periodic Voronoi tessellation of a 2D RVE with 5 randomly placed germs. The germs are copied 8 times and distributed around the intended RVE. A Voronoi tessellation of all germs results in a periodic tessellation of the central RVE.

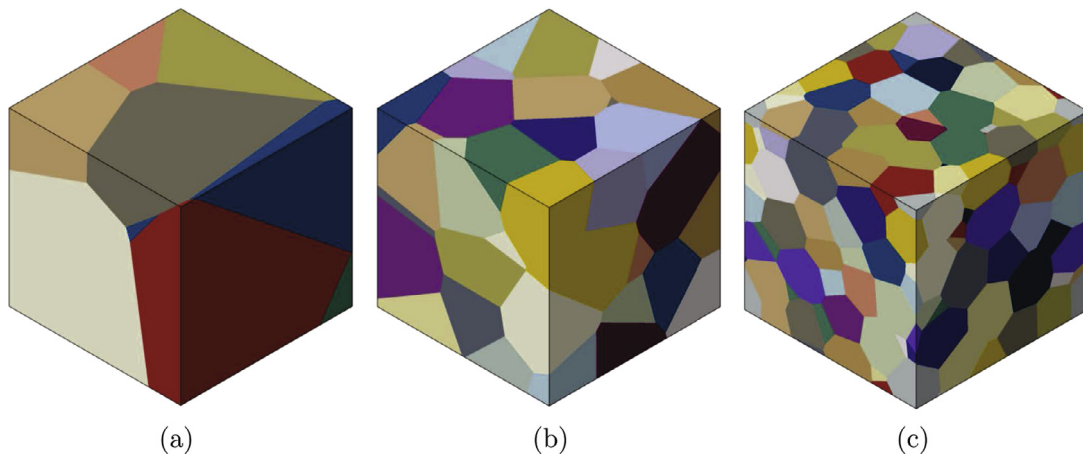


Fig. 11. Voronoi tessellations: (a) Random germ generations with 5 germs. (b) Hardcore germ generations with 50 germs. (c) Periodic centroidal germ generations with 100 germs.

Lamellar microstructures consist of so-called colonies that are of similar shape and are arranged in the same space-filling manner as grains in conventional polycrystals.⁷ In contrast to grains, colonies are divided into thin lamellae as shown in Fig. 12. Depending on the alloy system, the lamellae can be of, e.g., different crystal orientation variants of the same phase or an alternating lay-up of different phases. In addition, material specific features may occur like the waviness of the cementite lamellae in pearlite colonies or the domain structure, subdividing the γ phase lamellae in titanium aluminides, see Fig. 12(b).

Due to the analogies to grain microstructures, RVEs of lamellar microstructures are partly created using techniques described in Section 2.1.1.

2.1.2.1. Microstructure reconstruction from experimental data. While being well established for grain microstructures, 3D reconstructions of lamellar microstructures by serial sectioning (see Section 2.1.1.1) are only reported for pearlite colonies in pearlitic steels [95,223–225] and arrangements of several α laths in Ti6Al4V [226,227] so far. These reconstructions grant

⁷ By lamellar microstructure we do not only refer to microstructures that completely consist of lamellar colonies (fully lamellar) but also address microstructures with a significant volume fraction of lamellar regions/colonies (e.g., duplex or twinning microstructures), since the RVE generation for such microstructures follows the same ideas.

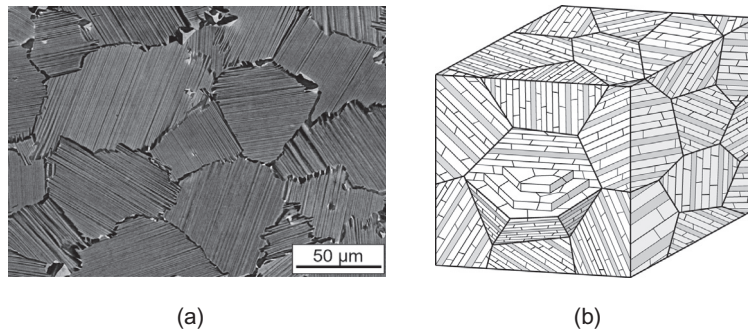


Fig. 12. (a) SEM image of fully lamellar microstructure in Ti-42Al-8.5Nb. (b) Illustration of RVE with lamellar colonies in titanium aluminides. White: γ phase; light gray: α_2 phase. Cut-out shows domain structure in γ lamellae.

valuable insight into the 3D interconnection and waviness of the lamellae, but also reveal the challenges of capturing fine lamellar structures by serial sectioning techniques.

Kral et al. [223] reported problems with aligning successive images during the reconstruction process, since the morphology of the investigated pearlite colonies varied strongly between the sections. Further, many interconnections of branched cementite lamellae were lost in the reconstruction process. This loss of microstructural information results from the thickness of the successively removed material layers. In order to resolve very small microstructural features in the range of, e.g., lamella thickness in TiAl alloys (sometimes <100 nm) or described waviness and branching of cementite lamellae, the slice thickness has to be in the range of a few tens of nanometers (instead of the often reported >100 nm).⁸ Even if feasible with the selected milling technique (e.g., FIB), this results in an even bigger amount of data to be stored and processed and requires a huge number of sections to capture whole colonies that are usually in the range of some ten or even some hundred micrometers.

While these problems are related to the inevitable information loss due to the sectioning process itself, problems may also arise with capturing all information of a single 2D section: Independent of the scanning technique, capturing a representative number of colonies while precisely resolving the lamellar substructure necessitates an extremely high resolution due to the intrinsic difference of corresponding length scales and is, thus, often impeded in a single scan (see e.g. Fig. 1 in [229]). Further, detection problems may occur, e.g., when trying to precisely capture cementite lamellae in EBSD scans [95] which complicates the reconstruction process.

Experiment based reconstruction of lamellar microstructures, thus, remains a challenging task which still has the potential to grant unique insight in their intricate details.

2.1.2.2. Physics based microstructure generation. Due to the complexity of the phase transformations that lead to lamellar microstructures, physics based generation of corresponding RVEs is still not fully resolved and the subject of current research. Yamanaka et al. [230] obtained 2D RVEs of single ferrite-pearlite colonies via phase-field modeling (Section 2.1.1.2). For the subsequent finite element analysis of the different evolving morphologies, the results from the phase-field simulations were converted to 2D computational geometries by digital-image-based modeling.

Recently, 3D large scale phase-field simulations of eutectic solidification of ternary Al-Ag-Cu alloys [231] precisely reproduced the intricate cobblestone microstructure observed in experiments. Since lamellar microstructures often result from eutectic or eutectoid phase transformations, respective phase-field simulations might provide insight into the formation process and can in principal be used for physics based RVE generation in the near future.

2.1.2.3. Geometrical methods. The vast majority of reported RVEs of lamellar microstructures is geometry based and includes some kind of geometric simplification or multi-scale approach. Due to the high aspect ratio of the lamellae (in TiAl often $\frac{\text{colony size}}{\text{lamella thickness}} > 500$), a one to one discretization of a representative set of colonies results in an extreme number of elements and, thus, leads to unreasonable computational costs. Therefore, neither experiment nor physics based RVEs – both of which per definition intend a one to one representation of the microstructure – are widely used in modeling lamellar materials. Basically, two types of RVEs are set up for lamellar microstructures:

- RVEs of a single colony with a representative number of lamellae and
- RVEs with a representative set of differently oriented colonies.

⁸ In fact, 3D reconstructions of fine lamellar structures in block copolymers were reported with 20 nm slice thickness [228].

Depending on the modeling intention, the level of detail of geometry based RVEs may vary. Some authors (e.g., [232–239]) explicitly resolve the lamellae in their RVEs, while others (e.g., [240]) directly aim for homogenized constitutive relations for the single colonies, hence, not considering individual lamellae. Moreover, some authors (e.g., [241–244]) try to reproduce the geometric entities and material specific features of a microstructure as realistic as possible, while others (e.g., [245–248,233,249–251]) consciously choose to create structured RVEs with reduced complexity. Accordingly, the reported geometry based RVEs are categorized as

- lamellar or homogeneous and
- realistic or structured.

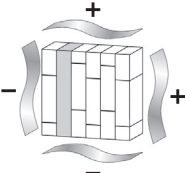
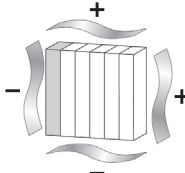
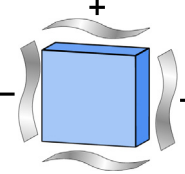
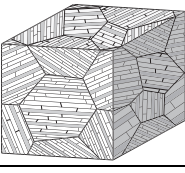
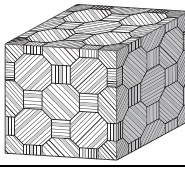
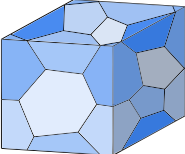
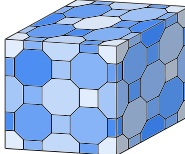
Table 1 schematically illustrates this classification and summarizes the literature in which respective kinds of RVEs are presented.

RVEs of single colonies can act as a starting point for modeling lamellar microstructures, to gain insight into the micromechanics on lamella scale or in the context of multiscale modeling. Their geometries are naturally quite simple and may be generated with standard CAD functions like extrusion of 2D sketches or Boolean operations on primitive 3D bodies. Respective tools are implemented in most commercial FE softwares and usually allow for parametrization and automation of geometry generation via scripting languages. Further, the simplicity of the geometries generally enables structured meshing. Subjected to periodic boundary conditions, these simple geometries still are a suitable representation of the countless lamellae in a single colony.

Polycolony RVEs are generally based on more complex geometries and, thus, need more sophisticated tools to be created. A realistic representation of the grain-shaped colony boundaries (yet without lamellae) can be obtained with the techniques described in Section 2.1.1.3 (e.g., by Voronoi-tessellation). However, most reported polycolony RVEs are created in a structured way using more or less complex, space-filling geometries from simple hexahedra over hexagonal prisms to truncated

Table 1

Strategies for setting up RVEs of lamellar microstructures categorized by level of detail. Homogeneous and lamellar refer to whether or not the lamellae are resolved. Realistic and structured indicate whether it is intended to represent geometrical features of the microstructure as realistic as possible or in a simplified (i.e., structured) way.

		Single lamellar colonies	
		Realistic	Structured
Lamellar		Modeled details domains in TiAl (3D: [232–239])	 Resolved phases TiAl ($\alpha_2 + 6 \gamma$ orientations [238,252,239]; $\alpha_2 + 2$ homogenized γ matrix and twin variants [238,251]); pearlitic steel (ferrite + cementite [253,242,254]; ferrite only [242]); Ti-6242 ($\alpha + \beta$ [255])
Homogeneous	Not applicable		Calibration of homogenized constitutive model TiAl [240]
		Polycolony microstructures	
		Realistic	Structured
Lamellar		Colony geometry Voronoi based [241]	 Colony geometry hexagonal (2D) [233,249,250]
Homogeneous		Colony geometry Voronoi based [242–244]	 Colony geometry truncated rhombic dodecahedral [245]; hexahedral [247,248,238,251]; rhombo hexagonal dodecahedral [256]

rhombic dodecahedra to represent the colonies. Colony shapes can be created using basic CAD functions in commercial FE codes, or, more complex ones, in one of the commonly used geometry exchange formats (e.g., IGES or STEP) from more powerful CAD tools.

If an explicit representation of the lamellae is intended, their number per colony is usually reduced due to discretization problems as mentioned above. Explicitly including the lamellae into the geometry can generally be achieved by Boolean intersection of the single colonies with appropriately oriented planes and subsequent merging of the (now lamellar) colonies. Thus, it is again feasible with built-in CAD functions. Alternatively, a specialized software like NEPER [201] allows direct creation of Voronoi based lamellar RVEs. If the colony geometries were not generated in the FE software, problems may arise due to geometry import: Further geometry processing like creating the lamellae, assigning material properties or meshing may fail as a result of poor geometry or misinterpreted geometric features.

In summary, the intrinsic discrepancy in microstructural lengths (lamella thickness \ll colony size) is impeding the use of realistic RVEs of lamellar microstructures. As a result, mainly homogenized constitutive models and multiscale approaches exist and physics as well as experiment based RVEs are not commonly used yet. Geometry based polycolony RVEs that explicitly resolve the lamellae are so far rarely reported but are expected to become more common.

2.1.3. Other polycrystalline microstructures

In addition to grain and lamellar microstructures, numerous other polycrystalline microstructures exist. Besides the fact that a respective list cannot be comprehensive due to the sheer number of possible alloy systems and their specifics, generation of RVEs for these polycrystalline microstructures is not discussed in detail because:

- Some regularly observed microstructures are not in stable equilibrium (e.g., most dendritic microstructures⁹). They are investigated to understand the underlying formation mechanisms in order to avoid them in technical applications. Thus, geometry generation for constitutive modeling is generally not intended. The microstructure (and, thus, geometry) formation in such systems is mainly modeled in a physics based manner using, e.g., phase-field and cellular automaton methods; see, e.g., [156,258–265] for a non-exhaustive list of formation simulations of dendritic microstructures.
- RVEs of most remaining polycrystalline microstructures are geometrically identical to those of matrix-inclusion composites or porous materials, since the RVE does not incorporate information on the constitutive behavior. Consequently, geometrically, crystalline inclusions/segregations in a crystalline matrix may be considered as closed-cell structures (Section 3.2) or particle reinforced composites (Section 2.3) and microstructures resulting from, e.g., spinodal decomposition may be created like open-cell structures (Section 3.2). For example, the cuboidal microstructure of nickel-based super alloys is atypical for a metal but is geometrically easily described as a matrix-inclusion composite or a closed cell structure.

2.2. Bicontinuous composites

Bicontinuous composites are composed of two solid phases, each of which is continuous in space, and form an interpenetrating network, see Fig. 13. With tailored geometric and topological layouts as well as properties of the phases, synthetic bicontinuous composites are designed to feature outstanding mechanical, thermal and electrochemical properties such as strength, stiffness, toughness, energy absorption, impact resistance, thermal and electrical conductivity, and electrocatalytic performance [266–269,114]. The structures of the bicontinuous composites can be random or ordered.¹⁰ The random structures usually form through a non-equilibrium phase separation process. Examples for random bicontinuous structures are nanoporous titanium-based composites [270], bicontinuous metal-ceramic composites [271] and composites of immiscible polymer blends [272]. Manufacturing ordered structures is possible through various chemical processes at various length scales, for example on the sub-micrometer scale (e.g., block copolymers [273], periodic discontinuous carbon and epoxy composites [274]) as well as in the millimeter range (e.g., bicontinuous polymer/elastomer composites [267] and triply periodically architected polymer composites with interpenetrating phases [275]). Skeletons of sea urchin and butterfly wings are among rare ordered and natural bicontinuous composites with a triply periodic minimal surface-based construction [275].

As seen in Fig. 13, each of the interpenetrating phases reveals an open-cell topology formed of interconnected ligaments. This feature is common to all bicontinuous composites. Thus, the methods for generating their microstructures are in principle identical to those used for generating open-cell microstructures. That is why we also refer the reader to Section 3.2 in which some methods are provided with a broader explanation.

⁹ During solidification of metals, various grain morphologies may emerge depending on the temperature gradient in the melt. If the gradient is negative, the liquid-solid interface becomes unstable and thermal dendrites form. While these have quite characteristic morphologies formed of child arms hierarchically branching off parent arms, at later stages of solidification not only the interdendritic space between arms crystallizes, but also dendritic crystals grow and impinge upon each other. As a consequence, except for the free surfaces of solidification voids, dendritic morphologies usually are not obvious. Thus, although there exists a limited engineering relevance, e.g., increasing ductility through introduction of ductile dendrites of crystalline phases in bulk amorphous alloys [257], in this study we will treat dendritic forms as an intermediate phase configuration during solidification and we will not explicitly investigate methods relevant to generation of such microstructures.

¹⁰ Ordered structures are rare though, especially in nature.

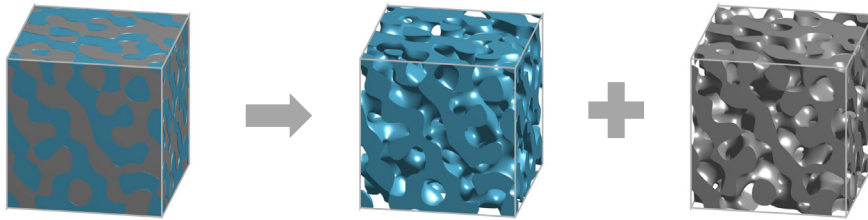


Fig. 13. A typical random bicontinuous composite microstructure composed of an interpenetrating network. Each phase reveals an open-cell morphology formed of interconnected ligaments. Exemplarily depicted is a bicontinuous composite in which each phase has a volume fraction of 50%. Generated based on the algorithm of [276].

2.2.1. Microstructure reconstruction from experimental data

The space filling property of bicontinuous composites proves useful in serial sectioning where the phases stabilize each other under mechanical loading caused by grinding/polishing. Nevertheless, due to the inherently destructive character of the method, serial sectioning only allows static and ex situ observations [277].

Non-destructive X-ray tomography, on the other hand, can be used in investigations of dynamic microstructures and in situ phenomena, e.g., deformation and failure mechanisms under applied loads. One can reach resolutions up to 10 μm and 1 μm in medium- and high-resolution microtomography, respectively [118,278]. The method is especially well suited for metal-polymer bicontinuous composites where the phase contrast is high and if the characteristic sizes are of several micrometers.

For the investigation on the nanoscale, electron tomography in a transmission electron microscope [279,280] or FIB/SEM tomography [98] are used. Although the former method attains high spatial resolution, the latter method is preferable once thicker samples are to be investigated which are not electron transparent. X-ray nanotomography, which constitutes a combination of transmission X-ray microscopy with tomographic methods, allows investigations at the nanoscale with resolutions as low as 30 nm [281,114].

Finally, for polymer/elastomer bicontinuous composites which have a contrast in magnetic moment provided by nuclear spin of the different phases, a non-destructive technique for reconstruction of the 3D microstructures is the magnetic resonance imaging (MRI). Resolutions which can be achieved by this method are in the range of several microns [282].

2.2.2. Physics based microstructure generation

Simulating the kinetics of phase separation constitutes the physics based method for modeling bicontinuous random nanocomposite microstructures. Cahn-Hilliard equations aim at modeling phase separation in binary alloys [283]. Various numerical procedures exist for solving these non-linear partial differential equations, see, e.g., [284–286]. For applications of molecular dynamics (MD) simulations in spinodal decomposition process, bicontinuous structures including atom positions were obtained by a lattice Monte-Carlo simulation of spinodal decomposition, see, e.g., [287]. The drawback of this method stems from the small size of associated spatial and temporal scales if used for MD simulations. A computationally more efficient alternative, allowing investigation at larger scales, is the finite volume method. Originally developed for computational fluid mechanics, nowadays, it is also applied to solid mechanics. A finite volume method-based numerical model of the Cahn-Hilliard equation was implemented in [286] for modeling phase separation in binary polymer systems, see Fig. 14. This work also demonstrates the performance of generated microstructures under applied mechanical loading. Another alternative is, once more, the phase field method. Sun et al. [288] applied this approach and use the Cahn-Hilliard equation as the underlying governing relation. The generated RVE is subsequently used in MD simulations.

2.2.3. Geometrical methods

While studying geometrical methods for generating bicontinuous microstructures, we consider ordered and random microstructures separately.

Ordered microstructures: It is possible to generate ordered bicontinuous composite microstructures by numerically infiltrating the pores in regular (open-)cell idealizations, e.g., those similar to the ones demonstrated in Fig. 44 of Section 3.2.1.3, by a second solid phase. However, as mentioned in Section 3.2.1.3, mostly these idealizations suffer from discontinuous surface normals, which does not meet reality.

To remedy this gap, constructions of (analytical) level surfaces are used. One prominent example for such analytical level surfaces are triply periodic bicontinuous cubic microdomain morphologies which are generated making use of triply periodic continuous minimal surfaces¹¹ represented by functions of the form $F(x, y, z) = \text{const.}$. The level set approximations $F(x, y, z)$ for the triply periodic minimal surfaces as demonstrated in Fig. 15 are

¹¹ In differential geometry, the description of the periodic minimal surfaces was given by Schwarz [289]. Schoen [290] extended this work with newly introduced surfaces as well as a naming convention. A minimal surface is a surface that locally minimizes its area, i.e., the total surface area is minimized subject to some constraint.

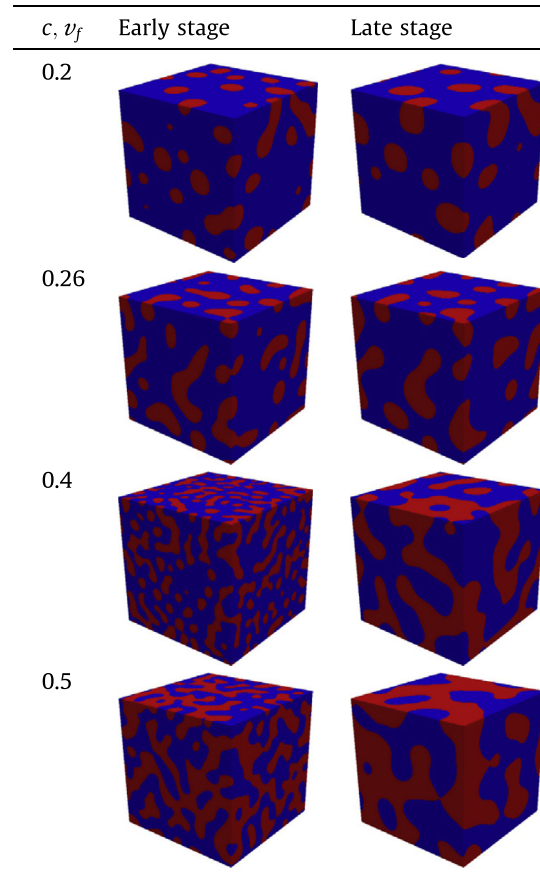


Fig. 14. 3D bicontinuous composite RVEs at early and late stages of phase separation generated by the finite volume method-based solution of the Cahn-Hilliard equations [286]. The coarsening of the ligaments with time is obvious comparing the early and late stages of phase separation. Figure reprinted from [286], under the terms of the Creative Commons Attribution 3.0 licence. <http://creativecommons.org/licenses/by/3.0>.

$$\begin{aligned}
 \text{Schwarz-D (diamond)} : F(x, y, z) &= \sin x[\sin y \sin z + \cos y \cos z] + \cos x[\sin y \cos z + \cos y \sin z], \\
 \text{Schwarz-P (primitive)} : F(x, y, z) &= \cos x + \cos y + \cos z, \\
 \text{I-WP} : F(x, y, z) &= \cos x \cos y + \cos y \cos z + \cos z \cos x, \\
 \text{gyroid} : F(x, y, z) &= \sin y \cos z + \sin z \cos x + \sin x \cos y.
 \end{aligned} \tag{5}$$

These level surfaces and the developed microstructures have the symmetries of a crystallographic group such as cubic, tetragonal, rhombohedral, and orthorhombic symmetries, see Fig. 15 for RVEs of triply periodic minimal surface-based bicontinuous composite microstructures. Triply periodic minimal surface-based composites have recently found a broad interest in the context of ordered bicontinuous composite applications. This is mainly due to the fact that these structures are found to show optimal bulk modulus as well as thermal and electrical conductivity [267]. Also, their analytical and elegant formulation allows systematic investigations for various volume fraction preserving symmetry classes. In the following, we list some noteworthy applications of triply periodic minimal surface-based composites.

Three types of bicontinuous polymer/elastomer composite structures with simple cubic, body-centered-cubic, and face-centered cubic Bravais lattices with triply periodic minimal surfaces of P (primitive), I-WP (wrapped package), and F-RD (rhombic dodecahedra) are investigated considering their elastic stiffness, yield, post-yield, and dissipative behaviors in [267]. Interpenetrating phase composites with triply periodic minimal surface-based sheet and solid reinforcement material are considered in [275], see Fig. 16. Sheet-network reinforcements are shown to feature better mechanical properties than solid-network ones when considering stiffness, strength, and toughness. Interconnectivity of the phases is shown to improve the service performance of the material by avoiding catastrophic failure. Specific energy absorption properties of bicontinuous carbon-epoxy nanocomposites are investigated in [274], see Fig. 17. A noteworthy improvement in the energy absorption of nanocomposites with submicrometer-scale triply periodic architecture is observed. Such a property is crucial considering the field of protective materials, e.g., high-performance protective films, in which dissipation of large mechanical

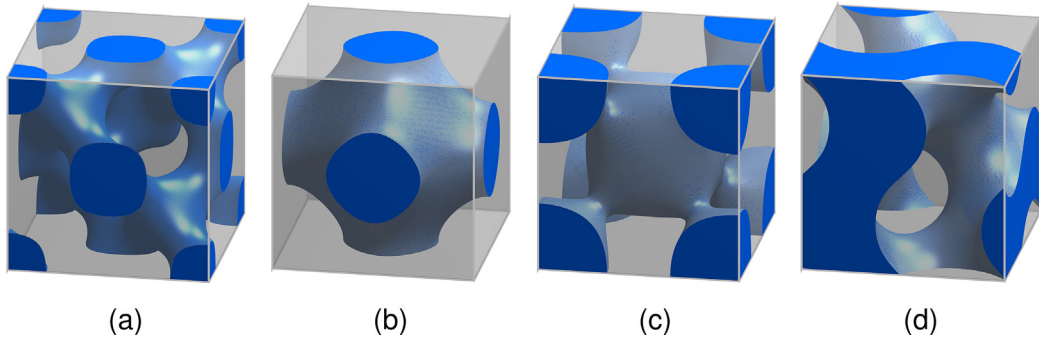


Fig. 15. RVEs of triply periodic minimal surface-based bicontinuous composite microstructures. The interface between phase 1 (blue) and phase 2 (transparent grey) is represented by: (a) Schwarz-D level surface (diamond) of genus¹²3, $F_{\text{Schwarz-D}}(x, y, z) = 1/2$; (b) Schwarz-P level surface (primitive) of genus 3, $F_{\text{Schwarz-P}}(x, y, z) = 1/10$; (c) I-WP level surface of genus 4, $F_{\text{I-WP}}(x, y, z) = -1/10$; (d) G level surface (gyroid) of genus 3, $F_{\text{gyroid}}(x, y, z) = 1/10$. The analytical expressions making up these implicit surfaces are given in Eq. (5), cf. also Fig. 45.

energies with least material mass is aimed at. Without loss of generality, the architecture can be applied to different material combinations, e.g., carbon/light-metal and polymer/piezoelectric materials. Triply periodic minimal surfaces are also applied to biological membranes (see, e.g., the chapter of Zakaria and coworkers in [292]), block copolymers [293–295] and porous materials with open-cell microstructures, see Section 3.2.1.3.

Random microstructures: One robust method to develop random bicontinuous microstructures is to define the interface between two phases making up the bicontinuous composite by a level cut ξ of a Gaussian random field [4,296]. Models depending on random fields require two steps: (i) generation of the random field over the domain, and (ii) performing level cuts (single or double [297]) on the generated field. Leveled-wave models for random morphologies, which were initially proposed for bicontinuous material morphologies formed due to phase separation [298], have found attention in various applications [299,276]. Fig. 13 demonstrates level surfaces developed by Cahn’s method for a gold–polymer nanocomposite. Here, the two-phase microstructure is approximated by the following truncated Fourier series, see Soyarslan et al. [296],

$$f(\mathbf{x}) = \frac{1}{\sqrt{N}} \sum_{i=1}^N c_i \cos\left(\frac{2\pi}{L} \mathbf{k}_i \cdot \mathbf{x} + \varphi_i\right), \quad (6)$$

where \mathbf{x} is the position vector and L is the representative volume element size. N denotes the number of waves considered. The wave phases φ_i and the wave directions \mathbf{k}_i are uniformly distributed on $[0, 2\pi)$ and over the solid angle 4π , respectively. Usually, the wave number is constant, i.e., $k_i = |\mathbf{k}_i| = k_0$. Without loss of generality, the wave amplitude is assumed as $c_i = \sqrt{2}$. Consequently, $f(\mathbf{x})$ gives a Gaussian random function with $\langle f \rangle = 0$, $\langle f^2 \rangle = 1$ where brackets denote ensemble over realizations. Given the random function (6), the different phases of the system are then defined via a selected single level cut ξ :

$$\begin{aligned} \mathbf{x} \in \text{phase 1} & \quad \text{if } f(\mathbf{x}) < \xi, \\ \mathbf{x} \in \text{interface} & \quad \text{if } f(\mathbf{x}) = \xi, \\ \mathbf{x} \in \text{phase 2} & \quad \text{if } f(\mathbf{x}) > \xi. \end{aligned} \quad (7)$$

The Gaussian property of the field $f(\mathbf{x})$ allows the following definition of the single level ξ in terms of ϕ_1 , that is volume fraction of phase 1, with $\phi_2 = 1 - \phi_1$,

$$\xi(\phi_1) = \sqrt{2} \text{inverf}(2\phi_1 - 1), \quad (8)$$

where inverf denotes the inverse error function. Eq. (8) guarantees a priori facilitation of the desired volume fraction in generated microstructures of random bicontinuous composites. 3D bicontinuous composites with RVEs generated making use of the presented leveled wave model are studied in Soyarslan et al. [276], see also Fig. 13.

2.3. Matrix-inclusion composites

Matrix-inclusion composites are characterized by non-overlapping particles embedded in a topologically interconnected matrix. The inclusions are meant to improve the mechanical properties such as specific strength in lightweight construction

¹² Genus of a connected, orientable surface is an integer giving the largest number of nonintersecting simple closed curves that can be drawn on the surface without separating it [291]. It is an important topological invariant which allows quantitative characterization of open-cell materials. 3 is the smallest possible genus for triply periodic minimal surfaces.

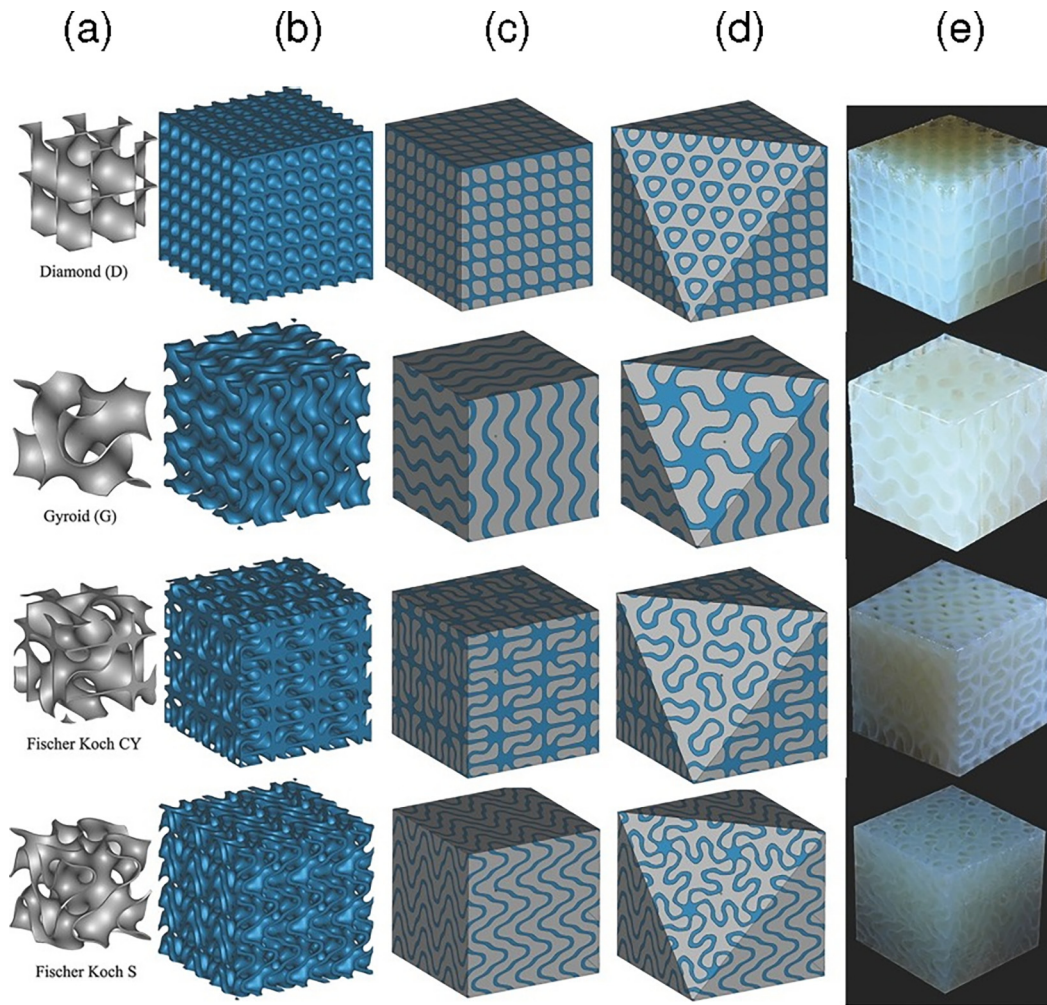


Fig. 16. Triply periodic minimal surface-based topologies with reinforcements of sheet-network and solid-network. (a) Level surfaces considered in model development considering a single unit cell. (b) $3 \times 3 \times 3$ tiling of wetted surface. (c) Interpenetrating composite and (d) its cross-section. (e) 3D fabrication of the developed concept. Figure reprinted from [275], with permission from Wiley-VCH Verlag GmbH & Co. KGaA.

(e.g., short and long fiber reinforced materials), fracture toughness (e.g., polymer blends) or they emanate from the manufacturing process (e.g., injection molding or sintering). In terms of microstructure characterization, volume fraction and geometry of the inclusions are of major importance. Experimental observations indicate various geometries of inclusions, see e.g. Fig. 18, ranging from aspect ratios around unity to several orders of magnitude. In this study, inclusions with aspect ratios <100 are referred to as particles, whereas those with higher aspect ratios are categorized as long fibers. In RVEs, inclusions are often approximated by idealized convex bodies like spheres, polyhedra, capsules or spherocylinders, ellipsoids or cylinders. In addition to the shape, statistical and stereological (interpretation of spatial cuts) information needs to be considered such as, e.g., size distribution, orientation distribution, covariance or pair correlation functions [4].

A prominent example of a material with spherical inclusions are rubber particles in polymer blends. Convex polyhedra are typically employed to mimic inclusions in concrete or asphalt as well as metal matrix composites. Short fiber reinforcements, approximated by cylinders or spherocylinders, are widely used in lightweight constructions (boats, automobiles, water tanks, pipes or external skins) by mixing glass fibers or carbon fibers with polymers. Long fiber reinforced composites, also commonly approximated by cylinders, are common in automotive and aerospace applications, where glass and carbon fiber mats are embedded in polymers. However, for most natural fibers, a simple cylindrical approximation is not possible due to their inherent waviness.

2.3.1. Microstructure reconstruction from experimental data

Composites are made of possibly very different materials, a condition introducing complexity into the choice of experimental techniques. A potentially inherent material contrast allows to employ many characterization methods that are not or only to a certain extent suitable for the investigation of single-phase materials, such as X-ray tomography, energy-dispersive

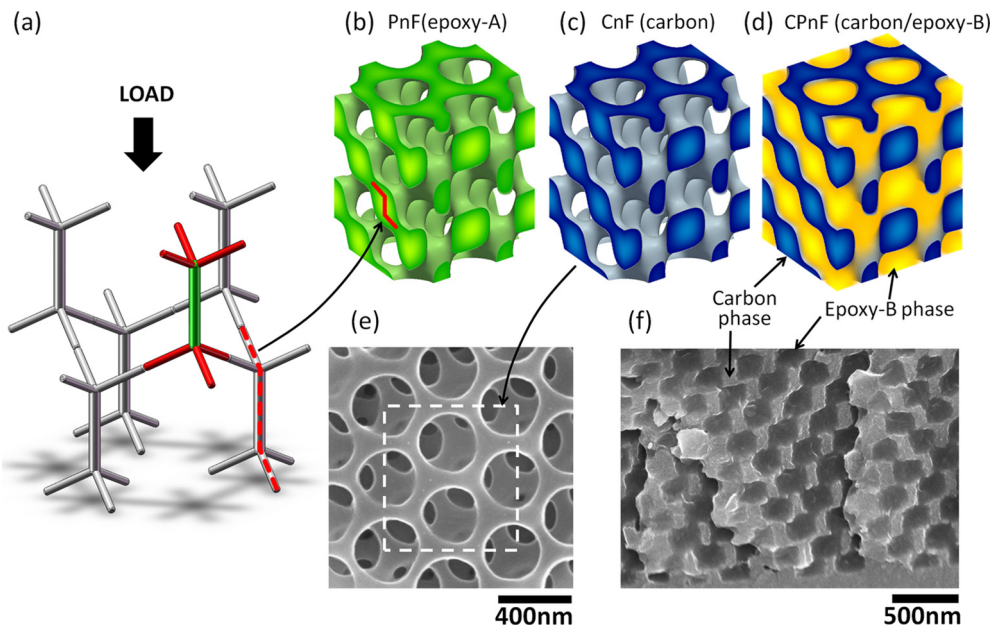


Fig. 17. (a) A load bearing skeleton formed of nanostruts. 1×2 cells of (bc) open-cell and (d) bicontinuous composite microstructures making up the struts. (e-f) Corresponding scanning electron microscope (SEM) images. Figure reprinted from [274], with permission from (Lee, Wang, Boyce, Thomas, Periodic bicontinuous composites for high specific energy absorption, *Nano Letters* 12 (8) (2012) 4392–4396). Copyright (2012) American Chemical Society.

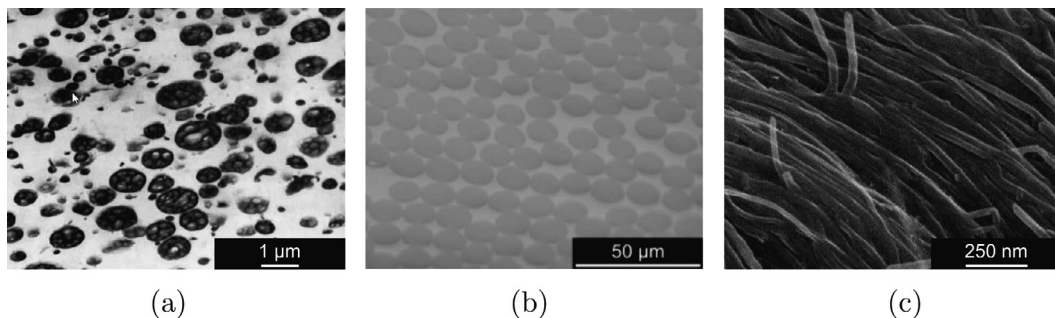


Fig. 18. (a) Polymer blend ABS with ellipsoidal shaped inclusions; (b) fiber-reinforced composite with cylindrical shaped inclusions; (c) wavy carbon nanotubes acting as long fiber reinforcements. Figure (a) reprinted from [300], with permission from Wiley-VCH Verlag GmbH & Co. KGaA.

X-ray spectroscopy (EDS) or atom probe tomography (APT). On the other hand, different behavior of the composite's constituents also introduces difficulties as the chosen cutting and imaging techniques must be applicable to all components.

Imaging methods based on optical microscopy allow for large specimen sizes and are in principle applicable to all material classes. However, depending on the material system, contrast has to be enhanced in pre-processing using staining or etching. In the case of SEM, which is based on imaging with electrons, pre-processing (a thin conductive coating) is required for insulating materials such as most ceramics and polymers. This coating, however, may obstruct both material and topography contrast imaging. Recently, environmental and variable pressure SEM instruments make imaging of insulating materials possible without pre-processing and even hydrated materials can be investigated in such devices [301].

SEM offers a wide range of possible imaging modes, compare also Section 2.1.1.1. In composite materials, especially imaging modes in which contrast results from differences in chemical composition such as back scattered electron (BSE) imaging, Auger electron spectroscopy (AES) and energy-dispersive X-ray spectroscopy (EDS) are of interest. However, in all these methods, it is problematic to differentiate between chemically similar materials or materials with small differences in atomic number z , as present, e.g., in co-polymers. Even voids, i.e., air, and low z materials such as polymers can be indistinguishable.

In cases like these, atomic force microscopy (AFM) [302–304] is a valuable tool. This technique, in which the specimen's surface is scanned with a nanometer sized tip, provides surface images with resolutions of fractions of a nanometer based on the surface topography or differences in the phase of the electric, magnetic, or elastic answer to a respective excitation by the probing tip. In combination with a cutting device, AFM can be utilized to reconstruct microstructures of composites with constituents that provide low contrast in electron imaging such as, e.g., polymer blends as demonstrated in [303].

For 3D reconstruction, imaging methods are combined with different sectioning techniques. To reduce time requirements and minimize possible error sources, setups which combine imaging and cutting and allow automation are preferred, cf. also Section 2.1.1.1. State of the art serial sectioning studies of inclusion composites commonly combine optical microscopy with grinding and polishing [305,78,306], AFM with ultramicrotome cutting [303,307] and SEM with ultramicrotome cutting for softer materials such as polymers or aluminum [308,307] or, for harder materials, FIB/SEM tomography [309–311]. Echlin et al. [312] presented an overview of femtosecond laser ablation combined with SEM imaging. This technique allows exceptionally fast material removal in a few microseconds and, thus, significantly reduces measuring times.

Despite the very different material removal processes utilized in the different sectioning techniques, they all suffer from large differences in the material properties, especially the hardness. If the composite's constituents are very different, e.g., in the case of a polymer matrix reinforced with ceramic particles, material removal is highly irregular [313,307]. If serial sectioning techniques fail, atom probe tomography or methods based on transmissive radiation should be used.

Notably, atom probe tomography (APT) [110,314–316] allows 3D characterization of a material's chemical composition at atomic resolution. The technique is based on the evaporation of atoms from a tip-shaped specimen with a curvature radius below 50 nm. Surface atoms are evaporated in a high voltage field or (for non-conducting specimen) by laser pulsing and accelerated onto a position-sensitive detector. Impact coordinates on the detector and sequence of detection are used to reconstruct the ion's position in the specimen while the atomic species is identified by time-of-flight spectroscopy [316]. However, interpretation of the results is not straightforward as different specimen behave very differently in atom probe tomography and, due to the small sample size, careful statistical evaluation is needed to determine whether recovered atom clusters are random or in fact microstructure features [316,315].

As already described in the Section 2.1.1.1, non-destructive microstructure characterization is handled by tomography with transmissive radiation. The most commonly available method is X-ray tomography (μ CT) [119,120] which allows imaging with a resolution of a few micrometers with desktop instruments. Synchrotron X-ray sources with parallel beams lead to even better resolutions in the nanometer range [317]. However, resolution in tomography scales with the specimen size [117]. Therefore, nanometer resolutions can only be achieved for micrometer samples.

In absorption based X-ray tomography, contrast is a function of the atomic number z , which makes it a natural choice for the non-destructive imaging of matrix inclusion composites, including metal matrix composites [118], ceramic/ceramic composites [318,319], reinforced concrete [320], or fiber reinforced polymers [321–323].

As contrast is based on the atomic number and density of the structure constituents, the problems in distinguishing chemically similar phases arise in μ CT as well.¹³ Furthermore, low z materials generally have low X-ray absorbance. For these materials and phases with similar X-ray attenuation, phase imaging [118,317] is an interesting alternative. This technique is based on measuring the phase difference of a parallel X-ray beam occurring due to light-matter interaction and allows sensitive imaging of edges and boundaries even between very similar phases. These advantages, however, are associated with a more complicated optical setup and require high quality, i.e., coherent, parallel beam X-ray sources.

Alternative to X-ray tomography, other types of radiation can be used. Electron tomography [117,324,325] based on (scanning) transmission electron microscopy, or (S)TEM, is often used for biological materials and polymers because the interactions between electrons and matter are a lot stronger than those between X-rays and matter and, therefore, provide contrast for low z materials while materials with higher atomic numbers are increasingly electron-opaque and, therefore, indifferent. Different imaging modes (discussed above for electron microscopy) can also be utilized in electron tomography as detailed in [325]. Other, less common tomography types which provide different contrast are for example neutron tomography [326] or Terahertz imaging [327].

As discussed in Section 2.1.1.1, many standard imaging methods in tomography are not suitable for crystalline materials because diffraction effects are dominant and reduce contrast. However, techniques exploiting diffraction of X-Rays and electrons [325,121] for imaging of crystalline materials are becoming increasingly common.

Common to all experimental characterization techniques is the need to post-process the data gathered and to identify microstructure constituents from the density and grayscale images. Automatic image segmentation requires special treatment in terms of powerful computational tools and dedicated algorithms for structure identification in different composite types. Often, established 2D techniques cannot easily be translated to 3D [328]. Careful examination of the collected information, however, does not only make the use of reconstructed microstructures as RVEs in FEM studies possible but can also be used for the geometry based generation of RVEs. Liu et al. [329] proposed a reconstruction technique based on Markov Random Field texture analysis that takes a microstructure image as an input to generate structures with a statistically similar structure. Furthermore, many of the geometry based techniques discussed in Section 2.3.3 can be fed with statistical information gathered from experimental microstructure characterization.

The commercial software SIMPLEWARE enables one to process complex 3D image data from experiments to RVEs. Special software solutions are developed in particular for, but not limited to, composites and porous materials. This software has many features for image processing allowing a systematic reconstruction and inspection of internal structures. Therefore, it can be used for visualization of the experimental data, analyzing the data in terms of statistics or to generate meshes for further use in CAD or finite element simulations. Based on scripting languages such as Python, the functionalities of

¹³ While distinguishing chemically similar and, especially, low weight phases with μ CT can be problematic, the technique allows to reliably differentiate pores and low weight materials, making it a popular tool in the experimental characterization of porous materials as discussed in Section 3.2.1.1.

the software can be accessed to automatize the targeted workflow. Examples of the application of SIMPLEWARE to the generation of RVEs can be found for several materials such as a composite cathode for lithium-ion cells [309], asphalt [331], metal matrix composites [330], or open-cell metal foams [332], among others.

2.3.2. Physics based microstructure generation

In most cases, it is inefficient to model the real physical processes of the microstructure generation process for matrix-inclusion microstructures. Bulk or mixing simulations are far too complex and their simulation times are usually not worth the gained findings on particle distributions. However, there are many methods inspired by physical processes like shake-down, motion of particles, growth simulations, or molecular dynamics to name just a few.

Considering particles alone, discrete element simulation of the locomotion of aggregates constitutes physics based modeling of their emerging distribution. The discrete element method is a numerical method using an explicit calculation scheme considering multibody dynamics modeling the motion and interaction of granules during granular flow [333]. Using this method, a physics based microstructure generation is realized through densification under the influence of gravity. One could either first randomly generate particles in a container and, then, apply gravity or let particles of random horizontal direction drop one by one over a set of already equilibrated ones, see Fig. 19. The former method is called mechanical contraction introduced by Williams and Philipse [334], whereas the latter is referred to as drop-and-roll and is due to Visscher and Bolsterli [335].

Here, contacting/bonding conditions between aggregates are crucial together with the size and distribution of each particle. The particle shapes are mostly idealized as 3D polyhedra. During this process, particles continuously interfere with each other by coming in contact or separating. This creates a continuous neighbor exchange with relative granule translations. Mechanical contraction and drop-and-roll algorithms are capable of generating RVEs closer to true packing of inclusions. Due to the packing process, weak anisotropies in vertical stacking direction are present. Furthermore, the packing

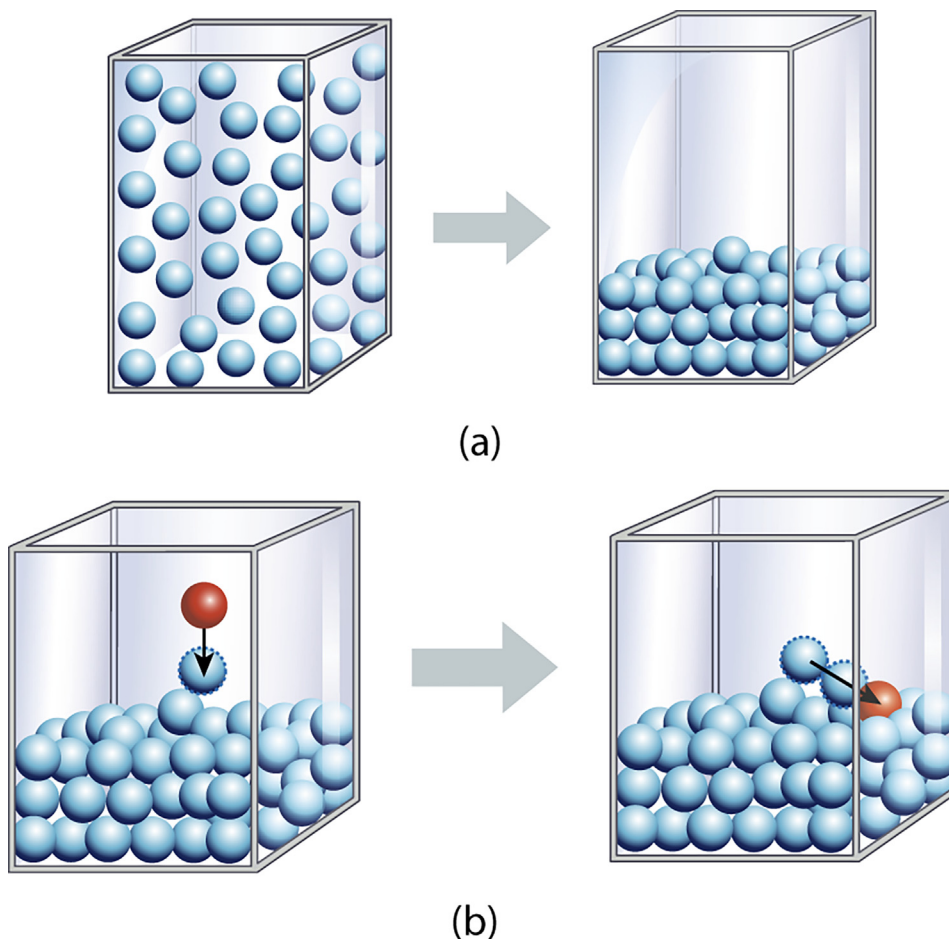


Fig. 19. (a) Mechanical contraction method (also referred to as sedimentation algorithm): generation of particles in a container and subsequent application of gravity. (b) Drop-and-roll method: generation of particles in a container and subsequent dropping of single particles over a set of equilibrated ones. Both use gravity for particle packing. In a variant of the drop-and-roll method, which is called spherical growth method, the granular pack grows spherically with centripetal instead of vertical sedimentation.

might not be very dense (58% for monodisperse spheres) because of a lack of additional compression. Besides spheres, RVEs with ellipsoids are generated by Feng et al. [336] employing an advancing front algorithm. Gaiselmann et al. [337] used a sedimentation algorithm for cylinders to model a short fiber reinforced composite.

In addition to packing algorithms like these, rheological models are of interest in generating microstructures of fiber reinforced composites. By combining mold filling flow simulations with hydrodynamic models of the fiber movement, fiber distributions arising in common processing techniques such as injection molding can be predicted. Models that rely on the discrete modeling of individual fibers and their movement in the matrix flow are, due to considerable simulation times, rarely used. In such particle-based simulations, fibers are represented by chains of spheres [338] or rods [339] and interactions inbetween fibers as well as fibers and the fluid matrix are modeled.

Due to their reduced computational effort, rheological models such as the classical Tucker-Folger model [340] and numerous extensions and adaptations, including ones accounting for slow orientation kinetics [341], fiber breakage [342] and long fibers [343], have gained more attention, see also [344]. These models allow to determine fiber orientation distributions (commonly expressed in terms of fiber orientation tensors [345]) in tandem with flow simulations of the fluid matrix. The determined fiber orientation distributions can subsequently be used in analytical homogenization techniques [346,343] or as input for geometrical generation methods as presented in the following section.

2.3.3. Geometrical methods

2.3.3.1. Composites with particle reinforcement. The artificial generation of particulate microstructures has a long history. One topic often addressed is the shape and representation of the inclusions. The manipulation of these geometric objects with numerical tools for RVE generation requires computational geometry. Moreover, all generation methods need a non-overlapping control algorithm which necessitates a geometric parametrization of the bodies. The center point \mathbf{x}_c is assigned to every shape. Furthermore, for anisotropic bodies, an orientation description via a direction \mathbf{d} with unit length and an angle of rotation $\alpha \in [0; \pi]$ can be introduced. The shapes are then parameterized by:

$$\begin{aligned} \text{sphere :} & \quad \text{sph}(\mathbf{x}_c, r) &= \{ \mathbf{x} | [\mathbf{x} - \mathbf{x}_c]^2 \leq r^2 \} \\ \text{ellipsoid}^{14} : & \quad \text{e}(\mathbf{x}_c, \mathbf{d}, \alpha, a, b, c) &= \{ \mathbf{x} | \mathbf{x} \cdot \mathbf{A} \cdot \mathbf{x} + [2\mathbf{A} \cdot \mathbf{x}_c] \cdot \mathbf{x} \leq c \} \\ \text{cylinder :} & \quad \text{cyl}(\mathbf{x}_c, \mathbf{d}, r, l) &= \{ \mathbf{x} | [\mathbf{x} - \mathbf{x}_c] \cdot [\mathbf{1} - \mathbf{d} \otimes \mathbf{d}] \cdot [\mathbf{x} - \mathbf{x}_c] \leq r^2 \cap [\mathbf{x} - \mathbf{x}_c] \cdot \mathbf{d} \leq \frac{l}{2} \cap -[\mathbf{x} - \mathbf{x}_c] \cdot \mathbf{d} \leq \frac{l}{2} \} \\ \text{capsule :} & \quad \text{caps}(\mathbf{x}_c, \mathbf{d}, r, l) &= \text{cyl}(\mathbf{x}_c, \mathbf{d}, r, l) \cup \text{sph}(\mathbf{x}_c - \frac{l}{2}\mathbf{d}, r) \cup \text{sph}(\mathbf{x}_c + \frac{l}{2}\mathbf{d}, r) \\ \text{polyhedron :} & \quad \text{poly}(\mathbf{n}_i, d_i) &= \{ \mathbf{x} | \bigcap_i^m \mathbf{x} \cdot \mathbf{n}_i \leq d_i \}. \end{aligned}$$

Geometric primitives and the interpretation of the individual parameters are depicted in Fig. 20. Given the parameterization of the geometric bodies, stochastic distributions can be considered with respect to position, orientation and individual parameters in a random manner to mimic experimental findings.

In general, inclusion systems can be generated [347]

- without contact between inclusions (system with isolated particles) or
- with contact between inclusions (packed particle system).

Various methods exist to generate such systems. A major goal is to mimic the statistical information of experimental findings such as location and/or orientation distribution of particles.

Generally, the main challenge is to achieve the volume fraction observed in real materials. This is due to the non-overlapping constraint which is usually executed via pairwise tests of the geometric primitives and, therefore, computationally very time consuming. The non-overlapping constraint is either checked by intersection tests or by distance computations in the framework of computational geometry [348,349]. For spheres, both approaches reduce to calculations of distance between the sphere centers \mathbf{x}_c and are well suited. The highest possible value of the inclusion volume fraction of monodisperse spheres is $\frac{\pi}{3\sqrt{2}} \approx 74\%$. Different authors report an asymptotic value of 64% for the volume fraction of random loose packings of spheres, e.g., [350]. If particles with different sizes are allowed, arbitrarily dense packings are possible.

For capsules, analytical expressions for the non-overlapping constraint exist. This reduces the problem to determining the distance between two line segments [351]. Convex polyhedra are treated by distance calculations between points and planes. For all other shapes, intersection tests and distance computations are by no means trivial. No analytical expressions of intersection or distance computations exist for ellipsoids or cylinders. Therefore, iterative methods have to be taken into account.¹⁵

Random sequential adsorption method: The random sequential adsorption method is the most intuitive and most widely used algorithm to generate non-overlapping matrix-inclusion RVEs. It was introduced in the fundamental work of Widom [355]. Objects are added randomly and sequentially and the method can be divided into four steps:

¹⁴ with $\mathbf{A} = \mathbf{Q}^T \cdot \text{diag}(1/a^2, 1/b^2, 1/c^2) \cdot \mathbf{Q}$, $c = \mathbf{x}_c \cdot \mathbf{A} \cdot \mathbf{x}_c - 1$ and the rotation matrix (here given by Rodrigues' rotation formula) $\mathbf{Q} = \mathbf{d} \otimes \mathbf{d} + \cos(\alpha) [\mathbf{1} - \mathbf{d} \otimes \mathbf{d}] - \sin(\alpha) \mathbf{e} \cdot \mathbf{d}$.

¹⁵ Eberly [351,352] suggested fast intersection tests of ellipsoids and cylinders. Viable approaches for distance computations are also introduced by Lin et al. [353] for ellipsoids and [354] for cylinders.

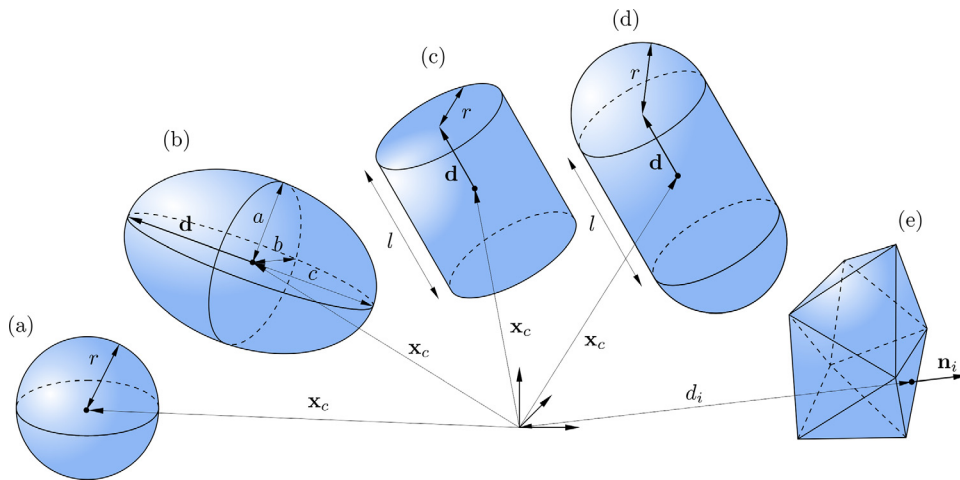


Fig. 20. Geometric primitives: (a) sphere, (b) ellipsoid, (c) cylinder, (d) capsule, (e) polyhedron. Spheres are isotropic and do not have an orientation, thus are described via the center point \mathbf{x}_c and the radius r . For ellipsoids, capsules and cylinders, the orientation \mathbf{d} needs to be considered. In addition, for ellipsoids, the three half-axes are described by a , b , and c , for capsules and cylinders the radius r and length l need to be stated. Convex polyhedra are defined by the intersection of half spaces.

Algorithm 1: Random sequential adsorption process.

```

1 while stop criterion not met(e.g., inclusion volume fraction) do
2   randomly place inclusion  $i$ 
3   if non-overlapping check==FALSE then
4     reject inclusion  $i$ 
5   end
6 end

```

One disadvantage of the random sequential adsorption approach is the low volume fraction achievable. In order to ensure the non-overlapping requirement for inclusions, the distances between the to-be-placed inclusion and all existing ones are calculated. If the distance is smaller than an a priori defined minimal distance d_{\min} , the new inclusion is rejected. The number of rejections increases drastically with increasing volume fraction or aspect ratio of the geometric primitives. Consequently, generating high volume fraction RVEs is very time consuming if not impossible.¹⁶ In the placement procedure, arbitrary distributions enter the process. Thus, statistically distributed orientations easily arise. Various researchers employed the algorithm for generating RVEs with spheres [358,356], capsules [358], cylinders [359,360,12], ellipsoids [358,361] or approximations of those shapes via lines or convex polyhedra [12,362].

Collective rearrangement algorithms: Collective rearrangement algorithms are typically utilized in combination with random sequential adsorption or sedimentation methods which generate an initial configuration with possibly overlapping particles. In a second step, a denser packing is achieved by repositioning and shrinking some or all particles. The densification processes are inspired by molecular dynamics, compression tests or artificial repositioning schemes driven by heuristics.

Repositioning by an artificial scheme is used by Jodrey et al. [363] for spheres of equal radii. Starting from an initial configuration with overlapping spheres, the particles are shrunk and intelligently removed to reach a volume fraction of 64.2–64.9%. An innovative method of generating cylinders and spheres based on a constrained optimization formulation is given in [364]. In the case of unidirectional cylinders of equal diameter, volume fractions of 80% are achieved; for spheres only up to 40%. Schneider et al. [136] combined a random sequential adsorption process with migration and repositioning of fibers. Fed by a given orientation distribution, large fibers are iteratively moved, driven by the solution of a minimization problem. Large aspect ratios as well as high volume fractions up to 60% are achieved.

Balzani et al. [365] generated so-called statistically similar RVEs which are less complex than a fully representative choice, but exhibit similar statistical features as the real microstructure. They proposed a least-square functional including an arbitrary number of statistical measures. By minimization of this functional, the artificially generated RVE is statistically similar to the included statistical information. They utilize ellipsoids which are repositioned during the optimization procedure and which may overlap.

¹⁶ In 2D, a circle jamming limit of 54.7% [356] and, in 3D, an asymptotic limit volume fraction of 38.5% for monodisperse spheres [357] are reported (as compared to the theoretical maximum of 74% for the close packing). Therefore, RVEs generated employing the random sequential adsorption method typically feature volume fractions up to 20%.

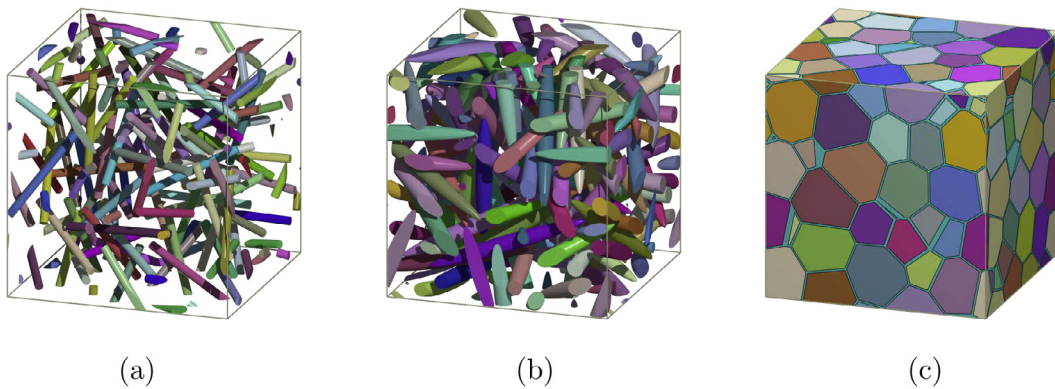


Fig. 21. Geometric setting of various matrix-inclusion composites: (a) 100 cylindrical inclusions with an aspect ratio of 25 and a volume fraction of 5%. (b) 100 ellipsoidal inclusions with an aspect ratio of 10 and a volume fraction of 20%. (c) 100 polyhedral inclusions with a volume fraction of 90%.

Inspired by molecular dynamics, Alder et al. [366] introduced the idea to solve Newton's law of motion for every particle: particles move towards each other due to artificially introduced attracting forces. Contact algorithms or approximate contact algorithms (intersection tests) need to be employed to circumvent overlapping. Recent works in this field are presented by Ghossein et al. [367]¹⁷ and Salnikov et al. [368].¹⁸

Another method is inspired by compression and shaking. By employing external constraints, introducing gravitational forces and accounting for contact between the particles, the initial configurations are densified. Han et al. [369] achieved an inclusion volume fraction of 52% for monodisperse spheres by a combination of global compression, random (local) compression as well as shaking. Yu et al. [370] suggested a compacting algorithm also applicable to ellipsoids of moderate aspect ratios. More recent contributions address cylinder based fiber reinforced RVEs. Starting with experimental data of a fibrous microstructure as input, Gaiselmann et al. [371] compressed a fibrous network of cylinders. In contrast, Harper [372] et al. and Islam et al. [373] used FE-simulations to compress and obtain inclusion volume fractions of up to 50%. Sheng et al. [374] and Wang et al. [375] modeled concrete-like particle reinforced composites with polyhedral inclusions. The RVEs are generated by free fall acceleration simulations incorporating gravity and contact in terms of FE-simulations.

Catalanotti et al. [376] introduced an algorithm for spheres that is capable of generating RVEs with volume fractions up to 74%, see also Moscinski and Bargiel [377,378] or Maggi et al. [379] for volume fractions up to 70%. Catalanotti's method combines multiple packing arrangements starting from the densest packing (fcc) configuration and randomly removes and repositions the particles until the desired volume fraction is reached.

Popular methods in generating granular media composites employ geometric adaption of particles in terms of pure shrinking [380–383]. In contrast to the aforementioned geometric shapes, these microstructures are based on polyhedral inclusion shapes. Starting from an initial Voronoi tessellation, iterative shrinking is employed, allowing for arbitrary volume fractions. By appropriately choosing the initial Voronoi tessellation, grain size distributions can be incorporated in the final microstructure. Fig. 21 depicts some typical microstructures.

DIGIMAT is a commercial modeling platform for non-linear multiscale material and structural modeling problems. The finite element toolbox offers the possibility to create realistic RVEs for different inclusion shapes and material properties. Examples include the generation of RVEs with randomly distributed spherical inclusions [384,385], perfectly aligned fibers [386] or random fiber distributions by using a fiber randomization algorithm [387]. These RVEs can be exported as common CAD formats. DIGIMAT also includes a mean field homogenization toolbox to predict effective non-linear material parameters for all kinds of inclusions and sizes in an efficient way. Furthermore, the software includes tools for exchange of experimental data and material models, direct coupling to finite element software such as LS-DYNA, mapping results between different meshes as well as special purpose tools, e.g., the computation of composite sandwich panels.

Regular packing of microstructures

Some structures consist of regular or almost regular microstructural arrangements. In some of these cases, the simplest possible unit cell might be sufficient, but this is not necessarily the case. If one is interested in plastic or damage behavior, for example, larger volume elements are needed in order to ensure representativeness. Further, it may not be efficient to create random microstructures for complex inclusion shapes and/or high volume fractions. Depending on the underlying problem at hand, it might be sufficient to approximate the microstructure by regular patterns of the geometric entities.

¹⁷ Volume fraction of ellipsoids up to 40%.

¹⁸ Volume fraction of spheres and cylinders up to 40%.

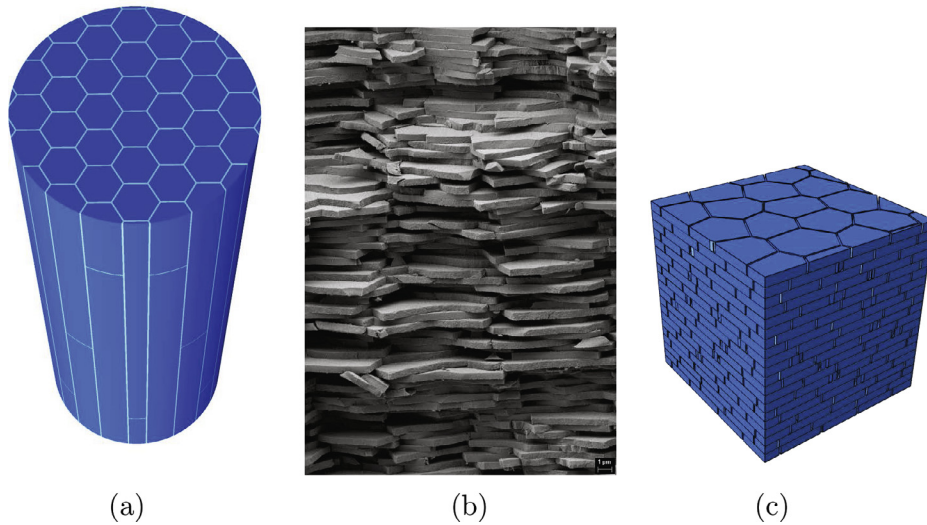


Fig. 22. Regular arranged 3D matrix-inclusion RVEs: (a) Dental enamel which consists of a microstructure with mineral fibers in protein matrix. (b) SEM image of nacre, a natural brick-and-mortar-structure and (c) a corresponding RVE.

The challenge does not lie in creating one RVE, but to automatize the generation in order to create many variations of the microstructure to account for statistical representativeness as well as to investigate structural influences for structure-property relations.

Non-simple, regular arranged 3D RVEs were created, for instance, for biomaterials, see Fig. 22: dental enamel (fiber reinforced microstructure) can be approximated by regular positioned prismatic fibers [388]; nacre (brick-and-mortar structure) as polygonal tablets which are non-flat but slightly wavy as characterized by a laser profilometer [389]. The brick-and-mortar RVE representing nacre (Fig. 22(c)) is created by shrinking multiple 2D Voronoi tessellation (cf. Section 2.1.1.3) which are subsequently extended into 3D and arranged arbitrarily on top of each other.

2.3.3.2. Composites with long fiber reinforcement. An increase in aspect ratio of reinforcing particles or fibers generally results in an increased stiffness and strength of the composite. However, composites reinforced with high aspect ratio or long fibers¹⁹ are more difficult to produce on a large scale than short fiber composites, a condition which impedes their use in every-day applications.

Automotive and aerospace applications, however, benefit especially from the enhanced impact and fatigue resistance associated with the high aspect ratio of continuous fiber reinforcements. In the last decades, carbon fiber-reinforced polymers have steadily replaced metals in aircraft construction. While in the 1980s, less than 10 weight-% of an aircraft were made from carbon fiber-reinforced polymers, today, carbon fiber-reinforced polymers account for 50% of the weight of the Boeing 787 and 53% in the A350 XWB [390]. This replacement of traditional materials with carbon fiber reinforced laminates results in emissions that are approximately a quarter lower than those of comparable aluminum aircrafts [390].

Long and continuous fibers are generally utilized in one of three forms, as depicted in Fig. 23, that is either as single fibers or in bundles of parallel fibers which we refer to as tows.²⁰ The third form, a twisted bundle (or tow), is called a yarn. All three configurations are commonly simplified and modeled as a single fiber, if the microstructure level of interest is significantly larger than an individual fiber diameter.

In a first approximation, fibers in long fiber composites are considered to be straight and unidirectionally oriented. If furthermore a regular fiber packing in the transverse cross-section is assumed, simple periodic elements as depicted in Fig. 24 can be employed as RVEs.

Both assumptions are in general far from reality and very limiting. In most unidirectionally oriented composites, the fibers are distributed randomly in the transverse cross-section [391]. These and other deviations from the idealized structure such as intertwining, varying diameters and waviness of the fibers directly influence their reinforcing capabilities. This is seen, for example, in composites reinforced with carbon nanotubes [392], which exhibit all the aforementioned deviations. Depending on the material under consideration, modeling approaches focus on two categories of fibers: straight and wavy.

Straight fibers: Typical examples for composites with reinforced straight fibers are glass or carbon fiber reinforced thermosets. In these composites, unidirectional mats of fibers are shaped as desired and are then impregnated with resin, layered

¹⁹ Here and in the following, “long fiber” is used to denote inclusions with aspect ratios of ≥ 100 , which includes both discontinuous fibers with high aspect ratios and continuous fibers as the general principles of RVE generation as presented here can often be employed for both groups.

²⁰ This is in accordance with the definition employed for carbon fiber reinforcements. In textile industries, “tow” refers to coarse, shorter natural fibers.

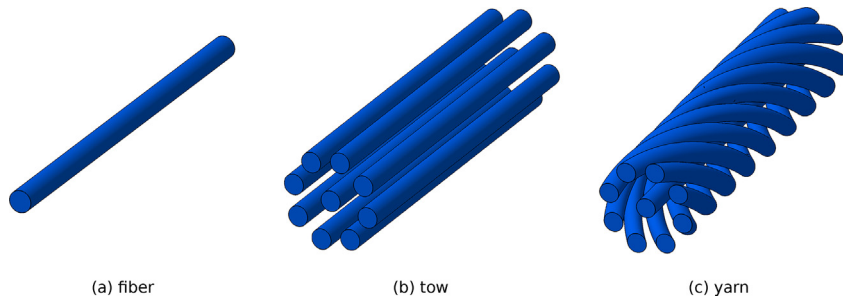


Fig. 23. Different forms in which fiber reinforcements exist: (a) single fiber, (b) tow as a bundle of parallel aligned single fibers and (c) yarn as a twisted bundle of aligned fibers.

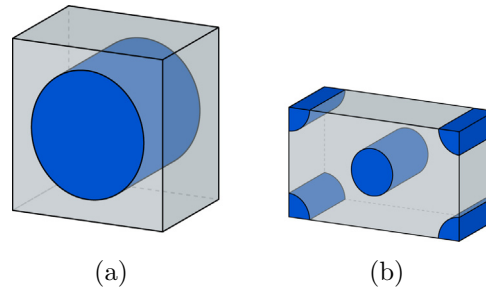


Fig. 24. Examples of periodical RVEs of idealized unidirectionally oriented long fiber composites: (a) square and (b) hexagonal fiber packing.

and cured into composite lamina. Furthermore, carbon fibers, among others, can be woven into bi-directional mats (cf. Section 3.1.1 on the generation of RVEs for woven structures).

Periodic fiber distribution: To describe microstructure dependent properties in a unidirectional composite, the simplest approximation is a regular, periodic packing of fibers. The first unifying discussion of unit cell-RVEs for such periodic arrangements was presented in [393], focusing on hexagonal packing,²¹ see Fig. 24(b).

Such an idealized structure results in small and simple RVEs and, therefore, fast computations especially if symmetries are also exploited in the assignment of boundary conditions [394]. Despite their highly simplified structure, these periodic unit cells are employed, e.g., as statistically equivalent replacements for complex realistic microstructures [395] or in cases in which the precise fiber distribution only plays a secondary role such as in the investigation of interlaminar effects [394].

Partially random fiber distribution: While idealized fiber packings can be assumed if effective properties along the fiber direction or interlaminar effects are studied, they are incapable of capturing behavior associated with fiber interaction in the transversal direction. It was shown that this spatial distribution of the fibers significantly influences the transverse mechanical properties [396], damage initiation and failure [14] and electric conductivity [397].

In the case of straight fibers, the fibers are in general still considered to be parallel. Thus, the microstructure generation reduces to the generation of a random distribution of disks that is subsequently extruded into the third dimension. In general, a square sample area is chosen to be populated with these disks. The edge length of this square should be at least 50 times the fiber radius to correctly reproduce the randomness of fiber reinforced materials [14]. To populate such a 2D square with disks, generally three approaches exist:

1. digitization of cross-sectional images
2. randomization of a regular, periodic arrangement or
3. random placement based on, e.g., the random sequential adsorption algorithm (see also Algorithm 1 in Section 2.3.3.1).

The first approach is based on experiments and is, therefore, very time-consuming if more than one sample needs to be considered. In the other two approaches, which are geometry based, the algorithms can be fed with statistical data (diameter distributions, mean distances, etc.) gathered from analysis of 2D microstructure images of transversal cross sections.

Geometry based approaches utilize the same general techniques as introduced in Section 2.3.3.1 for 3D particle distributions. In early studies, especially collective rearrangement algorithms, cf. Section 2.3.3.1, were employed. An initially square configuration of fibers with varying diameters can be randomized using Monte Carlo simulations: the coordinates of random fibers are altered while simultaneously the container size is reduced to increase the volume fraction [396]. Comparison with experiments shows excellent agreement of the predicted elastic constants in the transverse direction. Alternatively, it is

²¹ Hexagonal packing preserves transversal isotropy as opposed to square packing.

possible to start with a hexagonal packing (and a non-varying fiber diameter) and randomly relocate every disk in numerous iterations by selecting a random rotation angle and shifting the disk towards the next disk in that direction [391].

One method to achieve extremely high volume fractions of over 90%, however, only with partially random fiber packing, divides a square sample area into a grid of variable size (in the order of the fiber diameter) [398]. In each cell, a fiber is placed randomly, resulting in a globally approximately homogeneous fiber packing. To eliminate the generated overlaps, the packing is then allowed to relax. Unfortunately, the fibers tend to accumulate in very dense hexagonally packed areas that are separated by channels of pores and are partially randomly distributed. The algorithm duplicates fibers that are cut by the bounding box, resulting in a geometrically periodic RVE, which is not the case in the previously discussed algorithms.

Approaches based on random sequential adsorption (see Section 2.3.3.1) have to overcome the jamming limit (i.e., volume fractions greater than $\sim 55\%$) for fiber reinforced composites. This can be overcome by initially placing fibers using random sequential adsorption and then heuristically stirring the fibers in two steps [399]. The first step incrementally moves all fibers towards their closest neighbors, generating matrix-rich areas which facilitate further fiber placement with random sequential adsorption. The second step is localized to an area close to the RVE's edges and prevents clustering of fibers close to the edges and, therefore, local density variations. Fibers cut by the bounding box are duplicated, i.e., the resulting RVE is periodic. RVEs of transversely random fiber composites are generated with a fiber content of more than 65% volume fraction. Different fiber diameters can be accounted for [400]. Comparison of the RVEs with micrographs of 3D woven non-crimp carbon fiber/epoxy composites shows that they are statistically equivalent [401].

An alternative modification of random sequential adsorption is called the random sequential expansion algorithm [402]. Here, the first fiber is placed randomly. Neighboring fibers are generated iteratively via a random rotational angle and distance until no more fibers can be created without causing an overlap, resulting in a small cluster of fibers around the original fiber. Then, the algorithm moves on to the second fiber, filling the area around it. With this algorithm, fiber concentrations of $\sim 68\%$ volume fraction are achievable.

The general step sequence of the random sequential expansion algorithm is similar to the nearest neighbor algorithm proposed in [403] which, however, is a combined experimental-numerical approach. Here, first and second neighbor distributions are analyzed in micrographs of carbon fiber reinforced polymers and used to feed the algorithm. This generates fibers as first and second neighbors around a starting fiber, thus, reproducing both the short and long range interactions of the real composites in the generated microstructures. Including both, first and second neighbors, prevents fiber aggregation in the center area which might arise using the random sequential expansion algorithm. Introducing probability equations into the nearest neighbor algorithm improves the statistical equivalence of the generated microstructure with experimentally determined distributions [404].

Random fiber distribution: Long fiber composites with a random fiber distribution are less common because the very high aspect ratios require dedicated production techniques that are debilitatingly expensive compared to the mass production techniques of short fiber reinforced composites. Moreover, computational generation of such structures with realistic volume fractions is still an open challenge. One approach is to model fibers or tows as straight 1D elements and to allow intersections of fibers. While physically impossible, this approach allows to achieve random microstructures with fiber aspect ratios up to ~ 230 [405] from a random placement technique. As intersections of fibers are allowed, these structures can only be used to observe general trends or provide comparisons and not as an accurate depiction of realistic materials. Dirrenberger et al. [12] generated RVEs without intersections and large aspect ratios up to 100, achieving a volume fraction of 16%.

Realistic, non-overlapping structures can be generated with methods based on random sequential adsorption [361]. However, due to the increased number of rejections arising due to the high aspect ratio of the fibers, it is hardly feasible to generate structures with volume fractions of more than 10%, as depicted in Fig. 25.

In order to carry out computations on RVEs with a realistic microstructure, recently 3D reconstructions of the real composites from tomography data are becoming promising, compare Section 2.3.1.

Wavy fibers: While many applications rely on straight fiber reinforcements, most fibers are in fact wavy. This waviness may have been induced during composite production by, e.g., the resin flow, or is an inherent property of the fiber material.

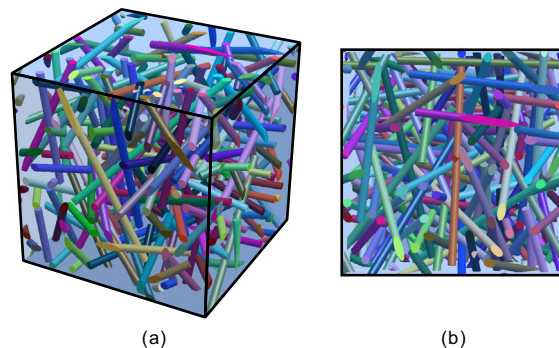


Fig. 25. Fully random distribution of non-overlapping fibers generated based on the approach of Schneider, Klusemann and Bargmann [361] using a random sequential adsorption algorithm. 10% volume fraction. (a) 3D view. (b) Top view.

Especially natural organic fibers and nanosize reinforcements such as carbon nanotubes exhibit pronounced waviness. This waviness partly determines the composite's mechanical properties.

Natural fibers with an inherent waviness such as flax, hemp, or sisal gain importance as reinforcement in polymer-matrix materials, especially in automotive industry. This is in large parts due to sustainability goals: Natural fibers are light, biodegradable, based on renewable raw materials and the energy consumption during production is small as compared to glass or carbon fibers [406]. Furthermore, natural fibers exhibit higher acoustic damping than conventional materials [407], which is exploited to address noise reduction in automobiles.

Carbon nanotubes, on the other hand, exhibit a number of outstanding properties, such as an elastic modulus comparable to that of diamond, and exceptional thermal and electric conductivity. While the latter properties allow for application in functional composites (compare, e.g. [397]), the reinforcing capabilities of carbon nanotubes generally fall short of theoretical predictions. The nanotube waviness is frequently identified as one of the core reasons for this shortcoming [408,409].

Regular waviness: Early attempts to describe the waviness of fibers are based on regular geometries. The waviness of carbon nanotubes can be modeled with a sinusoidal function, in which the waviness is characterized by the amplitude r and the wave length λ [408], compare Fig. 26(a). Using the equivalent fiber approach, a single sinusoidal fiber with surrounding matrix is modeled to determine effective mechanical properties [408], see also [410].

An RVE for laminate composites that describes fiber waviness also using a sinusoidal function was presented in [411]. In this approach, a 2D unit cell of a periodic hexagonal fiber distribution is extruded in the third dimension along a sinusoidal trajectory, resulting in a fully periodic RVE of parallel, wavy fibers.

Assuming sinusoidal waviness, however, only accounts for in-plane waviness. To model 3D waviness, [412,413] based their models on a helical fiber geometry as depicted in Fig. 26(b).

While such idealized descriptions of fiber waviness provide insight into the effects of deviation from a perfectly straight fiber geometry, realistic fiber waviness is random and often highly irregular.

Random waviness: Random nature of fiber waviness may result in agglomeration or intertwining of fibers in certain regions. These effects are major contributors to the reinforcing capabilities of wavy fibers. Wavy long fiber reinforcements are generally of two types:

- fibers with regular orientations, i.e., they are oriented so that their longitudinal axes around which they meander are aligned.
- fibers with random orientation with no preferential fiber orientation.

Due to the random nature of the waviness, entanglement and intertwining are possible in both types.

Arrays of oriented, stochastically wavy carbon nanotubes were modeled using a random walk method in [414]. The underlying statistical distributions of the tortuosity are determined from experimental 2D micrographs. In this method, the transversal growth of a single carbon nanotube fiber is confined by a bounding box, thus, preventing entanglement and limiting the tortuosity of the fibers.

Recchia et al. [415] also used a random walk algorithm to generate randomly wavy, entangled fibers forming a twisted yarn, see Fig. 27. To achieve an entanglement of fibers without intersections, fibers are generated stepwise on hexagonal grid planes that lie perpendicularly to the yarn direction. On the first of these planes, a fiber is initialized randomly with a point in one of the hexagonal cells. In the next step, the fiber is continued by passing through either the same hexagon on the next plane or one of the six cells in direct contact with it, resulting in a continuous but random path over multiple planes. Cells which are already filled with a fiber are inadmissible and, furthermore, crossing of paths with another fiber is prevented. If

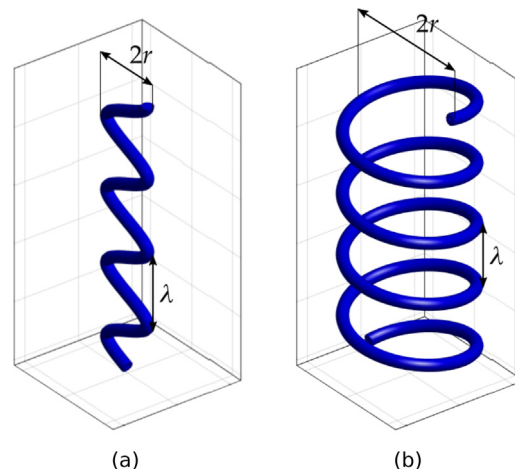


Fig. 26. Fiber waviness with regular geometric structures: (a) sinusoidal and (b) helical waviness.

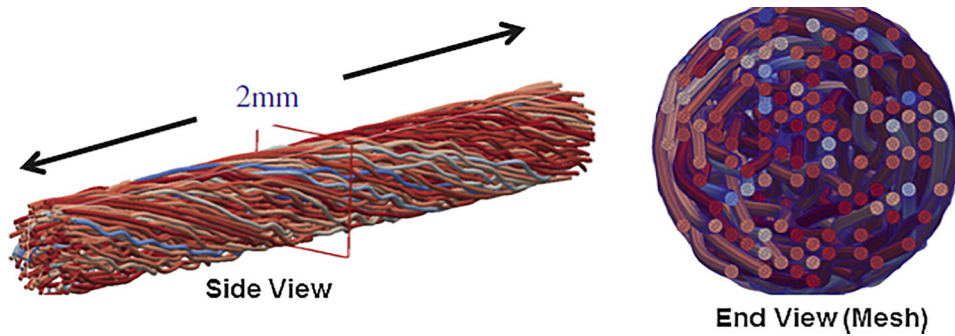


Fig. 27. RVE of a yarn consisting of randomly wavy fibers. Figure reprinted from *Acta Mechanica*, Fiberwalk: a random walk approach to fiber representative volume element creation [415], 225, 2014, 1301–1312, Recchia et al. (original copyright notice as given in the publication in which the material was originally published) With permission of Springer.

one fiber cannot move onto the next plane because no viable paths remain, it is terminated and a new one is started in an open space. Furthermore, the algorithm provides an option to introduce inclusions which the fibers cannot penetrate. The microstructures generated with this algorithm are not intended as representations of a composite material but it is possible to extend the algorithm accordingly.

The choice of a random walk through adjacent grid cells for high volume fractions of fibers limits the tortuosity to comparatively small values. Herasati et al. [416] proposed a model for entangled and interweaving carbon nanotubes that does not inherently restrict the tortuosity. Furthermore, it uses parameters identified from micrographs to describe the waviness of the nanotubes. In this approach, each fiber is composed of a sequence of straight line segments. Starting from an initial point on one RVE face, each segment is constructed on the basis of a random angle towards the previous segment's direction and a random rotation around this direction. A new segment is only generated if it does not intersect another fiber.

Drücker, Wilmers and Bargmann [417] based their work on this algorithm, using the end points of the line segments as geometry defining points which are connected with interpolating cubic splines. This guarantees a continuous geometry and prevents the occurrence of artificial kinks and sharp edges. Furthermore, in Drücker, Wilmers and Bargmann [417], the algorithm of Herasati and Zhang [416] is modified such that the generated RVEs are geometrically periodic. Using this approach, RVEs with volume fractions of up to 16% and realistically large waviness and entanglement can be generated, see Fig. 28, as it does not impose any restrictions on the fiber path within the RVE volume.

Motivated from studying randomly distributed cellulose fibers, Faessel et al. [418] modeled a 3D network of tortuous fibers by first generating a straight line that is randomly oriented within a cubic cell. The length of this line is determined from statistical distributions informed from X-ray tomography data. Around the line, curvature points are placed randomly. Using cubic interpolating splines, these points are connected and finally, a tube with a specified radius is extruded along the spline. In this algorithm, fibers are generated independently without intersection checks. Overlaps of fibers are considered to be rare due to low volume fractions and are treated by removal of the intersecting volume and subsequent definition of a contact interface. While generated fibrous network structures are subsequently not embedded in a matrix, such an extension seems possible if not entirely desirable due to the treatment of fiber overlap.

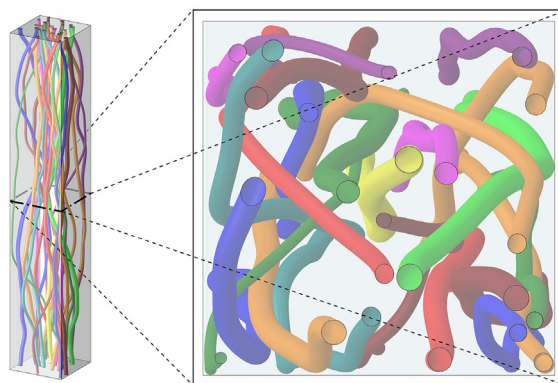


Fig. 28. Periodic RVE of a composite with carbon nanotube arrays, illustrating the random waviness and entanglement of the nanotubes. RVE generated based on Drücker, Wilmers and Bargmann [417].

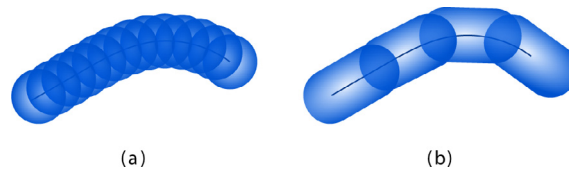


Fig. 29. Representation of part of a wavy fiber as a chain of (a) balls or (b) spherocylinders along a spline as used in [419] or [420]. Using spherocylinders instead of balls results in a less accurate geometry representation but significantly reduces the computational effort.

A random structure of non-overlapping randomly wavy fibers can also be generated by representing fibers by chains of intersecting balls [419], see Fig. 29(a). Using random walks, these balls are consecutively generated with a random orientation according to a multivariate von Mises–Fisher distribution and a possibly varying radius. The distance between the center points of the balls is chosen in a trade-off between accuracy of the structure representation and a treatable number of points. If spherocylinders (Fig. 29(b)) instead of balls are used, the computational effort is significantly reduced [420]. This initial structure still allows overlap of different fibers or different parts of the same fiber. To correct this, fibers are redistributed in a second step using force-biased fiber packing. Here, repulsion forces are used to prevent overlapping while a recovery force aims to keep the angles and distances between adjacent balls to prevent folding and unrealistic kinks in the fiber geometry. The algorithm uses stochastic distributions to capture the fiber orientation and, thus, allows generation of randomly distributed as well as oriented fibers with the same algorithm. Furthermore, exceptionally high fiber volume fractions of around 50% can be achieved with this algorithm, however, this also results in a low degree of tortuosity of the fibers.

3. Porous solids

We introduce the following classification for porous solids, see Fig. 30, partly based on the definitions and terminology of Rouquerol et al. [421] for agglomerates and aggregates:

- (a) fabrics
 - (i) woven structures
 - (ii) non-wovens
- (b) agglomerates
 - (i) cellular structures
 - closed-cell structures
 - open-cell structures
 - random open-cell structures
 - regular open-cell structures (metamaterials)
 - (ii) matrix-dilute pore systems
- (c) aggregates, such as sand, crushed stone, recycled concrete, ...

3.1. Fabrics

We classify fabrics in two categories: woven and non-woven. The former is made by weaving, braiding, stitching or knitting, whereas for the latter, fibers are bonded mechanically, chemically or thermally into a random web structure.

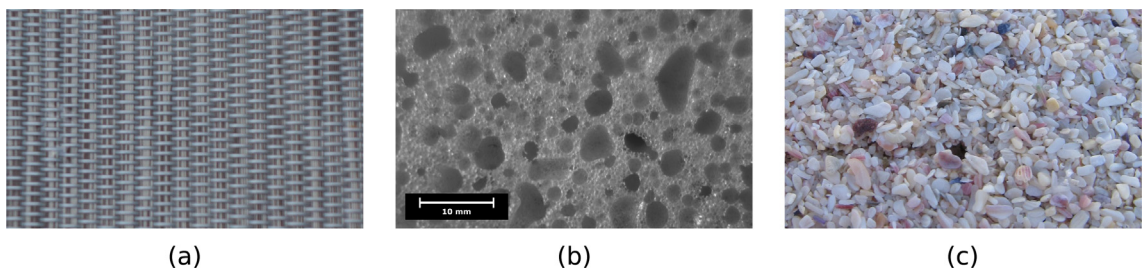


Fig. 30. Porous solids: (a) plain weave fabric, (b) sponge (agglomerate), and (c) sand (aggregate).

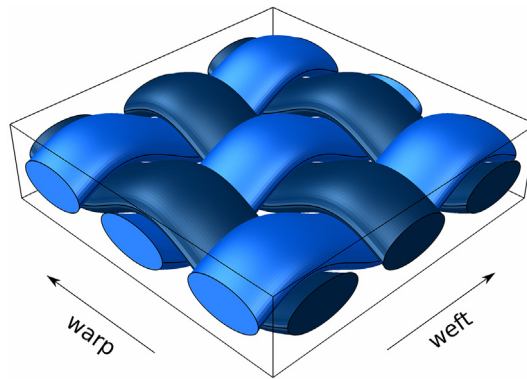


Fig. 31. In a woven structure, yarns running in processing direction are called warp while yarns running perpendicularly to the processing direction are called weft.

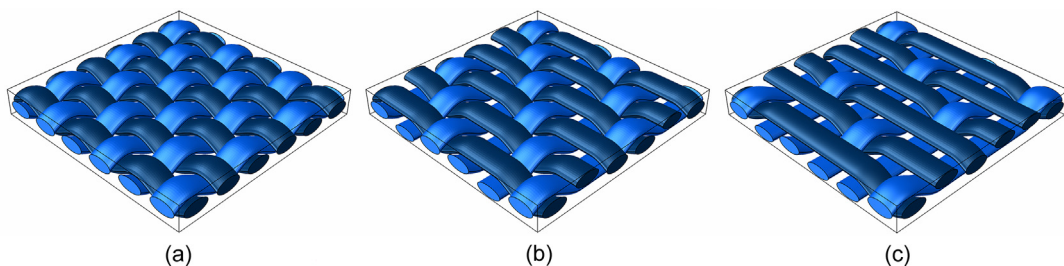


Fig. 32. The three basic types of 2D textile weaves: (a) Plain weave showing a criss-cross pattern. Warp and weft yarn are aligned in an alternating way. (b) Twill weave leading to a pattern of diagonal parallel ribs. Weft yarn is passed first over one or more and then under two or more warp yarns and so forth. (c) Satin weave exhibits a glossy surface and a dull back. In the applied warp-faced weaving technique, the warp yarns are passed over much more wefts than in twill.

3.1.1. Woven structures

Woven structures are characterized by a distinct hierarchy. Independent of whether a woven, braided or even stitched or knitted fabric is considered, the underlying building blocks are usually several yarns which themselves are made of fibers. These yarns can be distinguished based on their orientation with respect to the processing direction: warp yarns run in processing direction, weft yarns perpendicularly to it, see Fig. 31.

Examples of woven structures are plain, twill and satin weaves, see Fig. 32. In the case of plain weave, a criss-cross pattern is obtained by aligning warp and weft yarn in an alternating way. The smallest periodic RVE for this type of weaving consists of at least two warp and two weft yarns. A twill weave shows a pattern of diagonal parallel ribs obtained by passing the weft yarn first over one or more and subsequently under two or more warp yarns and so forth. The characteristic diagonal pattern is obtained by continuing this process for all weft yarns but with an offset to the previous row. In a satin weave, the warp yarns go over much more wefts than in twill leading to a very soft surface. A glossy surface and a dull back are characteristic for a warp-faced weaving technique.

Examples of a 3D woven structure are interlocked or interlaced fabrics. A review of modeling approaches in terms of micro-geometry for 3D woven interlock structures was given in [422]. Fang and Liang [423] provided an overview on numerical methods for braided structures, including a discussion of geometric modeling approaches and special aspects of mesh generation.

RVEs for woven structures either consist of the fabric alone or the fabric embedded into matrix material. Woven composites are space-filling, however, their RVE generation is primarily based on the geometry of the porous weave. Thus, they are discussed in this section.

3.1.1.1. Microstructure reconstruction from experimental data. A number of models for woven structures were created based on image information obtained by experiments, i.e., CT data [424–429].

Barbero et al. [424,430] approximated the fiber/matrix bundle in an RVE for plain weave fabrics. Based on digitization of photomicrographs, bounds of fabric are determined from cross sections (i) perpendicularly to the warp direction which also show the in-plane weave shape in the weft direction and (ii) perpendicularly to the weft direction which also show the in-plane weave shape in warp direction. Using this information, warp and weft are generated based on sinusoidal curves. These curves are adjusted to avoid intersections. A 3D model is built by modeling four half-yarns using the CAD-software I-DEAS

based on the 2D geometrical model of the cross-section curves described above, see also Fig. 34. A sweeping approach along path curves is not possible due to the fact that the evaluated curves for the weave at different cross sections do not match. Thus, the front face information is mirrored and copied to the back face before using a blending algorithm for the cross-section and path curves to define the yarn surfaces. For each yarn, three path curves and four cross-section curves are necessary to describe the surface. Small rotations of the yarns in the weft direction about the warp axis avoid any yarn intersection. This may lead to small gaps between the yarns which were subsequently treated as matrix material. Such an RVE represents a full wavelength in warp and fill direction, i.e., a periodic structure. The advantage of such an RVE is its simplicity as only a few measurements on micrographs are required for its generation. Still, it provides a good agreement with experimental results in terms of the mechanical properties, as illustrated in [424,430].

Sevenois et al. [431] determined yarn shapes and paths based on experimental data. Versatile shape functions are employed reproducing the weave geometry. Consequently, problems such as yarn intersection and mismatch in the volume fraction are avoided. The computational costs are rather low compared to methods presented in the following and the created geometry allows a direct application of meshing algorithms and periodic boundary conditions. This model was compared to a model created directly from μ CT X-ray data. In the latter approach, the cross section data points of each yarn are taken and connected using spline interpolation, see also [431]. By doing so, solid yarns are created which are assembled to the full fabric. The geometrical and μ CT based models are in good agreement, where the geometrical one is computationally significantly cheaper.

Based on μ CT scan data, Jacques et al. [427] investigated a 5-harness satin weave. First, the geometric information is identified from μ CT scans, which is subsequently used to create a model with the commercial CAD/meshing software CATIA which also allows the integration of flaws and faults of the material into the RVE. Complex geometries lead to single parts when importing a CAD model into a FE software. This might lead to meshes with non-identical surface meshes on opposing sides of the assembly which complicates the application of periodic boundary conditions (one way to overcome this problem is to approximate periodic boundary conditions for non-periodic RVEs [134–136]). The authors address this problem by constraint definitions at the interfaces between the different parts which are implemented into their software ORAS. The results are validated against models obtained via a combination of the more commonly used softwares WISETEX (see Section 3.1.1.4) and MESH-TEX as well as against experimental data. As these examples show, the generation of RVEs based on micrographs can be used to obtain elaborate as well as realistic structures. However, as soon as the full geometrical information is considered, challenges such as single parts, non-periodic RVEs or small geometric features, which are difficult to mesh, may arise. Therefore, a number of the discussed approaches considers geometrical methods, see Section 3.1.1.3, where the required parameters are identified from experimental micrographs, leading to simple models which may be sufficient for homogenization purposes. However, as soon as the local information within the structure is in the focus, e.g., crack propagation paths, idealized structures generated by geometrical methods are not sufficient and the full information of the experimentally obtained structure needs to be considered.

3.1.1.2. Physics based microstructure generation. What we classify as physics based methods is sometimes subdivided into kinematic and mechanical models when it comes to the generation of woven RVE structures [432]. Kinematic models are based on the simulation of the weaving process as well as post-processing steps such as compaction. These models account

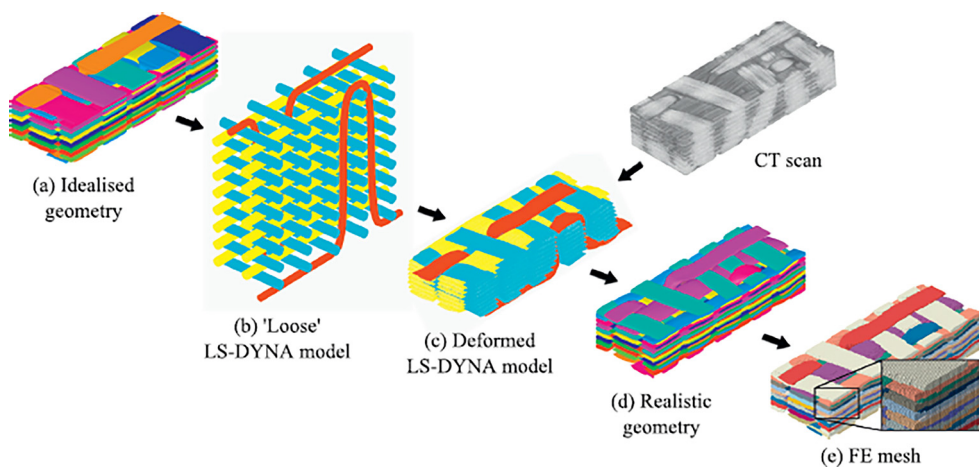


Fig. 33. Overview of workflow in the modeling process used in [435], including validation with a model based on CT data. (a) Creation of idealized unit cell of woven fabric using TEXGEN. (b) Generation of a loosely woven beam element model in LS-DYNA. The generation, meshing and application of boundary conditions is performed via Python scripts [435]. (c) Simulation of compaction to target volume fraction to obtain as-woven fabric (as-moulded composite). The resulting model is validated based on experimental CT data. (d) Conversion of model consisting of chains of beams into solid geometry model. (e) Meshing of geometry model to obtain finite element model. Reprinted from Composite Structures, 118, Green et al., Numerical modeling of 3D woven preform deformations [435], 747–756, Copyright (2014), with permission from Elsevier.

for contact between different yarns [432–437]. However, the actual mechanical behavior is not considered. In contrast, the mechanical model takes the mechanical behavior into account via a constitutive law. This allows the prediction of the final geometry of the fabric after processing including resulting pressures and forces [438,439]. Mechanical models are computationally more expensive than kinematic ones, but also more realistic. In some studies, a combination of geometric and physical modeling approaches is presented [440–442].

Green et al. [435] provided a workflow for the generation of a unit cell of a 3D orthogonal woven structure, see Fig. 33. Based on *TEXGEN* (see Section 3.1.1.4), a unit cell of the fabric is generated which is transferred to a *LS-DYNA* beam element model. One characteristic of their model is that each yarn is discretized by a bundle of chains of beam elements, making use of the multi-chain digital element method [443]. In the next step, loading is applied to the yarns to obtain an as-woven fabric. The desired volume fraction is obtained by compacting the model using rigid plates. Finally, a solid geometry is deduced from the chains of beam elements. The results of the approach in terms of accuracy are compared to μ CT scans of a dry specimen of the fabric.

Isart et al. [444] compared three generation strategies for 3D orthogonal interlock structures: an idealized representation of the geometry based on *TEXGEN*, a kinematic model based on the digital element method [443] and an analytical method [445] requiring measurement data from the fabric. The digital element method as well as the analytical method lead to more accurate descriptions of the geometry based on a comparison to experimental results in terms of tomography scans and elastic parameters. The idealized geometry is the fastest method in their study, however, shows deviations from experiments.

The presented physics based microstructure generation examples for woven structures allow for the simulation of realistic internal yarn structures that strongly depend on the manufacturing process. Therefore, such generated RVEs are more realistic for the investigation of local properties and behavior such as damage propagation.

3.1.1.3. Geometrical methods. In geometrical approaches, the geometry is constructed based on analytical or (relatively) simple geometric considerations [424,446–453], i.e., leading to parametrical solid models. Further, geometric approaches might be based on specific geometric rules, i.e., the yarn path has to follow certain restrictions to avoid interpenetration [454–458] or contact algorithms to avoid penetration [459–461]. For certain structures, such as braided textiles, the different present components of the textile, i.e. interlaced and bias yarns, are often modeled separately based on geometric considerations and afterwards assembled to form a braided structure showing a specified braiding angle and spacing [462,463]. As noted by Lomov et al. [447], geometrical methods can account for local variation in textile geometry, i.e., permeability, in an explicit way.

Plain weave: Most geometrical modeling approaches deal with plain weave fabrics [446,464,451,465]. Kuhn and Charalambides [446] considered composites with a polymer or ceramic matrix which show strong differences for the space between the bundles. The authors approximated the woven composite as a four layer laminated composite [446], where all four yarns are identical. The yarns are described by piecewise continuous functions. The cross-sections of the yarns are generated as sinusoidal top and bottom profiles with sharp points at the edges. Additionally, a sinusoidal periodic undulation of yarns is assumed. The in-plane width of yarns is modeled as constant along the longitudinal direction. The area of the cross-section remains constant along the yarn, but its shape strongly depends on the arrangement of the yarns. A fiber/matrix bundle in a 3D RVE for plain weave fabrics (depicted in Fig. 34) can be approximated based on a periodic 2D model described by four sinusoidal functions, one for each RVE face [424], see Fig. 34.

Brown et al. [464] presented a systematic approach to generate a model based on a 2D plain weave structure, assuming ideal connections between individual yarns. First, a yarn cross-section is created by using a rectangle of desired length and height in combination with a three point arc to construct the wireframe of the assumed lenticular shape. Based on the

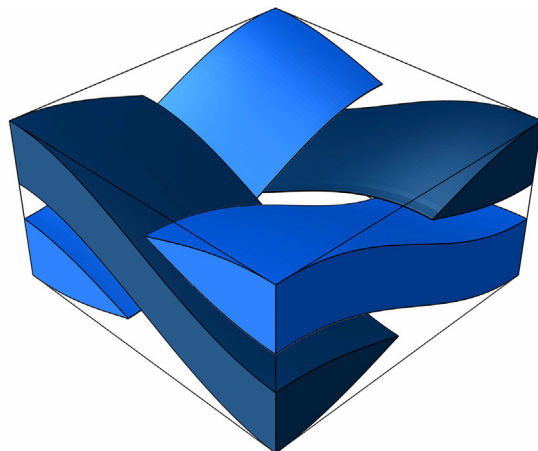


Fig. 34. Plain weave fabric RVE: Yarns are approximated by sinusoidal functions, as e.g. done in [424], where only a half wavelength is depicted.

identification of an appropriate yarn path, the two profiles are positioned to create a solid yarn. To assemble the RVE, the individual instances are incorporated by rotating and moving them until the desired orientations and positions are obtained. Within the proposed systematic approach, woven fabrics are created based on a common data source and a solid model of the fabric is automatically created [464]. The basic data in terms of the weave pattern is generated with XSection, coupled to the software SCOTWEAVE [466]. This information has to be supplemented with loom setup data to create the woven fabric, enabling the generation of a solid model of the fabric (based on I-DEAS) afterwards. The main advantage of such RVE modeling schemes is that gaps and intersections are easily avoided - leading to RVEs which are simple to generate, mesh and calculate computationally, however, providing less realistic geometries.

Kowalczyk [451] proposed an enhanced model for plain weave fabrics that preserves constant yarn cross-sections for undulated yarns, including much more geometric details of the yarn-to-yarn interface such as variable thicknesses between intersecting yarns and a local alignment of yarn's principal direction of transverse isotropy with fiber axis direction. The RVE is based on an analytical description for warp and weft yarns. One key assumption is the transformation of the yarn's central axis into a sinusoidal shape around which the yarns freely shape and the undulation is only restricted by neighboring yarns.

Twill weave: Stier et al. [467] generated an RVE of a twill weave ply, see Fig. 35. The determination of the elastic properties of the yarns is based on an additional RVE of perfectly aligned fibers in a hexagonal dense packing. In the RVE for the twill weave ply, the material orientation of the homogenized yarn is defined according to its sweep direction.

Multiple weavings: Hivet and Boisse [454] presented a geometrical model suitable for multiple shapes and weave types (plain, twill, satin), based on up to seven parameters, representing yarn width, yarn density, yarn weaving in each direction and thickness of the fabric. The yarns are created by sweeping the cross-section along a trajectory, allowing variation of cross-sectional shapes based on control sections and points. This is ensured by a smooth interpolation between the control sections using the “swept blend” feature in PROENGINEER. The developed model captures realistic contact surfaces between yarns and a varying cross-section shape along the yarn trajectory.

For twill and satin patterns, Adumitroaie and Barbero [449] proposed a general approach for models at ply level based on geometrical parameters defining the individual yarn geometry as well as weaving pattern of the fabric. New geometric functions, i.e., undulation and cross-section shape, are introduced which cover the current configuration of the composite. For the description of a braided composite, Zhang and Xu [468] used three unit cells to represent interior, surface and corner regions to investigate the distinct different properties of the composite at these positions. Tal and Fish [469] used statistical image information for the creation of statistically equivalent RVEs.

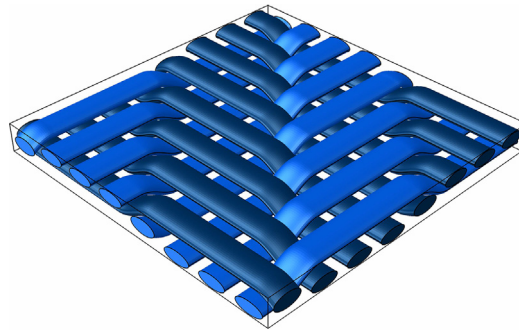


Fig. 35. RVE of a twill weave ply as used by Stier et al. [467].

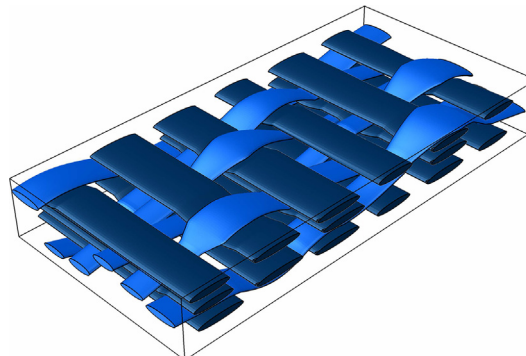


Fig. 36. Unit cell of an interlock fabric as used in, e.g., [460].

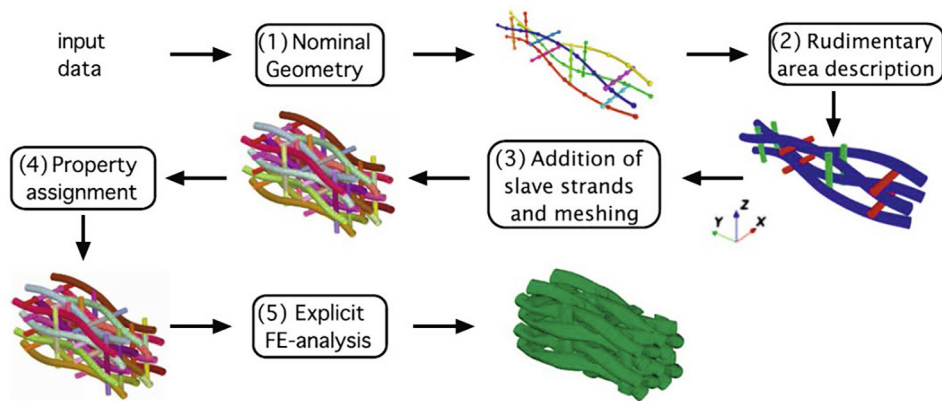


Fig. 37. Sequence of proposed modeling framework by Stig and Hallström [440] leading to a 3D woven textile RVE. First, `TEXGEN` is used to create a nominal periodic geometry. By using spline functions, which are defined between designated master nodes, the yarn paths are specified. In a second step, yarn cross-sections are defined at each master node leading to a rudimentary area description. Yarn cross-sections are initially assumed to be circular and constant as well as sufficiently small to avoid penetration. In the case of interpenetration, the cross-sections are uniformly reduced until no overlap remains. In a third step, the geometry information is transferred to a mesh generator to create periodic surface meshes of the yarns. Periodic contact conditions are achieved by adding slave yarns outside of the RVE. Next, kinematic couplings are defined to ensure periodic contact conditions. In order to expand the tubes, fluid flux is used via `ABAQUS/Explicit` with a general contact algorithm. To simplify the subsequent volume meshing, small gaps are introduced between the yarns which ensures no interpenetration and contact clearance. Reprinted from *Composite Structures*, 94(5), Stig and Hallström, Spatial modeling of 3D-woven textiles [440], 1495–1502, Copyright (2012), with permission from Elsevier.

An iterative strategy for the creation of a yarn structure of high density interlock unit-cells is presented in [460], accounting in particular for weaving, lateral and longitudinal contacts. The iterative strategy ensures consistency and prevents interpenetration at contact areas between yarns as well as a variable yarn section shape, see Fig. 36.

Stig and Hallström [440] presented an approach for the internal geometry generation, including path and cross-section variation of the yarns, see Fig. 37. The yarn perimeters are approximated as inflatable tubes. To avoid intersections, tubes are first constructed in `TEXGEN` in a rough manner where the geometry is small enough to avoid any intersection. For example, this is achieved by uniformly decreasing the cross-section of the yarns until no penetration remains. Afterwards, the yarns are treated as hollow cylinders and expanded until the correct volume fraction is reached, accounting for contact between the yarns. Subsequently, the geometry is exported to a mesh generator to create periodic surface meshes. The information of the surface mesh is subsequently used in the expansion process to track the contact conditions between the yarns. The synthetically created woven structure is validated by comparison to 3D tomography scan data.

With geometrical methods, RVEs of different complexities and levels of detail can be generated. Methods based on strong idealizations provide efficient tools for simplified RVEs which may be sufficient for homogenization purposes. If the focus is on local investigations more realistic geometrical approaches, e.g., considering contact, are required. Generating detailed RVEs with geometrical methods is still less computationally expensive than for physics based models (see Section 3.1.1.2).

3.1.1.4. Software tools. The software tools `WISETEX` and `TEXGEN` allow for generating textile RVEs based on geometrical methods. `WISETEX` [470–472] is an integrated design tool to model the internal microstructure and deformation of textiles. The software is based on a generalized description of the internal structure of the textile reinforcements at the unit cell level. The yarn's cross-sectional area is assumed to be constant. A unified description is used for the deformed and undeformed internal geometry of the fabrics. The yarn path is determined by minimizing the bending energy of the yarns inside the considered volume accounting for the designed weave pattern and assuming the stable state of the fabric. The weave patterns are described by a matrix coding algorithm. Afterwards, the yarns are decomposed into elementary crimp intervals. For each interval, the weft crimp heights (in-plane and out-of plane) are determined and subsequently used for reconstruction of the yarn geometry with a spline approximation solution. Models without interpenetration are constructed, however, this is not guaranteed [473]. The finite element model is generated by meshing the yarn volume with a sweep-meshing technique, using the mesh of the cross-section of the yarn. This results in a regular mesh for the yarn. To eliminate possible mesh penetrations, three steps are performed. First the yarns are separated, then a resistant media is placed between the yarns before compressing them together. By this, the initial positions of the yarns are found [471].

`TEXGEN` is an open source software based on a generic approach for all types of woven textile structures [456,474]. One specific feature is that local cross sectional changes of shape and size are admissible. This is done by a software feature for interference correction, avoiding penetration of yarns. The geometry is generated by an independent specification of yarn path and yarn cross sections. The yarn path is mathematically described by a spline and is usually determined by parameters such as fabric structure, yarn cross section, yarn spacing or fabric thickness [474]. For instance, the yarn path is interpolated from measured points from experimental micrographic images [473]. Zeng et al. [475] presented a procedure for the creation of a unit cell model in `TEXGEN` which accounts for a systematic local variation in yarn path and cross section to represent

orthogonal carbon fiber weaves. The initial yarn cross section is modeled in *TEXGEN* as constant with different possible forms, i.e., circular, elliptic or lenticular. The yarns are represented as solid volumes by *TEXGEN* where the total volume consists of individual sections which are defined at each control node of the spline, representing the yarn path. At each of these nodes, the cross sectional geometries are defined locally to account for experimental measurements or specific targeted variations. In addition to the classical symmetric shape of the cross section, *TEXGEN* allows the assignment of hybrid shape functions to account for asymmetries. The yarn surface is defined based on the yarn path and cross section. To create a yarn volume, the series of individual sections are combined for each yarn in the considered unit cell. However, as this procedure is often computationally inefficient, *TEXGEN* works with so-called centerlines which describe the yarn path with superimposed cross sections. Additionally, the toolbox provides the possibility to act as a pre-processor for finite element simulations, including mesh generation, contact definitions, material orientation and boundary conditions.

3.1.2. Non-woven structures

Non-woven fabrics can be described as manufactured sheet or web structures of random long fibers [476] that are bonded either mechanically by entanglement, chemically, or thermally, that is, through localized melting and resolidification. Possible fiber materials are manifold, however, most often, natural or polymer fibers are employed. By variation of the materials, bonding mechanisms or bond spot and fiber densities, non-wovens are tailored to different requirements, resulting in application cases ranging from hygiene and medical cloths over fire-protective linings and building materials to highly specialized filtration systems.

Non-woven fabrics are employed as filter materials because they allow to form mechanically stable structures with extremely high porosity resulting in a high permeability. Careful design of a non-woven fabrics' microstructure further allows to optimize pore sizes (and, therefore, the transport properties) as well as other functionalities such as thermal and electrical conductivity. Due to this versatility, non-woven filters are utilized, e.g., in advanced particle filters [477,478] and as gas-diffusion layers in fuel-cells [337]. To facilitate optimization of these materials, understanding the correlation between microstructure and functionality and, therefore, accurate models of the microstructure are crucial.

Non-wovens are structurally similar to the fully random distributions of wavy fibers discussed in Section 2.3.3.2. Therefore, it stands to reason that some of the principles discussed there could be employed in RVE generation for non-wovens as well. However, these microstructure generation mechanisms are generally not able to account for the high number of fiber contacts and the large fiber curvature necessary for web formation in non-wovens.

The complexity of a single fiber's morphology and the convoluted nature of the whole microstructure make straightforward geometry descriptions difficult. Therefore, many approaches exist that aim to reconstruct non-woven microstructures from experimental imaging techniques.

3.1.2.1. Microstructure reconstruction from experimental data. Investigating the microstructure of non-woven fabrics with classical 2D imaging techniques such as optical microscopy or scanning electron microscopy (SEM) is a difficult task as, due to the high void volume, information from different material depths is conflated. This loss of information makes fiber identification and image post-processing increasingly difficult. Confocal microscopy could be used to mitigate this problem but is only applicable for limited depths [479] and still requires extensive interpolation for overlapping fibers.

Sambaer [480] automatically extracted the top layer of a nanofiber based non-woven from a 2D SEM image. Conditions for successful fiber identification in post-processing such as good contrast and viewing angles are outlined. The 2D fiber structure recovered with this method is then used to generate an artificial 3D structure by stacking multiple rotated copies of the 2D layer. Using this technique, realistic pore channels can be modeled, but the mechanical properties of the non-woven cannot be studied as connections and entanglements between layers are neglected.

To capture full 3D information, such as the interconnectivity of whole networks with 2D imaging techniques, serial sectioning methods are applied. As these are based on the removal of thin slices inbetween the imaging steps, they cannot be applied on a non-woven without sample preparation that stabilizes the structure. Mechanical cutting is made possible by embedding the non-woven into a matrix material such as a polymeric resin [481] that holds the fibers in place during cutting. Embedding the sample in a second phase requires care, as complete filling of the void space is required and flow of the impregnating resin within the network causes movement of the fibers. This alteration of the microstructure can be minimized by skilled and experienced experimentalist, but it is impossible to guarantee a completely unaffected microstructure.

Non-destructive imaging of non-woven microstructures is performed using imaging techniques based on transmissive radiation, compare Section 2.1.1.1. Hoferer et al. [477] employed magnetic resonance imaging (MRI) as known from medical applications to study the structure and particle deposition within a polymer fiber filter. While the non-destructive nature of this method is promising for in situ studies, it requires the void space to be filled with water as the fibers themselves do not provide a sufficient signal. Using this workaround, the void space is measured and the fiber structure is recovered as its inverse. Immersing the specimen in water may alter the microstructure before imaging and requires elaborate specimen holders. With this setup, static high-definition imaging allows resolutions of up to 59 μm at a measuring time of 8 h. For in situ measurement, the measuring time has to be reduced considerably, resulting in significant deterioration of the image resolution.

Imaging using X-ray tomography in contrast is non-invasive and allows for 3D imaging of a non-woven microstructure at resolutions of a few micrometers [482–484], compare also Section 2.1.1.1. Despite the possible resolutions being much better than in MRI, μCT measurements may still be insufficient for non-wovens, as the fiber diameter especially in advanced materials may be significantly smaller than the resolution limit [482].

3.1.2.2. Physics based microstructure generation. Numerous fabrication processes for non-wovens exist, depending on the material and the bonding type. One common process route is aerodynamic web forming, in which the fibers are released from a rotating drum or, in the case of some polymer fibers, directly from the melt spinning process into highly turbulent air flows in which they are entangled. These entangled fibers are then deposited onto a moving conveyor belt to form a 3D web structure. Further post-processing steps such as compression or thermobonding are possible.

Describing this whole process mathematically is too complex but modeling process steps can provide valuable insights into the microstructure generation. Klar et al. [485] presented a stochastic 3D surrogate model for the lay down of the fibers on the conveyor belt in which the deposited fibers are described by an arc-length parametrized curve. The model includes parameters accounting for physical properties of the fibers such as their stiffness and coiling behavior, and takes process parameters (turbulence influence on deposition topology, machine geometry, conveyor belt speed, etc.) as an input. Furthermore, the framework allows to include different degrees of anisotropy, frilling and crimping of the fibers and thermobonding by identification of contact points [486]. The parameters determining the material, process and structure evolution behavior need to be determined from experiments or, partially, from simulations of turbulent flow dynamics [486]. The high number of parameters is necessary to achieve realistic microstructures but requires elaborate experiments and extensive studies of the parameters' influence.

3.1.2.3. Geometrical methods. When artificially generating a microstructure, certain geometrical simplifications are introduced depending on the method applied. Often, these simplifications are quite significant, a drawback that is commonly balanced by considerable reductions of the method's complexity and computational overhead. Therefore, the suitability of any microstructure generation technique depends not only on the material at hand but also on the type of information one is interested in. For example, some descriptions of non-woven microstructures neglect interconnectivities of the fibers in one spatial direction [480,487] which makes mechanical investigations impossible but is admissible when one is interested in the flow behavior along this direction. Similarly, the different bonding types in non-wovens lend themselves to different structural simplifications.

Some thermobonded non-wovens are bonded by local melting and compression of the fibers by a hot calender. This results in a generally regular pattern of bond spots within the randomly oriented fiber sheet. Mueller and Kochmann [488] used this basic structure to generate 2D RVEs for non-woven sheets consisting of a regular grid of plates, representing bond spots, that are connected by fiber bundles modeled as trusses. The orientation of these trusses can be random, based on orientation distributions determined in experimental studies [489]. RVEs generated with these methods are two-dimensional but the same principles could certainly be employed in building 3D structures.

To study a 3D structure in which fibers bond across different layers, approximating mechanically bonded non-wovens, Niskanen and Alava [490] introduced an algorithm in which initially straight fibers are positioned and oriented randomly within a plane before being lowered onto a substrate. The fibers are lowered one after the other and are kept straight and parallel to the substrate until first contact with a subjacent fiber. Upon contact, the fiber is deformed to lower parts of the fiber further. The degree of bending, i.e., the fiber's stiffness, is controlled by a user input deflection constraint. With this method, an interconnected, randomly oriented fiber structure can be modeled. However, it does not allow for the typical looping and entanglement of non-woven fibers.

Methods allowing to generate microstructures of wavy entangled fibers have already been discussed in Section 2.3.3.2. While such methods [419,415,417] could be used as a good approximation for non-woven structures, the degree of curvature possible is significantly lower than what is expected for non-wovens. Microstructures with arbitrarily large fiber curvatures and even looping can be generated with the algorithm presented in [337]. To allow for these large curvatures, the fiber path is represented by a random polygonal track based on multivariate time series. Fibers described by these paths are placed randomly within a volume, without preventing overlaps. This structure is in a second step transformed into a non-overlapping one using a force-biased fiber packing algorithm [419], compare Section 2.3.3.2. A higher degree of curvature is possible in this technique, however, it goes along with a loss of control over fiber orientations and structure anisotropies as compared to [419]. The choice of a geometrical generation method for non-woven fabrics is, therefore, not straightforward and requires careful examination of the admissibility and influence of the introduced simplifications.

3.2. Agglomerates

As agglomerates, we consider porous materials which are consolidated, existing as relatively rigid, macroscopic bodies whose dimensions exceed those of the pores by many orders of magnitude. We divide these into two groups depending on the relative density ρ^*/ρ_s where ρ^* denotes the density of the agglomerate and ρ_s represents the density of the solid phase. Materials with relative density smaller than 0.3 are referred to as cellular materials [266]. These materials encapsulate certain mechanical, thermal and acoustic properties, such as high strength to weight ratio, low thermal conductivity, and relatively higher sound absorption, desired for many engineering applications. Increasing the relative density requires thickening of the cell wall and a consequent reduction of the pore volume. Matrix-dilute pore systems which involve materials with isolated elliptical or spherical voids are studied in the class of porous media with high relative density. Through the presence of material discontinuities due to pores these materials share the mentioned mechanical, thermal and acoustic properties of cellular materials, however relatively less effectively due to their higher density.

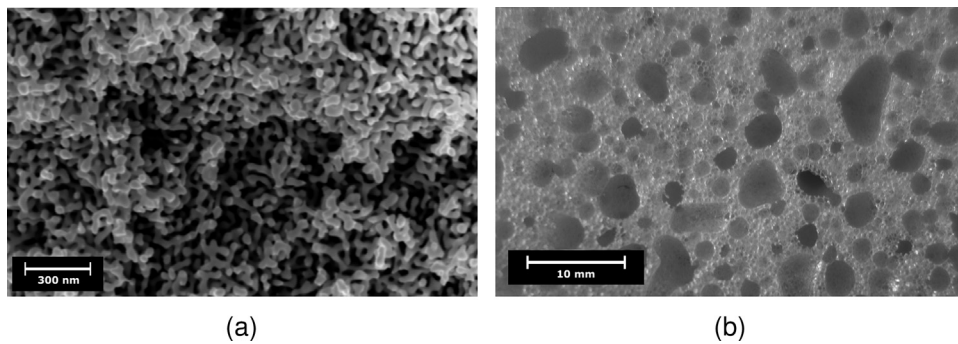


Fig. 38. 3D cellular materials: (a) Open-cell nanoporous gold (reprinted from Journal of the Mechanics and Physics of Solids, 99, J. Wilmers, A. McBride, S. Bargmann, pp. 163–177, [492], copyright 2017; Elsevier, with permission from Elsevier). (b) Closed-cell polyurethane.

Cellular materials are composed of mostly polyhedral cells with solid edges or faces [266]. Edge refers to “lines” connecting vertices, whereas face (resp. wall) refers to a “surface” of the polyhedra. If only cell edges exist in the material microstructure, we refer to these materials as open-cell. Microstructures containing cell faces sealing each cell off from its neighbors are referred to as closed-cell. Thus, in open-cell structures, it is always possible to find a way through the cells without penetrating the solid part of the material, whereas this is not possible for closed-cell materials. Most generally available cellular materials are foams which exist as open- or closed-cell structures, see Fig. 38. Certain materials involve a blend of open and closed cells and are, thus, of mixed type.

Cellular microstructures may emerge at various scales. For instance, in nanoporous open-cell metals, the pores are in the range of nanometers, whereas for natural sea sponges, the pores are in the range of millimeters. Further materials with cellular microstructures are, e.g., bone, cork, wood, plant stems, and other animal and plant tissues. The inherent 3D structural complexity of cellular materials has a strong influence on the effective mechanical, thermal and acoustic properties. This makes conventional analytical bounds on the corresponding effective properties too conservative [491]. Thus, 3D realistic models are required for an accurate evaluation of structure-property relations of cellular solids.

3.2.1. Cellular structures

3.2.1.1. Microstructure reconstruction from experimental data. Although the underlying fundamental idea of serial sectioning of cellular materials is the same as for polycrystals, the details are not straightforward. Most cellular structures, especially those with open cells, are inappropriate candidates for conventional serial sectioning techniques, composed of cyclic abrasion of material layers via grinding/polishing and imaging the newly exposed sections [493], due to their inherent sensitivity to local mechanical loading. However, for open-cell structures, stabilizing the load carrying network through polymer infiltration²² exploiting the structure’s percolation property allows application of serial sectioning²³.

Serial sectioning techniques are inherently destructive, and by that, their application is limited to static and ex situ microstructural investigations. On the other hand, non-destructive techniques such as computer X-ray tomography are more suited for investigation of dynamic microstructures and in situ phenomena at the scale above one micrometer [494]. Especially with their low overall absorption of X-rays as a consequence of their low density, cellular materials are optimal candidates for X-ray tomography. The non-destructive nature of this technique allows in situ visualization of deformation and failure mechanisms of ligaments and cell walls. The resolution of the tomography is crucial considering the scale of the relevant cellular microstructure and needs to be sufficiently high to resolve ligaments and cell walls [495]. In medium resolution microtomography, a resolution of the order of 10 μm can be achieved by using a classical micro focus X-ray tube as a source. In high-resolution microtomography, high intensity X-ray radiation is necessary in order to produce highly parallel beams which allow resolutions of the order of 1 μm [118]. Thus, many cellular materials with characteristic sizes above several micrometers constitute ideal candidates for X-ray tomography. For example, undeformed microstructures of polyurethane foam and local deformation mechanisms during a compression test are investigated by means of X-ray microtomography in [496]. Different closed-cell foams where the material ranged from metal, polymer and mineral (concrete) foams to even bread were investigated using X-ray tomography with a quantitative comparison through 3D image processing with corresponding finite element model development attempts [495]. In situ X-ray microtomographic studies on aluminum closed-cell foams under compression are reported in [497].

If the investigated material has features on the submicron scale which are inaccessible to the mentioned medium- or high-resolution X-ray microtomography, an alternative method to generate 3D information is using electron tomography

²² The polymer infiltration process itself applies mechanical loads with the volume change of the polymer during solidification to the ligament network which may cause some but not a substantial amount of damage.

²³ Closed-cell structures do not allow percolation due to the isolated nature of their pores. However, due to cell walls they are relatively more stable during serial sectioning.

in a transmission electron microscope [279,280]. High-angle annular dark-field scanning transmission electron microscopy imaging can be used for nanoporous gold foils with average thickness of 120 nm for 3D reconstruction of the microstructure [279]. The method allows binarized reconstructions with 3D voxel resolution even below 1 nm. Although providing very high spatial resolution in a non-destructive way, the applicability of the method is limited to very thin films.

For thicker samples, a powerful technique is FIB/SEM tomography, as described in the preceding sections. For example, 3D open-cell structures of nanoporous gold with a characteristic length scale as small as 40 nm are investigated in [98]. In order to supply structural stability by holding cut ligaments in place, the pores are infiltrated with epoxy (at room temperature) prior to the removal of material layers. Nevertheless, FIB milling may introduce surface relaxation or severe damage [498,499]. Moreover, due to its destructive nature, unlike conventional tomography methods, this method does not allow investigating dynamic microstructure and in situ experimenting. Investigation of coarsening in nanoporous gold microstructures over static microstructures of interrupted processes can be found in [100].

Finally, combining transmission X-ray microscopy using synchrotron X-ray sources with tomographic methods renders non-destructive observations with submicron spatial resolution (as low as 30 nm) for samples with thickness of the order of 10 micrometers [281,114]. This X-ray nanotomography method allows in situ morphological and topological property investigations of nanoporous metals with characteristic length scales as small as nanometers during coarsening or under mechanical loading [114].

For cellular materials, another technique for reconstruction of the 3D microstructures is magnetic resonance imaging. However, whereas the above methods apply equally to cellular materials with metal, ceramic or polymer solid phase, the use of magnetic resonance imaging is limited to polymers or open-cell ceramics filled with water.

3.2.1.2. Physics based microstructure generation. Considering man-made foams, different types of solids require different foaming techniques. For polymers, initial stages of foaming are based on growing and stabilization of gas bubbles introduced into the hot polymer [266]. For metals, various liquid or solid state processes exist. For foaming processes composed of liquid and gas, the evolution of foams is about modeling the evolving gas-liquid interface through stages of bubble nucleation, bubble growth and cell wall thinning with drainage, topological changes with bubble wall rupture and consequent bubble coalescence.²⁴ This requires simultaneous consideration of hydrodynamics, capillary forces and gravity [500]. A macroscopic field discontinuity and a sharp fluid-gas interface which is moving in time create fundamental challenges in the simulation. The large and strongly evolving interface makes the numerical treatment with standard CFD methods very difficult. To this end, a lattice Boltzmann approach in the treatment of free surfaces is proposed by Körner et al. [500]. Employment of underlying governing physics allows simulation of various experimentally observed complex phenomena such as: coarsening, solidification, drainage, self-organization in confined geometries, and avalanches.

A common method for modeling high quality nanoporous (open-cell) metallic microstructures is simulating the kinetics of phase evolution with phase separation during dealloying and coarsening via Ginzburg-Landau and Cahn-Hilliard equations [501,284,285,502]. MD simulations constitute one widely used numerical method for the spinodal decomposition process [287,288,503].²⁵ Usually, ab initio calculations are used to attain potentials used in MD simulations [504]. If a subsequent finite element analysis is planned with the developed microstructure, the point cloud data representing the atomic locations has to be converted to a solid model. Under certain circumstances, MD simulations are powerful substitutes of expensive experiments for determining effective properties of nanoporous metals, although the spatial and temporal scales in MD simulations are generally much smaller than those of the experiments [505]. Especially, the nano-second temporal scale of this method results in high computational times for the simulation of the microstructure evolution by dealloying and coarsening. A more efficient method which allows predictions at the meso scale is the kinetic Monte Carlo method. Kinetic Monte Carlo simulations, like in the case of MD simulations, work with a computationally generated discrete lattice of atoms. Unlike MD, however, the kinetics of these atoms are ruled by stochastic rate laws for diffusion and dissolution [506]. The kinetic Monte Carlo method has been successfully used to study the evolution of porosity during dealloying in, e.g., [507–509]. Findings of kinetic Monte Carlo simulations are in agreement with high-resolution elemental mapping observations conducted in a transmission electron microscope [509].

A computationally even more efficient method of modeling phase-separation dynamics (i.e., phase-ordering dynamics of thermodynamically unstable phases) is the use of cell dynamical systems [510,511,284] such as coupled maps and cellular automata (cf. Section 2.1.1.2).

3.2.1.3. Geometrical methods. Cellular materials such as nanoporous materials, foams, bone or microemulsions are non-particulate and, therefore, cannot be modeled as a distribution of cavities in a matrix [61].

The simplest geometrical methods for agglomerates involve cell models. For regular and periodic structures, a periodic building constitutes the RVE. This is generally the case for metamaterials.

Metamaterials are man-made, usually periodically microstructured materials with at least one non-natural property such as negative electric permittivity or negative Poisson's ratio. The overall properties are designed based on the material's

²⁴ Similar end geometries are also formed in food products made by frying starch containing biopolymers.

²⁵ All three sources used MD simulations for modeling spinodal decomposition, however, the initial RVEs were generated based on the lattice Monte Carlo method [287], reconstruction from nanotomography [503] and phase field method [288].

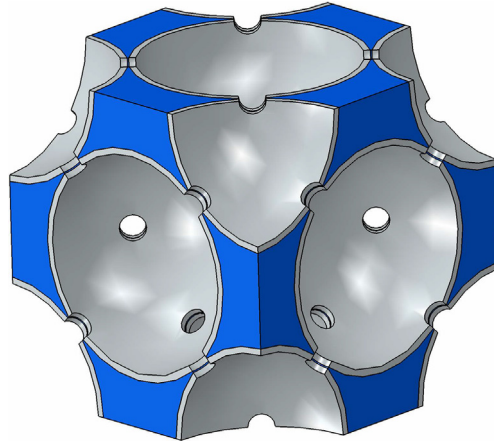


Fig. 39. Unit cell of inverse opal structure (SiO_2) with silica coating [512].

microstructure in terms of its structure rather than composition. In this regard, the RVEs are all generated based on geometric modeling approaches.

An inverse opal metamaterial with a coating based on the inverse of an fcc crystal geometry is depicted in Fig. 39. This material possesses high specific strength and modulus which can be further extended by an optimized architecture offering tunable optical bandgaps and large-area fabrication simultaneously [512]. The geometry of the employed unit cell is set up via CAD techniques in ABAQUS. Bonding between the coating and the inverse opal structure is obtained via surface constraints.

The concept of metamaterials allows the design of novel properties in engineering materials on the basis of targeted manipulation of their microstructure [513]. In contrast to classical materials, auxetic materials show an increase in lateral dimensions when elongated leading to a negative Poisson's ratio. Lakes [514] presented the first reported auxetic material produced from open-cell polymer foams leading to a foam with re-entrant (folding) structure. Rather than working with re-entrant structures, the bucklicrystals introduced by Babae et al. [515] are based on instabilities leading to large geometric non-linearities due to elastic buckling and show a negative Poisson's ratio. An ideal building block to design 3D auxetic metamaterials is provided by a unit cell which is capable of isotropic volume reduction [515]. These building blocks represent patterned spherical shells with different hole arrangements, a structure previously introduced as buckliball [516], see also Fig. 40. Only five patterns with 6, 12, 24, 30 and 60 holes are possible for the construction of RVEs of such crystals, leading to two symmetry groups: octahedral (6, 12, 24 holes) and icosahedral symmetry (30, 60 holes). The number of connection sites is limited as building blocks need to be attached to each other.

For example, the fcc RVE proposed by Babae et al. [515] consists of one-eighth building blocks at each corner and half building blocks at the middle of all six faces, see Fig. 40(b). The collapse of every building block is promoted by mechanical instabilities leading to a volume reduction transforming the cubic RVE into a rectangular periodic parallelepiped RVE with ellipsoidal holes. In terms of the stress-strain behavior, bucklicrystals show a behavior typical for cellular solids: an initially linear elastic regime followed by almost a stress plateau. The behavior change is associated with a mechanism shift due to buckling.

3D metamaterials, in which the concept of buckling induced pattern switch is the physical basis for the negative Poisson's ratio (extended to large strains), can be based on a very simple initial geometry [517,518]. The initial geometry is a cube in

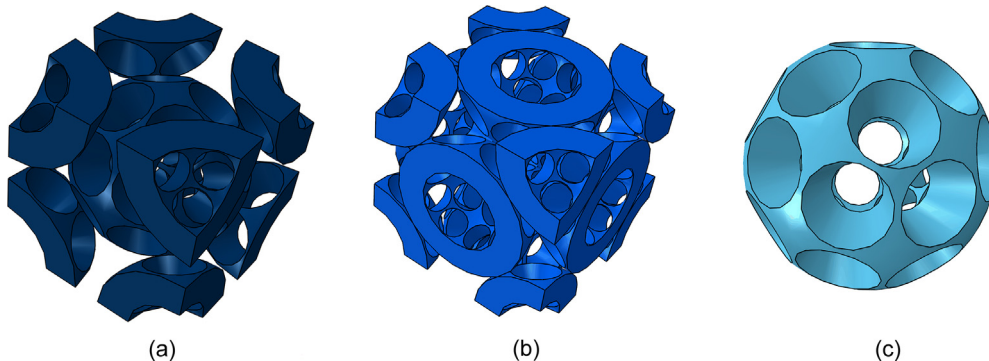


Fig. 40. (a) RVE of bucklicrystal with body-centered cubic symmetry. (b) RVE of bucklicrystal with face centered cubic symmetry. (c) Both structures are made of this anisotropic building block with 24 holes. Such RVEs were proposed by [515] and the initial bucklicrystals by [516].

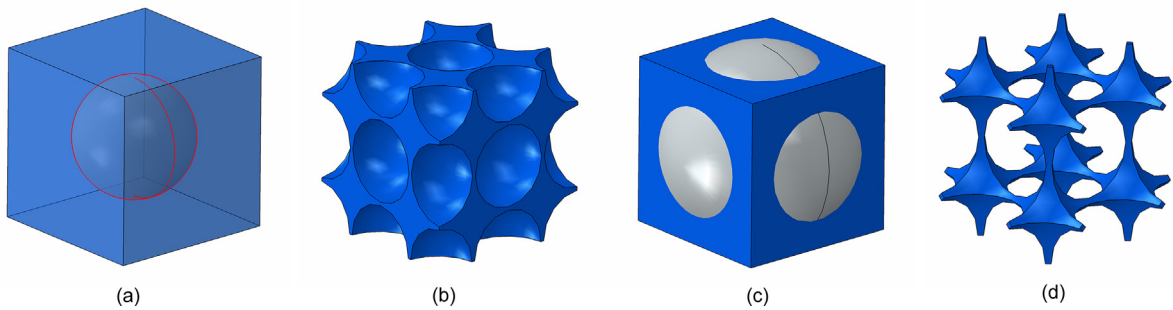


Fig. 41. The initial geometry design is based on creating a cavity within a cube based on spherical voids [517]. The RVEs consist of eight building blocks leading, depending on the sphere's radius, to either face-centered cubic (fcc) or simple cubic crystals. (a) Building block for a fcc cell; (b) RVE of a fcc cell. (c) Building block for a simple cubic cell. (d) RVE of a simple cubic cell. Structures constructed following the approach in [517].

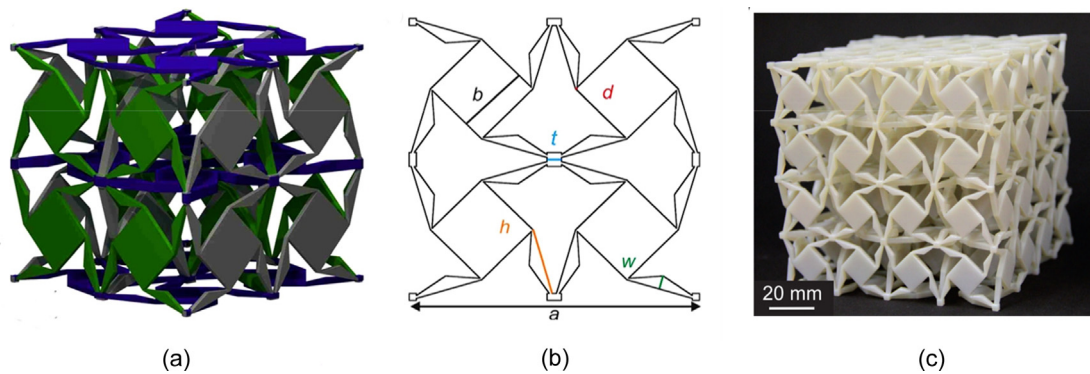


Fig. 42. 3D dilational metamaterial [519]. (a) Unit cell made of squares and triangles arranged in a checkerboard pattern. (b) 2D illustration of one plane of the unit cell to illustrate the relevant geometrical parameters: cubic lattice constant a , block size b , width of the holding element w , layer thickness t , holder length h and connection size d . (c) Picture of additively manufactured macroscopic specimen of dilational metamaterial, consisting of $2 \times 2 \times 2$ unit cells. Figures reprinted from [519], under the terms of the Creative Commons Attribution 3.0 licence. <http://creativecommons.org/licenses/by/3.0>.

which a cavity is created based on a hollow sphere. Controlled by the dimension of the sphere compared to that of the cube, fcc or simple cubic cells are created. The RVE is constructed based on eight building cells, see Fig. 41. The RVEs are altered by incorporating patterns of imperfections into the structure. Variations of volume fraction and magnitude of imperfections lead to different negative Poisson's ratios. Substituting the basis elastomer by a ductile metal initially leads to loss of the auxetic behavior. This can be compensated by incorporating different patterns of imperfections [518].

The structure for auxetic materials introduced by [519] and presented in Fig. 42 allows for identical lateral and vertical contraction under load leading to a Poisson's ratio of -1 . It is based on a 2D model presented in [520]. The unit cell consists of square and triangular elements which are connected by very small internal connections and arranged with its mirror representations in a 3D checkerboard pattern. This pattern prevents undesired trivial modes of deformation, such as simple translation of the squares. The small cubes connecting the triangles, see Fig. 42(b), do not contribute to the mechanical behavior, however, are required for experimental measurements. The cubic unit cell as shown in Fig. 42(a) is geometrically

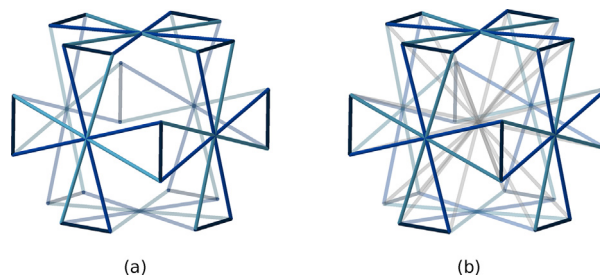


Fig. 43. 3D lattice structures for auxetic materials as proposed by Cabras and Brun [523]. (a) Unit cell of cubic lattice. (b) Unit cell of isotropic lattice where a system of additional diagonal elements (grey) is introduced into the cubic lattice.

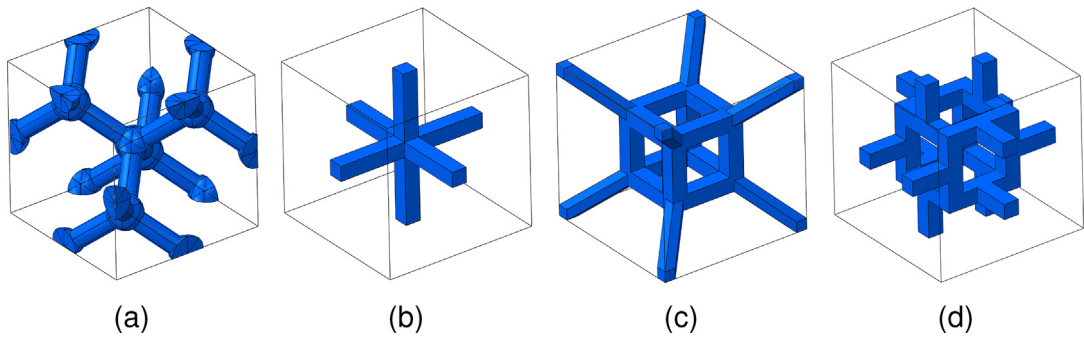


Fig. 44. Some idealized unit-cell-based microstructures for open-cell materials: (a) diamond cubic unit cell [529,530], (b) cross unit cell (variants of cross unit cells with mass agglomeration at the junctions are investigated, e.g., [527,528]), (c) extended cross unit cell, (d) Gibson-Ashby unit cell [526,266]. These models can easily be generated making use of a set of parameters and trigonometric relations.

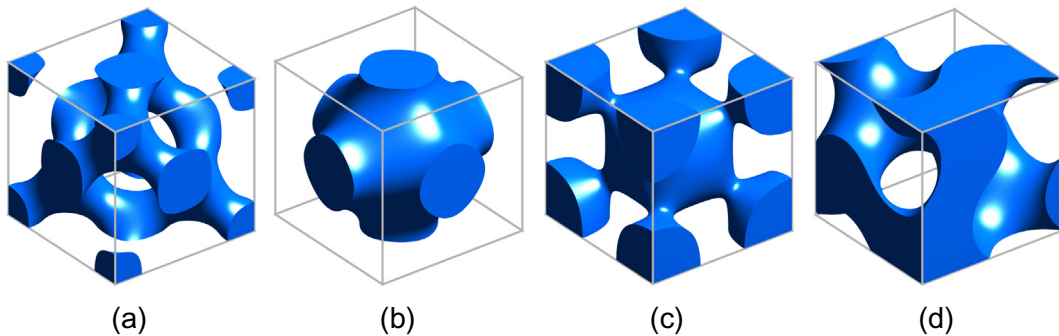


Fig. 45. RVEs of triply periodic minimal surface-based open-cell microstructures. The free surface is represented by: (a) Schwarz-D level surface (diamond); (b) Schwarz-P level surface (primitive); (d) the G level surface (gyroid). The analytical expressions making up these implicit surfaces are given in Eq. (5). For bicontinuous composites generated using identical minimal surfaces the reader is referred to Fig. 15. Their representability in simple analytical forms and triple-periodicity make these unit cells elegant alternatives to those listed in Fig. 44. In addition, their smoothness avoids stress concentrations triggered by sharp corners.

modeled via the CAD COMSOL Kernel. Although this structure is 3D, their geometrical considerations are primarily 2D. The same holds for 3D auxetic structures of honeycomb type [521,522].

Cabras and Brun [523] presented another class of 3D lattice structures for auxetic materials exploiting the modification of omni-directional Poisson's ratios close to -1 . The proposed unit cells consist of slender cross-shaped elements which are linked at their central points and connected by trusses at their end points. A cubic, Fig. 43(a), as well as an isotropic lattice, Fig. 43(b), are constructed. The latter is obtained from the cubic one by introducing additional diagonal cross-shaped elements which are considered as Euler beams. The tessellated structure is generated in COMSOL with half of the unit cell shown in Fig. 43(a). The final investigated cubic lattice consists of $2 \times 2 \times 2$ unit cells. The joined elements at the central points are kinematically coupled in a way such that only homothetic expansion or contraction deformation modes are possible [523]. The cubic lattice leads only for some directions to negative Poisson's ratios. To overcome this limitation, diagonal beam elements as well as one additional lattice point in the center of the unit cell are added, leading to an isotropic auxetic lattice, see Fig. 43(b). The beam elements are constrained such that they exhibit the same displacement at the central point, where a hinge was introduced. The topology of the microstructure in conjunction with the stiffness contrast of the used elements leads to an auxetic behavior close to the stability limit of the Poisson's ratio.

Porous solids with random cellular structures: By disregarding the inherently random cellular nature of the microstructure, the simplest approach seems to be the deterministic periodic unit (open-)cell-based idealizations.²⁶ These involve heuristic constructions, see, e.g., Fig. 44, or constructions of (analytical) level surfaces, e.g., triply periodic minimal surface-based unit cells, Fig. 45. The oldest of such models is the so-called Kelvin model [524] which consists of a regular packing of tetra(kai) decahedra. Waire and Phelan [525] improved this model to involve different types of cells which are dodecahedra and tetradeca(hedra). The model of Gibson and Ashby [526,266] is among the most widely used idealized unit cells for metallic foams as well as nanoporous metals. Various proposals for alternatives were made since then: e.g., modified

²⁶ The periodic unit cells readily satisfy the requirements of a representative volume element if the underlying structure is also periodic, e.g., regular honeycombs.

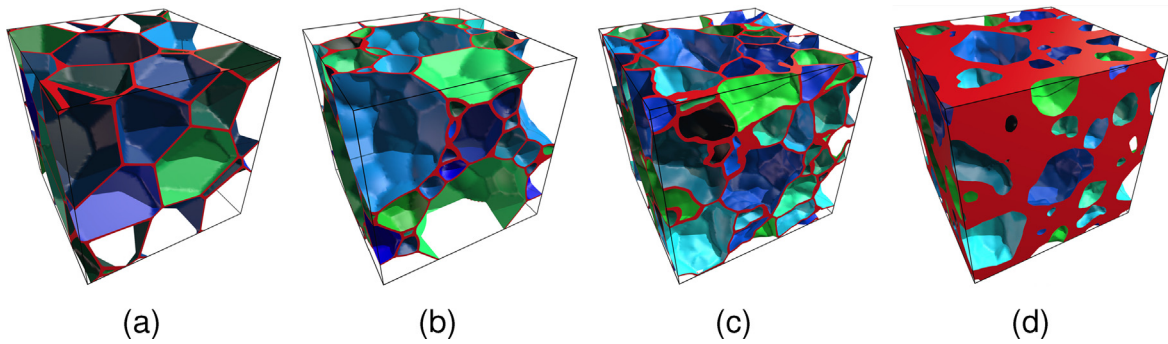


Fig. 46. Closed-cell foam microstructures generated from (a) mono-sized sphere packing, (b) multi-sized sphere packing and (c) and (d) arbitrary-shaped inclusion packing with different thickness values. Figure reprinted from Computational Mechanics, An advanced approach for the generation of complex cellular material representative volume elements using distance fields and level sets [538], 56, 2015, 221–242, Sonon et al. (original copyright notice as given in the publication in which the material was originally published). With permission of Springer.

rectangular unit cells [527,528] considering agglomeration of the mass in junctions or periodic diamond cubic unit cells [529]. However, as depicted in Fig. 44, mostly these idealizations involve ligaments with rectangular cross sections and discontinuous surface normals which do not meet reality.

As a remedy, triply periodic minimal surface²⁷-based open-cell structures can be used, see Fig. 45. Their smooth surfaces allow incorporation of theories accounting for surface curvature effects more realistically. Periodic unit cell idealizations constitute efficient, simple and tractable models which allow clarification of load carrying mechanisms along struts possibly with size effects. However, they fail to reflect some of the crucial morphological and mechanical characteristics of nanoporous metals. On the morphological part, nanoporous metal microstructures are usually formed as a highly disordered and random network of nanosized ligaments. In experiments, their mechanical response is usually observed to be (statistically) isotropic without any preferred directions. On the contrary, the structures depicted in Fig. 44 show cubic anisotropy with high polarity in terms of their directional dependence of Young's modulus.

One way to circumvent this problem is to involve a large number of cells, each with a form of stochastic disorder: cell ligament misalignments by using perturbed junction locations [530], missing ligaments or cells through sequential inhibition or non-uniformly distributed ligament diameters. The crucial role of disorder introduced into ligament networks formed of initially cubic building blocks was reported in [531]. Polygonal-like or polyhedral-like shapes are studied in [532,533] considering statistical distributions.

A more systematic method in forming stochastic (as well as deterministic) cells is through Voronoi tessellation (cf. Section 2.1.1.3). In applications to open-cell structures, cell walls are disregarded and only cell edges are considered. For closed-cell structures, walls are also considered. Random distribution of the previously regular lattice points result in random cell structures. Some noteworthy applications of Voronoi tessellations for generating cellular material microstructures include [534–537]. Based on distance and level set functions, a geometric method for generating open- and closed-cell material microstructures is presented in [538]. The method uses random tessellations constructed from random inclusion packings and allows modeling of disordered foams making use of arbitrary-shaped tessellations. The latter can degenerate in a Voronoi tessellation under special conditions, see Fig. 46 for various closed-cell microstructures formed with this method.

In Gaussian random field approaches, the free-surface of the load bearing phase is defined by level cuts of random fields [4]. In this context, the steps for generating random field-based bicontinuous microstructures are identical to those listed in Section 2.2.3. The only difference here is the substitution of pores for a second solid phase in random bicontinuous composites. The porous microstructures developed by this method are static. Compared to models relying on molecular dynamics simulations of the spinodal decomposition process, leveled wave models prove to be far more efficient by generating such complicated microstructures in relatively short times (few minutes). Besides, usually the mathematical expression defining the random field not only allows a priori definition of the desired phase volume fraction, but also the analytical computation of many topological properties for the generated level cuts, e.g., average Gaussian curvature and the probability distribution for the mean curvature [299,539,296].

Except for the ones relying on Voronoi tessellation, the bicontinuous microstructures considered so far require discretization with three dimensional continuum finite elements. The efficiency level can be increased making use of appropriate beam finite elements. Here, formulations accounting for the shear deformation mode should be considered along with agglomeration of the mass in junctions and associated stiffness increase. It is possible, using the medial axis transformation, to find an equivalent beam network for triply periodic microstructures with level set approximations and the ones generated using random fields, see Fig. 47(c).

²⁷ For fundamental definitions regarding triply periodic minimal surfaces, the reader is referred to Section 2.2.3.

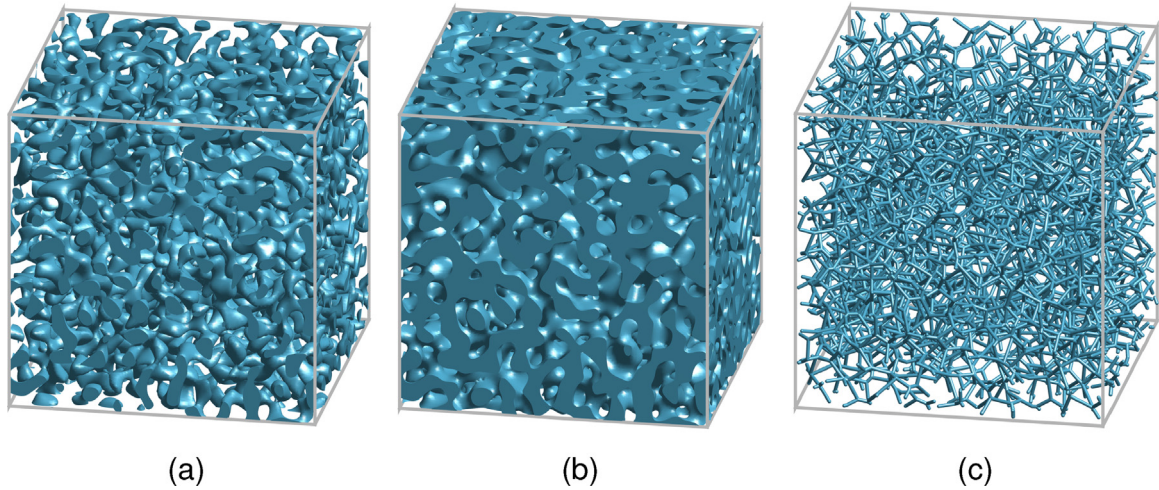


Fig. 47. Open-cell material microstructures developed by leveled-Gaussian random field model with (a) 20% and (b) 50% solid phase volume fraction. RVEs are generated based on the approach of Soyarslan et al. [296]. (c) Homotopic medial axis skeletonization-based beam-FE model for the leveled-Gaussian random field model with 50% solid phase volume fraction [566,567].

3.2.2. Matrix-dilute pore systems

Matrix-dilute pore material systems consist of a matrix material which contains isolated voids. The source of dilute pores can be natural or synthetic. As examples of dilute pore systems one can speak of most metallic alloys with casting defects in the form of micro- or macro-voids of various sizes and shapes. Microvoids nucleate at dislocation pile-ups or through inclusion debonding on the course of mechanical loading whose continuation leads to void growth until void coalescence as a precursor to material failure [540–542]. In this respect, dilute voids in metallic alloys tend to decrease stiffness, strength, and ductility of the material. There are circumstances, however, where dilute pores have a positive influence on certain material characteristics and, thus, are intentionally introduced into the material. Nanoporous metallic glasses are an example for such a positive influence of dilute voids [543] where, e.g., a transition from a catastrophic fracture by localization into a single dominant shear band to a homogeneous plastic flow mediated by a proliferation of shear bands occurs. Another example are architected materials with periodically introduced dilute pores of various shapes and sizes. Dilute pore systems, where the porosity can be as low as 1%, feature large band gaps, that is, frequency ranges with strong wave attenuation, a property which is crucial in vibration control [544].

3.2.2.1. Microstructure reconstruction from experimental data. With their relatively stiffer structure as compared to open-cell foams, dilute pore systems allow conventional serial sectioning methods without any need for polymer infiltration. Those methods are described in Sects. 2.1.1.1 and 2.3.1. Depending on their densities, matrix-dilute pore systems can also be ideal candidates for X-ray microtomography with low overall absorption of the X-rays. With increasing density, the thickness of the samples may need to be limited. Also, the characteristic size of the dilute pores should comply with the resolution

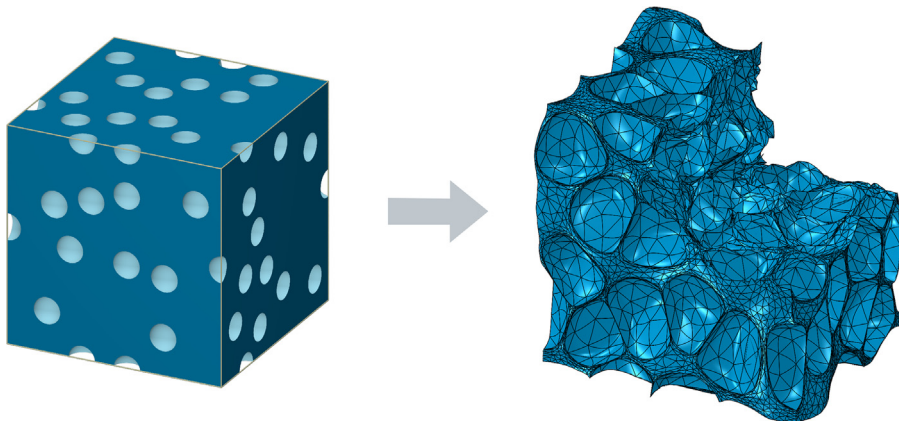


Fig. 48. Excessive and stable void growth in starch containing biopolymers during frying. As a consequence, a substantial relative density reduction is observed where the matrix-dilute pore system evolves into a cellular material with closed-cell structure.

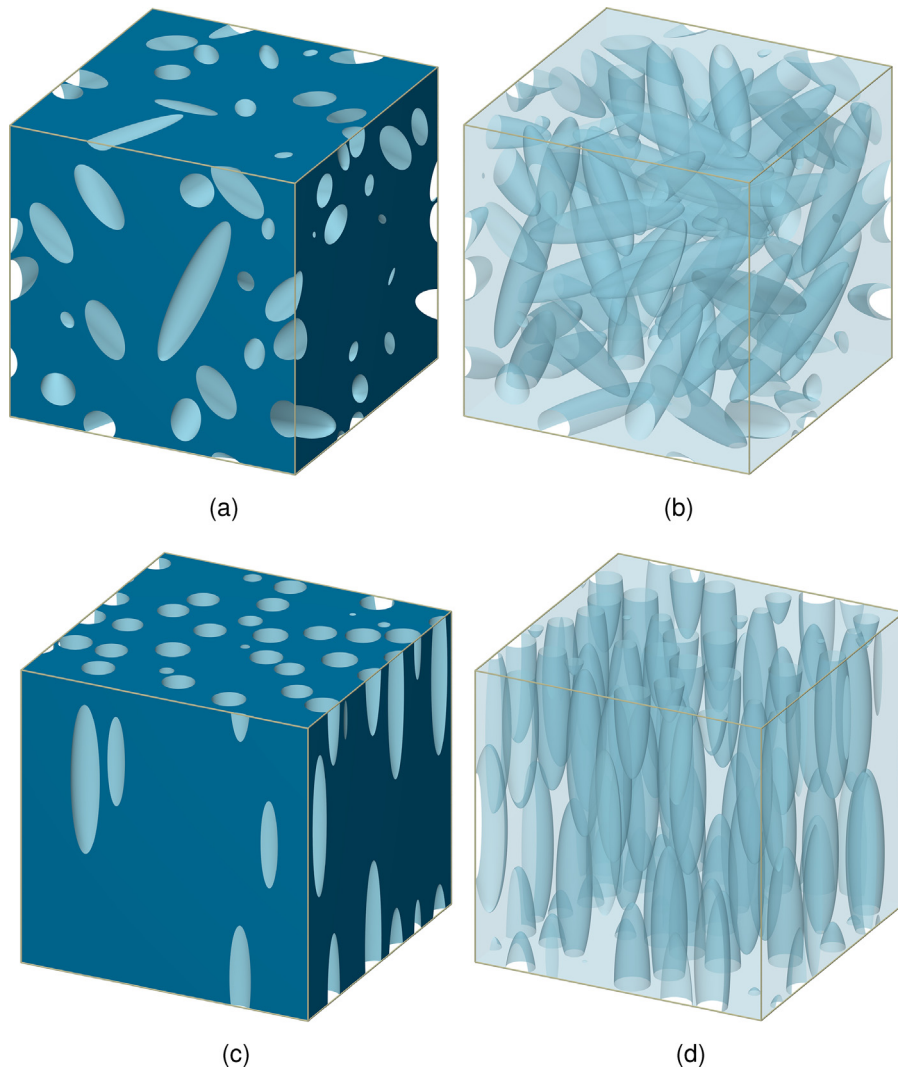


Fig. 49. Typical 3D structures obtained using random sequential additions of overlapping cavities. Microstructure with 50 voids and 80% phase volume fraction generated using (a) randomly orientated elongated ellipsoids incl. (b) its transparent representation for displaying the voids. (c) Deterministically oriented elongated ellipsoids and (d) the transparent representation.

threshold of the utilized X-ray microtomography method. As an example, using in situ X-ray computer tomography, growth and coalescence of embedded arrays of holes, with respective sizes of 10 μm and 40 μm , in pure copper and Glidcop are investigated in [545].

3.2.2.2. Physics based microstructure generation. In matrix-dilute pore systems, pores form during casting or irradiation-induced long-term diffusion and clustering of surviving point defects [546]. Like the case of nanoporous open-cell metallic microstructures, molecular dynamics simulations prove convenient in modeling physical mechanisms of generation and interaction of irradiation defects [547]. Moreover, like in grain growth and recrystallization, the phase field method is frequently used in homogeneous and heterogeneous void and gas bubble evolutions, including gas bubble nucleation and growth [548] and void lattice formation [549]. Moreover, kinetic [550] and object kinetic Monte Carlo methods [551] are among possible modeling techniques for modeling irradiation induced long-time defect evolution, as reviewed in [546].

Under mechanical loading, driven by internal pressurization of pores, and, thus, excessive and stable void growth, matrix-dilute pore systems can evolve into cellular materials with closed-cell microstructures. For instance, during frying starch-containing biopolymers, rapid growth of starch containing voids is observed, see Fig. 48 for simulations of this process. The stability of emerging cell walls even after excessive void growth is due to the strengthening with elongated molecular chains of biopolymer bulk. For metallic materials, void growth only continues up to a critical porosity threshold. Once this threshold is met, the material fails with intervoid linking and rapid void coalescence.

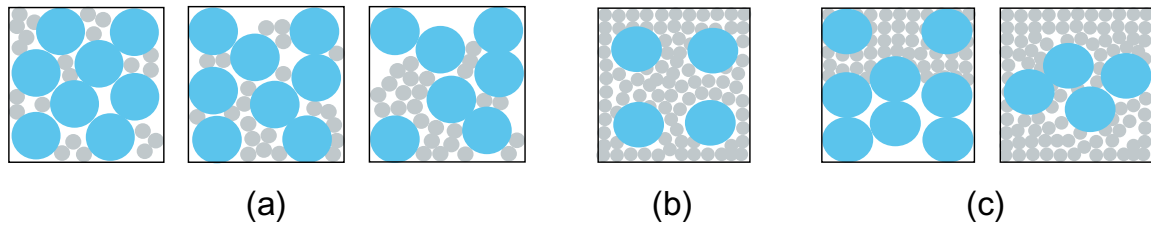


Fig. 50. Microstructure classification of binary granular soils which relies on the granule type dominating the force transmission through contact [555]. Blue: coarse granules. Grey: fine granules. (a) Granular configurations with dominance of coarse granule contact is referred to as coarse grain soil mix. In this scenario, fine granules can be confined within voids fully or partially in contact with coarse granules. They may also act as separators of coarse granules. (b) Stacking of layer(s) of coarse and/or fine granules results in layered soil mix. (c) Granular configurations with dominance of fine granule contact are referred to as fine grain soil mix. Although this scenario considers a binary granule size distribution, in reality, size and shape of the granules can vary drastically. Also, bonding at the contacting interfaces can also be important as observed for bonded expansive geomaterials.

3.2.2.3. Geometrical methods. Since dilute pore systems have a particulate nature, the pores can be modeled by the distribution of non-overlapping cavities. Thus, geometrical methods for RVE generation of this class complies with those listed in Section 2.3.3 on particle reinforced composites. On the other hand, open-cell agglomerates are of nonparticulate nature and, therefore, cannot be modeled as a distribution of overlapping cavities. However, it is possible to generate void structures of a typical foam material by injection of ellipsoid-like voids into a 3D matrix until reaching a desired void volume fraction using random sequential adsorption algorithms [552]. Here, the anisotropy of the final microstructure can be controlled considering the aspect ratio as well as the orientation of the injected ellipsoids, see, e.g., Fig. 49.

3.3. Aggregates

As aggregates, we consider unconsolidated, non-rigid, more-or-less loosely packed assemblages of individual particles where the particles are surrounded by a network of interparticle voids²⁸ whose volume fraction may be as large as 80% [554]. These particles are called granules. Their gathering forms a granular body whose deformation amounts to a granular flow. Aggregates represent a broad category of coarse particulate materials including sand, rice, gravel, crushed stone, slag, recycled concrete and geosynthetic aggregates. Aggregates may be used as reinforcing components in composite materials such as concrete and asphalt concrete (cf. Section 2.3).

Effective properties of granular bodies depend on the size, shape and manner of packing of the granules under frictional contact. The network of the contacting particles forms the load carrying skeleton, and thus, constitutes the fundamental difference of the granular bodies from suspensions [553]. Considering contact mechanisms among granules schematically depicted in Fig. 50, a microstructural classification (according to [555]) of binary granular soils is possible. Here, contacting elements dominating the force transmission are taken as the main criterion considering just two sizes of perfectly circular granules. In reality, size and shape of the granules can vary drastically.

3.3.1. Microstructure reconstruction from experimental data

Since aggregates are unconsolidated loosely packed assemblages, they do not constitute ideal candidates for serial sectioning. However, specimen preparation with infiltration with cross-linked epoxy facilitates cutting and polishing and, thus, microscopic examination by serial sectioning. Application of the method for SEM analysis for Portland cement particles is found in [556]. Like many porous materials, the aggregate's high porosity content is a source of a desired density contrast which makes them ideal for X-ray computer tomography, see, e.g., [557]. This method allows investigation of aggregates with various granule sizes in general in a non-destructive manner as far as sufficient resolution is rendered by the utilized technology (cf. Section 3.2.1.1).

3.3.2. Physics based microstructure generation

Discrete element simulation of the locomotion of aggregates, as in the case of mechanical contraction or drop-and-roll as presented in Section 2.3.2 constitutes the physics simulation based modeling of the emerging microstructures. Since the physics simulation only aims at generating the microstructural layout, cohesive, cataclastic, thermal or rate effects are disregarded and the particles are assumed as rigid with omission of granule deformation. For noteworthy applications of discrete element method in 3D particle discharge and packing under gravitational forces, see, e.g. [558–560].

²⁸ We assume that the interstitial medium between the granules is void. However, granular bodies exist where the interstitial medium is fluid or solid with a weaker strength [553]. Moreover, in reality, the particles may or may not be porous at the scale of interest. This condition may require distinguishing intraparticle and interparticle voids [421].

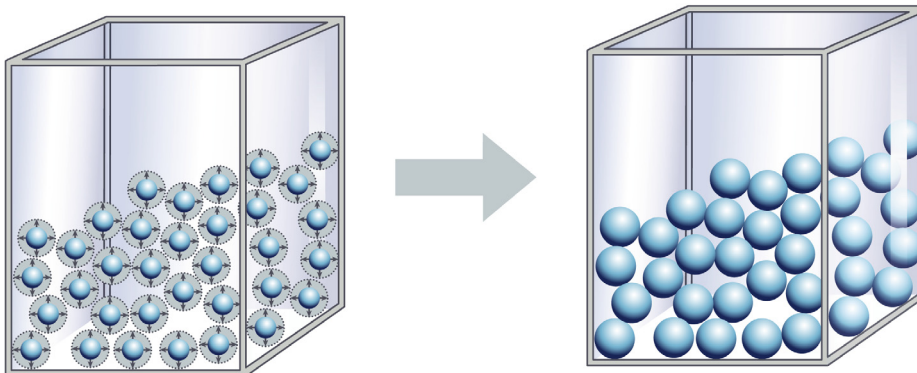


Fig. 51. Demonstration of the mechanism of granular microstructure generation making use of Monte Carlo method.

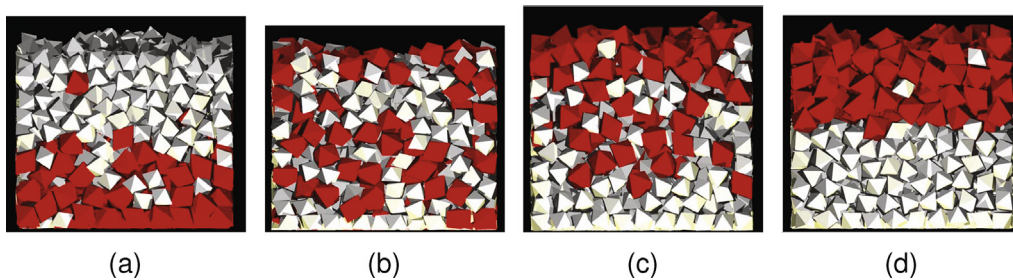


Fig. 52. Final packings of polyhedra with two different sizes, starting with a configuration where the smaller sized polyhedra are positioned on top. After (a) 100 (b) 500 (c) 900, and (d) 1500 shaking iterations. If granular material of different sizes is subjected to shaking or vibration, the larger particles rise to the top and the smaller sink to the ground. Figure reprinted from Granular Matter, A packing algorithm for three-dimensional convex particles [562], 11, 2009, 307–315, Lee et al. (original copyright notice as given in the publication in which the material was originally published). With permission of Springer.

3.3.3. Geometrical methods

Like in the case of physics based methods, geometrical methods for granular distributions follow closely collective rearrangement algorithms which are presented for matrix-inclusion materials in Section 2.3.3. These methods are generally referred to as granular packing algorithms. Thus, a stability check for the generated microstructure is not considered. There have been various attempts in this direction in the literature. In the Monte Carlo spherical packing method, a set of randomly generated spheres are expanded gradually until contact is detected [557]. If possible, the spheres, positions are rearranged to allow further granule growth. This procedure is pursued until the desired void volume fraction is achieved. Fig. 51 depicts a demonstration of the method. Although spherical granules are depicted in this figure, the method can be extended to various polyhedral shapes.

A Monte Carlo approach to generate random packing of spherical particles obeying an a priori defined distribution is presented in He et al. [561]. Overlaps are first allowed, but later eliminated in a relaxation iteration.

An algorithm on packing of convex particles with diverse shapes and sizes in 3D including particle-particle and particle-container wall contact detection is given in [562], see Fig. 52. The authors use a Monte Carlo based approach, consisting of a system generation process, a system packing process, and a system shaking process. Unlike the previously defined method in which packing was due to gradual granule growth, this method delivers packing through sinking of smaller granules towards the bottom of the container with iterative position updating, a step similar to mechanical contraction. Finally, a geometry-based system shaking process takes place to improve the densification.

A statistical approach on how to determine representative volumes of granular materials is published in [563].

4. Summary

Many natural heterogeneous materials are ubiquitous in engineering applications due to their extraordinary mechanical properties featuring seemingly contrasting attributes of light weight and high strength and/or stiffness. With today's manufacturing and processing techniques, it is possible to not only produce synthetic counterparts but also to tailor the emerging microstructures - and, hence, the material's local as well as effective properties, whether it be damage-tolerance, thermal or electrical conductivity, stiffness or hardness, of the material - for intended use. In this respect, in addition to the individual properties of the constituent(s) and their interfaces making up the heterogeneous material, their morphological and

topological features play a substantial role. An accurate quantification of structure-property relationships in natural as well as synthetic materials inevitably requires numerical simulation along with experimental characterization. The need for an RVE, as the smallest volume of the material which allows efficient computation of effective macroscopic properties (such as elastic stiffness, conductivity or permeability) as well as insight into damage and/or fracture behavior, emerges at this stage. In this study, we review RVE generation techniques for heterogeneous solids.

The reference list in this review is by no means exhaustive. Nevertheless, it constitutes a comprehensive collection of relevant up-to-date techniques for generating 3D RVEs for a broad class of materials including polycrystals with grain and lamellar microstructures, matrix-inclusion composites with particle and long fiber reinforcements, woven and non-woven fabrics, cellular materials, matrix dilute pore systems and aggregates. For each microstructure class, methods relying on microstructure reconstruction from experimental data, physics based methods aiming at simulation of physical process(es) liable for microstructure formation and geometrical methods aiming at mimicking the material's morphology disregarding the underlying physics of microstructure development, are considered. These methods are critically reviewed considering their efficiency and accuracy to benefit scientists who are conducting research on microstructured materials and their behavior characterization and prediction.

Acknowledgements

This work benefited from many fruitful discussions with co-workers and colleagues which is gratefully acknowledged. We gratefully acknowledge financial support from the German Research Foundation (DFG) via SFB 986 “M³”, projects A5, B6, and B8. Figure courtesies:

Fig. 1(a): J. K. Wilmers, Fig. 2, top row, from left to right: J. Enz (Helmholtz-Zentrum Geesthacht), M. Rackel (Helmholtz-Zentrum Geesthacht), Figure reprinted from [286] under the terms of the Creative Commons Attribution 3.0 licence. <http://creativecommons.org/licenses/by/3.0> reprinted from [300] with permission from Wiley-VCH Verlag GmbH & Co. KGaA, L. Wang (Central Division of Electron Microscopy, Hamburg University of Technology), reprinted from [564] with permission (Atwater et al. [564] published under license CC BY 4.0 <https://creativecommons.org/licenses/by/4.0>), N. Mameka (Helmholtz-Zentrum Geesthacht), own work, reprinted from [565] with permission (Liberato et al. [565] published under license CC BY-NY 3.0 <https://creativecommons.org/licenses/by-nc/3.0>), own work.

Fig. 2, bottom row, from left to right: all own works. Fig. 3(a): J. Schmauch and Ch. Braun (Universität des Saarlandes, FR 7.2 Experimentalphysik), Fig. 12: M. Rackel (Helmholtz-Zentrum Geesthacht), Fig. 18(b): L. Wang (Central Division of Electron Microscopy, Hamburg University of Technology), Fig. 18(c): M. Mecklenburg, SFB 986 “M³”, project B1 (Hamburg University of Technology), Fig. 22(b): S. Bechtle, SFB 986 “M³”, project A6 (Hamburg University of Technology), Fig. 38(a): N. Mameka (Helmholtz-Zentrum Geesthacht).

We further acknowledge help in preparation of the following figures: Fig. 1(b): M. Bremer (University of Wuppertal), Figs. 22(a), 23 and 43: V. Blümer (University of Wuppertal), Figs. 22(c): Ch. Leuther (University of Wuppertal), Fig. 28: S. Drücker (Hamburg University of Technology), Figs. 31, 32, 34, 35, 36, 39, 40: N. Jendrysik (Hamburg University of Technology). The specimen shown in Fig. 3(b) resides at Natural History Museum of Utah.

References

- [1] Altenbach H, Altenbach J, Kissing W. *Mechanics of composite structural elements*. Berlin Heidelberg: Springer-Verlag; 2004.
- [2] Aboudi J, Arnold S, Bednarczyk B. *Micromechanics of composite materials: a generalized multiscale analysis approach*. 1st ed. Academic Press; 2013.
- [3] Zaoui A. Continuum micromechanics: survey. *J Eng Mech* 2002;128(8):808–16.
- [4] Torquato S. *Random heterogeneous materials: microstructure and macroscopic properties*, vol. 16. New York: Springer; 2002.
- [5] Ostoja-Starzewski M. Material spatial randomness: from statistical to representative volume element. *Probab Eng Mech* 2006;21(2):112–32.
- [6] Hill R. Elastic properties of reinforced solids: some theoretical principles. *J Mech Phys Solids* 1963;11(5):357–72.
- [7] Drugan WJ, Willis JR. A micromechanics-based nonlocal constitutive equation and estimates of representative volume element size for elastic composites. *J Mech Phys Solids* 1996;44(4):497–524.
- [8] Gusev AA. Representative volume element size for elastic composites: a numerical study. *J Mech Phys Solids* 1997;45(9):1449–59.
- [9] Shan Z, Gokhale AM. Representative volume element for non-uniform micro-structure. *Comput Mater Sci* 2002;24(3):361–79.
- [10] Jiang M, Alzabdeh K, Jasiuk I, Ostoja-Starzewski M. Scale and boundary conditions effects in elastic properties of random composites. *Acta Mech* 2001;148(1):63–78.
- [11] Kanit T, Forest S, Galliet I, Mounoury V, Jeulin D. Determination of the size of the representative volume element for random composites: statistical and numerical approach. *Int J Solids Struct* 2003;40(13):3647–79.
- [12] Dirrenberger J, Forest S, Jeulin D. Towards gigantic RVE sizes for 3D stochastic fibrous networks. *Int J Solids Struct* 2014;51(2):359–76.
- [13] Harper LT, Qian C, Turner TA, Li S, Warrior NA. Representative volume elements for discontinuous carbon fibre composites - part 2: determining the critical size. *Compos Sci Technol* 2012;72(2):204–10.
- [14] Trias D, Costa J, Turon A, Hurtado JE. Determination of the critical size of a statistical representative volume element (SRVE) for carbon reinforced polymers. *Acta Mater* 2006;54(13):3471–84.
- [15] Gitman IM, Askes H, Sluys LJ. Representative volume: existence and size determination. *Eng Fract Mech* 2007;74(16):2518–34.
- [16] Hoang T, Guerich M, Yvonnet J. Determining the size of RVE for nonlinear random composites in an incremental computational homogenization framework. *J Eng Mech* 2016;142(5):04016018.
- [17] Khisaeva ZF, Ostoja-Starzewski M. On the size of RVE in finite elasticity of random composites. *J Elast* 2006;85(2):153.
- [18] Ren Z-Y, Zheng Q-S. Effects of grain sizes, shapes, and distribution on minimum sizes of representative volume elements of cubic polycrystals. *Mech Mater* 2004;36(12):1217–29.
- [19] Shen H, Brinson LC. A numerical investigation of the effect of boundary conditions and representative volume element size for porous titanium. *J Mech Mater Struct* 2006;1(7):1179–204.
- [20] Huet C. Coupled size and boundary-condition effects in viscoelastic heterogeneous and composite bodies. *Mech Mater* 1999;31(12):787–829.

- [21] Böhm HJ. A short introduction to continuum micromechanics. Vienna: Springer; 2004. p. 1–40.
- [22] Zohdi TI, Wriggers P. Fundamental micro–macro concepts. Berlin, Heidelberg: Springer Berlin Heidelberg; 2005. p. 45–62.
- [23] Mura T. Micromechanics of defects in solids. Kluwer Academic Publishers; 1993.
- [24] Nemat-Nasser S, Hori M. Micromechanics: overall properties of heterogeneous solids. Amsterdam: Elsevier; 1999.
- [25] Dvorak GJ. Micromechanics of composite materials. Solid mechanics and its applications, vol. 186. Springer; 2013.
- [26] Doghri I. Micro-mechanics of materials. Berlin, Heidelberg: Springer Berlin Heidelberg; 2000. p. 519–44.
- [27] McBride A, Mergheim J, Javili A, Steinmann P, Bargmann S. Micro-to-macro transitions for heterogeneous material layers accounting for in-plane stretch. *J Mech Phys Solids* 2012;60(6):1221–39.
- [28] Kanouté P, Boso DP, Chaboche JL, Schrefler BA. Multiscale methods for composites: a review. *Arch Comput Meth Eng* 2009;16(1):31–75.
- [29] Galvanetto U, Aliabadi M. Multiscale modeling in solid mechanics: computational approaches (computational and experimental methods in structures). Computational and experimental methods in structures, vol. 3. Imperial College Press; 2009.
- [30] Charalambakis N. Homogenization techniques and micromechanics. A survey and perspectives. *Appl Mech Rev* 2010;63(3):030803.
- [31] Nguyen V, Stroeve M, Sluys L. Multiscale continuous and discontinuous modeling of heterogeneous materials: a review on recent developments. *J Multisc Model* 2011;3(4):229–70.
- [32] Klusemann B, Böhm H, Svendsen B. Homogenization methods for multi-phase elastic composites with non-elliptical reinforcements: comparisons and benchmarks. *Euro J Mech A/Solids* 2012;34:21–37.
- [33] Ortolano J, Ortega JH, Olivella XO. A comparative study on homogenization strategies for multi-scale analysis of materials. Centre Internacional de Mètodes Numèrics en Enginyeria (CIMNE); 2013.
- [34] Saeb S, Steinmann P, Javili A. Aspects of computational homogenization at finite deformations: a unifying review from Reuss' to Voigt's bound. *Appl Mech Rev* 2016;68(5):050801.
- [35] Eshelby J. The determination of the elastic field of an ellipsoidal inclusion, and related problems. *Proc R Soc Lond A: Math, Phys Eng Sci* 1957;241(1226):376–96. <https://doi.org/10.1098/rspa.1957.0133>.
- [36] Mori T, Tanaka K. Average stress in matrix and average elastic energy of materials with misfitting inclusions. *Acta Metal* 1973;21(5):571–4. [https://doi.org/10.1016/0001-6160\(73\)90064-3](https://doi.org/10.1016/0001-6160(73)90064-3).
- [37] Benveniste Y. A new approach to the application of Mori-Tanaka's theory in composite materials. *Mech Mater* 1987;6(2):147–57. [https://doi.org/10.1016/0167-6636\(87\)90005-6](https://doi.org/10.1016/0167-6636(87)90005-6).
- [38] Hershey A. The elasticity of an isotropic aggregate of anisotropic cubic crystals. *J Appl Mech-Trans ASME* 1954;21(3):236–40.
- [39] Kröner E. Berechnung der elastischen Konstanten des Vielkristalls aus den Konstanten des Einkristalls. *Zeitschrift für Physik* 1958;151(4):504–18.
- [40] Hill R. A self-consistent mechanics of composite materials. *J Mech Phys Solids* 1965;13(4):213–22.
- [41] Budiansky B. On the elastic moduli of some heterogeneous materials. *J Mech Phys Solids* 1965;13(4):223–7.
- [42] Lebensohn R, Tom C. A self-consistent anisotropic approach for the simulation of plastic deformation and texture development of polycrystals: application to zirconium alloys. *Acta Metal Mater* 1993;41(9):2611–24. [https://doi.org/10.1016/0956-7151\(93\)90130-K](https://doi.org/10.1016/0956-7151(93)90130-K).
- [43] Molinari A, Canova G, Ahzi S. A self consistent approach of the large deformation polycrystal viscoplasticity. *Acta Metal* 1987;35(12):2983–94. [https://doi.org/10.1016/0001-6160\(87\)90297-5](https://doi.org/10.1016/0001-6160(87)90297-5).
- [44] Sharma P, Ganti S. Size-dependent Eshelbys tensor for embedded nano-inclusions incorporating surface/interface energies. *ASME J Appl Mech* 2004;71(5):663–71.
- [45] Nemat-Nasser S, Taya M. On effective moduli of an elastic body containing periodically distributed voids. *Quart J App Math* 1981;39:43–59.
- [46] Dormieux L, Molinari A, Kondo D. Micromechanical approach to the behavior of poroelastic materials. *J Mech Phys Solids* 2002;50(10):2203–31. [https://doi.org/10.1016/S0022-5096\(02\)00008-X](https://doi.org/10.1016/S0022-5096(02)00008-X).
- [47] Nazarenko L, Bargmann S, Stolarski H. Energy-equivalent inhomogeneity approach to analysis of effective properties of nanomaterials with stochastic structure. *Int J Solids Struct* 2015;59:183–97. <https://doi.org/10.1016/j.ijsolstr.2015.01.026>.
- [48] Hashin Z. Assessment of the self consistent scheme approximation: conductivity of particulate composites. *J Compos Mater* 1968;2(3):284–300.
- [49] Garboczi E, Berryman J. Elastic moduli of a material containing composite inclusions: effective medium theory and finite element computations. *Mech Mater* 2001;33(8):455–70. [https://doi.org/10.1016/S0167-6636\(01\)00067-9](https://doi.org/10.1016/S0167-6636(01)00067-9).
- [50] Bernard O, Ulm F-J, Lemarchand E. A multiscale micromechanics-hydration model for the early-age elastic properties of cement-based materials. *Cem Concr Res* 2003;33(9):1293–309. [https://doi.org/10.1016/S0008-8846\(03\)00039-5](https://doi.org/10.1016/S0008-8846(03)00039-5).
- [51] Pichler B, Hellmich C. Upscaling quasi-brittle strength of cement paste and mortar: a multi-scale engineering mechanics model. *Cem Concr Res* 2011;41(5):467–76.
- [52] Duschlbauer D, Böhm H, Pettermann H. Computational simulation of composites reinforced by planar random fibers: homogenization and localization by unit cell and mean field approaches. *J Compos Mater* 2006;40(24):2217–34.
- [53] Chou T-W, Nomura S, Taya M. A self-consistent approach to the elastic stiffness of short-fiber composites. *J Compos Mater* 1980;14(3):178–88.
- [54] Pipes RB, Frankland S, Hubert P, Saether E. Self-consistent properties of carbon nanotubes and hexagonal arrays as composite reinforcements. *Compos Sci Technol* 2003;63(10):1349–58.
- [55] Feng X-Q, Mai Y-W, Qin Q-H. A micromechanical model for interpenetrating multiphase composites. *Comput Mater Sci* 2003;28(3):486–93.
- [56] Hellmich C, Barthlmy J-F, Dormieux L. Mineral collagen interactions in elasticity of bone ultrastructure a continuum micromechanics approach. *Euro J Mech - A/Solids* 2004;23(5):783–810. <https://doi.org/10.1016/j.euromechsol.2004.05.004>.
- [57] Nazarenko L, Bargmann S, Stolarski H. Influence of interfaces on effective properties of nanomaterials with stochastically distributed spherical inclusions. *Int J Solids Struct* 2014;51(5):954–66. <https://doi.org/10.1016/j.ijsolstr.2013.11.024>.
- [58] Shahidi M, Pichler B, Hellmich C. Interfacial micromechanics assessment of classical rheological models. II: multiple interface sizes and viscosities. *J Eng Mech* 2016;142(3):04015093.
- [59] Moulinec H, Suquet P. A fast numerical method for computing the linear and nonlinear mechanical properties of composites. *Comptes rendus de l'Académie des sciences. Série II, Mécanique, physique, chimie, astronomie* 1994;318(11):1417–23.
- [60] Brisard S, Dormieux L. FFT-based methods for the mechanics of composites: a general variational framework. *Comput Mater Sci* 2010;49(3):663–71. <https://doi.org/10.1016/j.commatsci.2010.06.009>.
- [61] Torquato S. Statistical description of microstructures. *Ann Rev Mater Res* 2002;32(1):77–111.
- [62] Torquato S. Morphology and effective properties of disordered heterogeneous media. *Int J Solids Struct* 1998;35(19):2385–406.
- [63] Voigt W. Lehrbuch der Kristallphysik: mit Ausschluss der Kristalloptik. Leipzig Berlin: B.G. Teubner; 1928.
- [64] Reuss A. Berechnung der Fließgrenze von Mischkristallen auf Grund der Plastizitätsbedingung für Einkristalle. *ZAMM - J Appl Math Mech/Zeitschrift für Angewandte Mathematik und Mechanik* 1929;9(1):49–58.
- [65] Hashin Z, Shtrikman S. A variational approach to the theory of the elastic behaviour of multiphase materials. *J Mech Phys Solids* 1963;11(2):127–40.
- [66] Beran MJ, Molyneux J. Use of classical variational principles to determine bounds for the effective bulk modulus in heterogeneous media. *Quart Appl Math* 1966;24:107–18.
- [67] Milton GW. Bounds on the electromagnetic, elastic, and other properties of two-component composites. *Phys Rev Lett* 1981;46:542–5.
- [68] Milton GW, Phan-Thien N. New bounds on effective elastic moduli of two-component materials. *Proc R Soc Lond Ser A, Math Phys Sci* 1982;380(1779):305–31.
- [69] Talbot D, Willis J. Some simple explicit bounds for the overall behaviour of nonlinear composites. *Int J Solids Struct* 1992;29(14):1981–7. [https://doi.org/10.1016/0020-7683\(92\)90188-Y](https://doi.org/10.1016/0020-7683(92)90188-Y).
- [70] Ponte Castañeda P. The effective mechanical properties of nonlinear isotropic composites. *J Mech Phys Solids* 1991;39(1):45–71.

- [71] Klusemann B, Svendsen B, Vehoff H. Modeling and simulation of deformation behavior, orientation gradient development and heterogeneous hardening in thin sheets with coarse texture. *Int J Plast* 2013;50:109–26.
- [72] Sachtleber M, Zhao Z, Raabe D. Experimental investigation of plastic grain interaction. *Mater Sci Eng: A* 2002;336(1–2):81–7.
- [73] DeHoff R, Aigeltinger E, Craig K. Experimental determination of the topological properties of three-dimensional microstructures. *J Microsc* 1972;95(1):69–91.
- [74] Rhines F, Craig K, DeHoff R. Mechanism of steady-state grain growth in aluminum. *Metall Trans* 1974;5(2):413–25.
- [75] Weiland H, Rouns TN, Liu J. The role of particle stimulated nucleation during recrystallization of an aluminum-manganese alloy. *Zeitschrift für Metallkunde* 1994;85(8):592–7.
- [76] Liu G, Yu H. On the sampling of serial sectioning technique for three dimensional space-filling grain structures. *Image Anal Stereol* 2000;19(2):81–4.
- [77] Liu G, Yu H, Qin X. Three-dimensional grain topology–size relationships in a real metallic polycrystal compared with theoretical models. *Mater Sci Eng: A* 2002;326(2):276–81.
- [78] Spowart JE, Mullens HE, Puchala BT. Collecting and analyzing microstructures in three dimensions: a fully automated approach. *Jom* 2003;55(10):35–7.
- [79] Raya SP, Udupa JK. Shape-based interpolation of multidimensional objects. *IEEE Trans Med Imag* 1990;9(1):32–42.
- [80] Lyroudia K, Nikolaidis N, Pitas I, Zervas P, Palakidis K. Computerized three-dimensional reconstruction: a method to study pulpal vessels and nerves. *J Endodont* 1993;19(12):604–8.
- [81] Kubis AJ, Shiflet GJ, Hull R, Dunn DN. Focused ion-beam tomography. *Metall Mater Trans A* 2004;35(7):1935–43.
- [82] Herman GT, Zheng J, Bucholtz CA. Shape-based interpolation. *IEEE Comput Graph Appl* 1992;12(3):69–79.
- [83] Grevera GJ, Udupa JK. An objective comparison of 3-d image interpolation methods. *IEEE Trans Med Imag* 1998;17(4):642–52.
- [84] Bors AG, Kechagias L, Pitas I. Binary morphological shape-based interpolation applied to 3-d tooth reconstruction. *IEEE Trans Med Imag* 2002;21(2):100–8.
- [85] Münch B, Gasser P, Holzer L, Flatt R. FIB-nanotomography of particulate systems Part II: particle recognition and effect of boundary truncation. *J Am Ceram Soc* 2006;89(8):2586–95.
- [86] Jørgensen P, Hansen K, Larsen R, Bowen J. A framework for automatic segmentation in three dimensions of microstructural tomography data. *Ultramicroscopy* 2010;110(3):216–28.
- [87] Simmons JP, Chuang P, Comer M, Spowart JE, Uchic MD, Graef MD. Application and further development of advanced image processing algorithms for automated analysis of serial section image data. *Model Simul Mater Sci Eng* 2009;17(2):025002.
- [88] Madej L, Mojzeszko M, Chraponski J. Digital material representation model of porous microstructure based on 3d reconstruction algorithm. *Arch Metal Mater* 2017;62(2):563–9.
- [89] Fredrich JT. 3D imaging of porous media using laser scanning electron microscopy with application to microscale transport processes. *Phys Chem Earth, Part A: Solid Earth Geodesy* 1999;24(7):551–61.
- [90] Forsman O. Undersökning av rymdstrukturen hos ett kolstå av hypereutectoid sammansättning. *Jernkontorets Ann* 1918;102:1–30.
- [91] Chawla N, Ganesh VV, Wunsch B. Three-dimensional (3D) microstructure visualization and finite element modeling of the mechanical behavior of SiC particle reinforced aluminum composites. *Scripta Mater* 2004;51(2):161–5.
- [92] Wiederkehr T, Klusemann B, Gies D, Müller H, Svendsen B. An image morphing method for 3D reconstruction and FE-analysis of pore networks in thermal spray coatings. *Comput Mater Sci* 2010;47(4):881–9.
- [93] Bansal RK, Kubis A, Hull R, Fitz-Gerald JM. High-resolution three-dimensional reconstruction: a combined scanning electron microscope and focused ion-beam approach. *J Vac Sci Technol B* 2006;24(2):554–61.
- [94] Groeber MA, Haley BK, Uchic MD, Dimiduk DM, Ghosh S. 3D reconstruction and characterization of polycrystalline microstructures using a FIB-SEM system. *Mater Character* 2006;57(4):259–73.
- [95] Zaefferer S, Wright SI, Raabe D. Three-dimensional orientation microscopy in a focused ion beam-scanning electron microscope: a new dimension of microstructure characterization. *Metall Mater Trans A* 2008;39(2):374–89.
- [96] Korte S, Ritter M, Jiao C, Midgley PA, Clegg WJ. Three-dimensional electron backscattered diffraction analysis of deformation in MgO micropillars. *Acta Mater* 2011;59(19):7241–54.
- [97] Holzer L, Cantoni M. Review of FIB-tomography. In: *Nanofabrication using focused ion and electron beams: principles and applications*. Oxford University Press; 2012. p. 410–35.
- [98] Mangipudi K, Radisch V, Holzer L, Volkert C. A FIB-nanotomography method for accurate 3D reconstruction of open nanoporous structures. *Ultramicroscopy* 2016;163:38–47.
- [99] Jones HG, Mingard KP, Cox DC. Investigation of slice thickness and shape milled by a focused ion beam for three-dimensional reconstruction of microstructures. *Ultramicroscopy* 2014;139:20–8.
- [100] Hu K, Ziehmer M, Wang K, Lilleodden ET. Nanoporous gold: 3D structural analyses of representative volumes and their implications on scaling relations of mechanical behaviour. *Philos Magaz* 2016;96(32–34):3322–35.
- [101] Adams B, Olson T. The mesostructure – properties linkage in polycrystals. *Prog Mater Sci* 1998;43(1):1–87.
- [102] Larson BC, Yang W, Ice GE, Budai JD, Tischler JZ. Three-dimensional X-ray structural microscopy with submicrometre resolution. *Nature* 2002;415(6874):887–90.
- [103] Groeber M, Ghosh S, Uchic MD, Dimiduk DM. A framework for automated analysis and simulation of 3D polycrystalline microstructures.: Part 1: statistical characterization. *Acta Mater* 2008;56(6):1257–73.
- [104] Groeber M, Ghosh S, Uchic MD, Dimiduk DM. A framework for automated analysis and simulation of 3D polycrystalline microstructures. Part 2: synthetic structure generation. *Acta Mater* 2008;56(6):1274–87.
- [105] Diehl M, Groeber M, Haase C, Molodov DA, Roters F, Raabe D. Identifying structure–property relationships through DREAM.3D representative volume elements and DAMASK crystal plasticity simulations: an integrated computational materials engineering approach. *JOM* 2017;1–8.
- [106] Adams B. Description of the intercrystalline structure distribution in polycrystalline materials. *Metall Trans A* 1986;17(12):2199–207.
- [107] Saylor DM, Rohrer GS. Determining crystal habits from observations of planar sections. *J Am Ceram Soc* 2002;85(11):2799–804.
- [108] Zhang C, Enomoto M, Suzuki A, Ishimaru T. Characterization of three-dimensional grain structure in polycrystalline iron by serial sectioning. *Metall Mater Trans A* 2004;35(7):1927–33.
- [109] Brahme A, Alvi M, Saylor D, Fridy J, Rollett A. 3D reconstruction of microstructure in a commercial purity aluminum. *Scripta Mater* 2006;55(1):75–80.
- [110] Kelly T, Miller M. Atom probe tomography. *Rev Scient Instrum* 2007;78(3):031101.
- [111] Katnagallu S, Nematollahi A, Dagan M, Moody M, Grabowski B, Gault B, et al. High fidelity reconstruction of experimental field ion microscopy data by atomic relaxation simulations. *Microsc Microanal* 2017;23(Suppl 1):642–3.
- [112] Miao J, Ishikawa T, Johnson B, Anderson EH, Lai B, Hodgson KO. High resolution 3D X-ray diffraction microscopy. *Phys Rev Lett* 2002;89(8):088303.
- [113] Ludwig W, King A, Reischig P, Herbig M, Lauridsen E, Schmidt S, et al. New opportunities for 3D materials science of polycrystalline materials at the micrometre lengthscale by combined use of X-ray diffraction and X-ray imaging. *Mater Sci Eng: A* 2009;524(1):69–76.
- [114] Chen Y-CK, Chu Y, Yi J, McNulty I, Shen Q, Voorhees P, et al. Morphological and topological analysis of coarsened nanoporous gold by X-ray nanotomography. *Appl Phys Lett* 2010;96(4):043122.
- [115] Döbrich K, Rau C, Krill C. Quantitative characterization of the three-dimensional microstructure of polycrystalline Al-Sn using X-ray microtomography. *Metall Mater Trans A* 2004;35(7):1953–61.
- [116] Döbrich K. Tomographische Charakterisierung und quantitative Bestimmung der Korngrößenkorrelation in polykristallinem Al-Sn. Diploma Thesis, Saarland University, Saarbrücken, Germany; 2002.
- [117] Midgley PA, Dunin-Borkowski RE. Electron tomography and holography in materials science. *Nat Mater* 2009;8(4):271–80.

- [118] Maire E, Buffière J-Y, Salvo L, Blandin J, Ludwig W, Létang J. On the application of X-ray microtomography in the field of materials science. *Adv Eng Mater* 2001;3(8):539–46.
- [119] Ferrière E, Buffière J-Y, Ludwig W, Gravouil A, Edwards L. Fatigue crack propagation: in situ visualization using X-ray microtomography and 3D simulation using the extended finite element. *Acta Mater* 2006;54(4):1111–22.
- [120] Salvo L, Suéry M, Marmottant A, Limodin N, Bernard D. 3D imaging in material science: application of X-ray tomography. *Comp Rend Phys* 2010;11(9–10):641–9. <https://doi.org/10.1016/j.crhy.2010.12.003>.
- [121] Renversade L, Quey R, Ludwig W, Menasche D, Maddali S, Suter RM, et al. Comparison between diffraction contrast tomography and high-energy diffraction microscopy on a slightly deformed aluminium alloy. *IUCrj* 2016;3(1):32–42.
- [122] Yang W, Larson B, Tischler J, Ice G, Budai J, Liu W. Differential-aperture X-ray structural microscopy: a submicron-resolution three-dimensional probe of local microstructure and strain. *Micron* 2004;35(6):431–9.
- [123] Zhang C, Li H, Eisenlohr P, Liu W, Boehlert C, Crimp M, et al. Effect of realistic 3D microstructure in crystal plasticity finite element analysis of polycrystalline Ti-5Al-2.5Sn. *Int J Plast* 2015;69:21–35.
- [124] Eisenlohr P, Shanthraj P, Kieft BV, Bieler T, Liu W, Xu R. Subsurface grain morphology reconstruction by differential aperture X-ray microscopy. *JOM* 2017:1–6.
- [125] Poulsen HF, Nielsen SF, Lauridsen EM, Schmidt S, Suter RM, Lienert U, et al. Three-dimensional maps of grain boundaries and the stress state of individual grains in polycrystals and powders. *J Appl Crystal* 2001;34(6):751–6.
- [126] Pokharel R, Lind J, Li S, Kenesei P, Lebensohn R, Suter R, et al. In-situ observation of bulk 3D grain evolution during plastic deformation in polycrystalline Cu. *Int J Plast* 2015;67:217–34.
- [127] Lauridsen E, Schmidt S, Nielsen S, Margulies L, Poulsen H, Juul Jensen D. Non-destructive characterization of recrystallization kinetics using three-dimensional X-ray diffraction microscopy. *Scripta Mater* 2006;55:51–6.
- [128] Miao J, Sandberg R, Song C. Coherent X-ray diffraction imaging. *IEEE J Select Top Quant Electron* 2012;18(1):399–410. <https://doi.org/10.1109/jstqe.2011.2157306>.
- [129] Pfeifer M, Williams G, Vartanyants I, Harder R, Robinson I. Three-dimensional mapping of a deformation field inside a nanocrystal. *Nature* 2006;442(7098):63–6.
- [130] Vaxelaire N, Proudhon H, Labat S, Kirchlechner C, Keckes J, Jacques V, et al. Methodology for studying strain inhomogeneities in polycrystalline thin films during in situ thermal loading using coherent X-ray diffraction. *New J Phys* 2010;12(3):035018. <https://doi.org/10.1088/1367-2630/12/3/035018>.
- [131] Chen-Wiegart YK, Harder R, Dunand D, McNulty I. Evolution of dealloying induced strain in nanoporous gold crystals. *Nanoscale*; 2017.
- [132] Reid AC, Langer SA, Lua RC, Coffman VR, Haan S-I, Garca RE. Image-based finite element mesh construction for material microstructures. *Comput Mater Sci* 2008;43(4):989–99.
- [133] Coffman V, Reid A, Langer S, Dogan G. OOF3D: an image-based finite element solver for materials science. *Math Comp Simul* 2012;82(12):2951–61.
- [134] Yuan Z, Fish J. Toward realization of computational homogenization in practice. *Int J Numer Meth Eng* 2008;73(3):361–80.
- [135] Kassem G. Micromechanical material models for polymer composites through advanced numerical simulation techniques, Ph.D. Dissertation. RWTH Aachen (Germany); 2010.
- [136] Schneider K, Klusemann B, Bargmann S. Fully periodic RVEs for technological relevant composites: not worth the effort! *J Mech Mater Struct* 2017;12:471–84.
- [137] Kawasaki K, Nagai T, Nakashima K. Vertex models for two-dimensional grain growth. *Philos Magaz B* 1989;60(3):399–421.
- [138] Fuchizaki K, Kusaba T, Kawasaki K. Computer modelling of three-dimensional cellular pattern growth. *Philos Magaz B* 1995;71(3):333–57.
- [139] Weygand D, Bréchet Y, Lépinoux J, Gust W. Three-dimensional grain growth: a vertex dynamics simulation. *Philos Magaz B* 1999;79(5):703–16.
- [140] Syha M, Weygand D. A generalized vertex dynamics model for grain growth in three dimensions. *Model Simul Mater Sci Eng* 2009;18(1):015010.
- [141] Mora LB, Mohles V, Shvindlerman L, Gottstein G. Effect of a finite quadruple junction mobility on grain microstructure evolution: theory and simulation. *Acta Mater* 2008;56(5):1151–64.
- [142] Mora LB, Gottstein G, Shvindlerman L. Three-dimensional grain growth: analytical approaches and computer simulations. *Acta Mater* 2008;56(20):5915–26.
- [143] Brakke K. The surface evolver. *Exper Math* 1992;1(2):141–65.
- [144] Wakai F, Enomoto N, Ogawa H. Three-dimensional microstructural evolution in ideal grain growth – general statistics. *Acta Mater* 2000;48(6):1297–311.
- [145] Janssens K. An introductory review of cellular automata modeling of moving grain boundaries in polycrystalline materials. *Math Comp Simul* 2010;80:1361–81.
- [146] Miodownik M. A review of microstructural computer models used to simulate grain growth and recrystallisation in aluminium alloys. *J Light Metals* 2002;2:125–35.
- [147] Raabe D. Cellular automata in materials science with particular reference to recrystallization simulation. *Ann Rev Mater Res* 2002;32:53–76.
- [148] Janssens K. Random grid, three-dimensional, space-time coupled cellular automata for the simulation of recrystallization and grain growth. *Model Simul Mater Sci Eng* 2003;11:157–71.
- [149] Yazdipour N, Davies C, Hodgson P. Microstructural modeling of dynamic recrystallization using irregular cellular automata. *Comput Mater Sci* 2008;44:566–76.
- [150] Raabe D. Introduction of a scalable three-dimensional cellular automaton with a probabilistic switching rule for the discrete mesoscale simulation of recrystallization phenomena. *Philos Magaz A* 1999;79(10):2339–58.
- [151] Brown S, Bruce N. Three-dimensional cellular automaton models of microstructural evolution during solidification. *J Mater Sci* 1995;30:1144–50.
- [152] Cortie M. Simulation of metal solidification using a cellular automaton. *Metall Trans B* 1993;24B:1045–53.
- [153] Pavlyk V, Dilthey U. Simulation of weld solidification microstructure and its coupling to the macroscopic heat and fluid flow modelling. *Model Simul Mater Sci Eng* 2004;12:33–45.
- [154] Rappaz M, Gandin C-A. Probabilistic modelling of microstructure formation in solidification processes. *Acta Metal Mater* 1993;41(2):345–60.
- [155] Spittle J, Brown S. A cellular automaton model of steady-state columnar-dendritic growth in binary alloys. *J Mater Sci* 1995;30:3989–94.
- [156] Wang W, Lee D, McLean M. A model of solidification microstructures in nickel-based superalloys: predicting primary dendrite spacing selection. *Acta Mater* 2003;51:2971–87.
- [157] Zhu M, Hong C. A three dimensional modified cellular automaton model for the prediction of solidification microstructures. *ISIJ Int* 2002;42(5):520–6.
- [158] Bos C, Mecozzi M, Sietsma J. A microstructure model for recrystallisation and phase transformation during the dual-phase steel annealing cycle. *Comput Mater Sci* 2010;48:692–9.
- [159] Ding R, Guo Z. Microstructural modelling of dynamic recrystallisation using an extended cellular automaton approach. *Comput Mater Sci* 2002;23:209–18.
- [160] Hallberg H, Wallin M, Ristinmaa M. Simulation of discontinuous dynamic recrystallization in pure Cu using a probabilistic cellular automaton. *Comput Mater Sci* 2010;49:25–34.
- [161] Hesselbarth H, Göbel I. Simulation of recrystallization by cellular automata. *Acta Metal Mater* 1991;39(9):2135–43.
- [162] Kühbach M, Gottstein G, Barrales-Mora L. A statistical ensemble cellular automaton microstructure model for primary recrystallization. *Acta Mater* 2016;107:366–76.
- [163] Kugler G, Turk R. Study of the influence of initial microstructure topology on the kinetics of static recrystallization using a cellular automata model. *Comput Mater Sci* 2006;37:284–91.

- [164] Popova E, Staraselski Y, Brahme A, Mishra R, Inal K. Coupled crystal plasticity probabilistic cellular automata approach to model dynamic recrystallization in magnesium alloys. *Int J Plast* 2015;66:85–102.
- [165] Salehi M, Serajzadeh S. Simulation of static recrystallization in non-isothermal annealing using a coupled cellular automata and finite element model. *Comput Mater Sci* 2012;53:145–52.
- [166] Zheng C, Xiao N, Li D, Li Y. Microstructure prediction of the austenite recrystallization during multi-pass steel strip hot rolling: a cellular automaton modeling. *Comput Mater Sci* 2008;44:507–14.
- [167] Zheng C, Raabe D. Interaction between recrystallization and phase transformation during intercritical annealing in a cold-rolled dual-phase steel: a cellular automaton model. *Acta Mater* 2013;61:5504–17.
- [168] Lan Y, Xiao N, Li D, Li Y. Mesoscale simulation of deformed austenite decomposition into ferrite by coupling a cellular automaton method with a crystal plasticity finite element model. *Acta Mater* 2005;53:991–1003.
- [169] Ding H, He Y, Liu L, Ding W. Cellular automata simulation of grain growth in three dimensions based on the lowest-energy principle. *J Cryst Growth* 2006;293:489–97.
- [170] Lan Y, Li D, Li Y. A mesoscale cellular automaton model for curvature-driven grain growth. *Metall Mater Trans B* 2006;37B:119–29.
- [171] Raghavan S, Sahay S. Modeling the grain growth kinetics by cellular automaton. *Mater Sci Eng A* 2007;445–446:203–9.
- [172] Saluja R, Narayanan R, Das S. Cellular automata finite element (CAFE) model to predict the forming of friction stir welded blanks. *Comput Mater Sci* 2012;58:87–100.
- [173] Anderson M, Grest G, Srolovitz D. Computer simulation of normal grain growth in three dimensions. *Philos Magaz B* 1989;59(3):293–329.
- [174] Radhakrishnan B, Zacharia T. Monte Carlo simulation of grain boundary pinning in the weld heat-affected zone. *Metall Mater Trans A* 1995;26(8):2123–30.
- [175] Qin R, Bhadeshia H. Phase field method. *Mater Sci Technol* 2010;26(7):803–11.
- [176] Provatas N, Elder K. Phase-field methods in materials science and engineering. John Wiley & Sons; 2011.
- [177] Boettinger WJ, Warren JA, Beckermann C, Karma A. Phase-field simulation of solidification. *Ann Rev Mater Res* 2002;32(1):163–94.
- [178] Krill III C, Chen L-Q. Computer simulation of 3-D grain growth using a phase-field model. *Acta Mater* 2002;50(12):3059–75.
- [179] Warren JA, Kobayashi R, Lobkovsky AE, Carter WC. Extending phase field models of solidification to polycrystalline materials. *Acta Mater* 2003;51(20):6035–58.
- [180] Long-Qing C. Phase-field models for microstructure evolution. *Ann Rev Mater Res* 2002;32:113.
- [181] Singer-Loginova I, Singer H. The phase field technique for modeling multiphase materials. *Rep Prog Phys* 2008;71(10):106501.
- [182] Hoetzer J, Veronika R, Rheinheimer W, Hoffmann MJ, Nestler B. Phase-field study of pore-grain boundary interaction. *J Ceram Soc Jpn* 2016;124(4):329–39.
- [183] Kim SG, Kim DI, Kim WT, Park YB. Computer simulations of two-dimensional and three-dimensional ideal grain growth. *Phys Rev E* 2006;74(6):061605.
- [184] Kim H-K, Kim SG, Dong W, Steinbach I, Lee B-J. Phase-field modeling for 3D grain growth based on a grain boundary energy database. *Model Simul Mater Sci Eng* 2014;22(3):034004.
- [185] Moelans N, Wendler F, Nestler B. Comparative study of two phase-field models for grain growth. *Comput Mater Sci* 2009;46(2):479–90.
- [186] Nestler B. A 3d parallel simulator for crystal growth and solidification in complex alloy systems. *J Cryst Growth* 2005;275(1):e273–8.
- [187] Fan D, Chen L-Q. Computer simulation of grain growth using a continuum field model. *Acta Mater* 1997;45(2):611–22.
- [188] Demirel M, Kuprat A, George D, Straub G, Rollett A. Linking experimental characterization and computational modeling of grain growth in Al-foil. *Interf Sci* 2002;10(2):137–41.
- [189] Demirel M, Kuprat A, George D, Rollett A. Bridging simulations and experiments in microstructure evolution. *Phys Rev Lett* 2003;90(1):016106.
- [190] Rios P, Dalpian T, Brandao V, Castro J, Oliveira A. Comparison of analytical grain size distributions with three-dimensional computer simulations and experimental data. *Scripta Mater* 2006;54(9):1633–7.
- [191] Aurenhammer F. Voronoi diagrams – a survey of a fundamental geometric data structure. *ACM Comput Surv (CSUR)* 1991;23(3):345–405.
- [192] Preparata FP, Shamos M. Computational geometry: an introduction. Springer Science & Business Media; 1985.
- [193] Okabe A, Boots B, Sugihara K, Chiu SN. Spatial tessellations: concepts and applications of Voronoi diagrams. John Wiley & Sons; 2000.
- [194] Ibrahimbegovic A, Delaplace A. Microscale and mesoscale discrete models for dynamic fracture of structures built of brittle material. *Comp Struct* 2003;81(12):1255–65.
- [195] Logé R, Bernacki M, Resk H, Delannay L, Digonnet H, Chastel Y, et al. Linking plastic deformation to recrystallization in metals using digital microstructures. *Philos Magaz* 2008;88(30–32):3691–712.
- [196] Xu T, Li M. Topological and statistical properties of a constrained Voronoi tessellation. *Philos Magaz* 2009;89(4):349–74.
- [197] Hitti K, Laure P, Coupeux T, Silva L, Bernacki M. Precise generation of complex statistical Representative Volume Elements (RVEs) in a finite element context. *Comput Mater Sci* 2012;61:224–38.
- [198] Lavergne F, Brenner R, Sab K. Effects of grain size distribution and stress heterogeneity on yield stress of polycrystals: a numerical approach. *Comput Mater Sci* 2013;77:387–98.
- [199] Fritzen F, Böhlke T, Schnack E. Periodic three-dimensional mesh generation for crystalline aggregates based on Voronoi tessellations. *Comput Mech* 2009;43(5):701–13.
- [200] Luther T, Könke C. Polycrystal models for the analysis of intergranular crack growth in metallic materials. *Eng Fract Mech* 2009;76(15):2332–43.
- [201] Quey R, Dawson PR, Barbe F. Large-scale 3D random polycrystals for the finite element method: generation, meshing and remeshing. *Comp Meth Appl Mech Eng* 2011;200(17):1729–45.
- [202] Bargmann S, Svendsen B, Ekh M. An extended crystal plasticity model for latent hardening in polycrystals. *Comput Mech* 2011;48(6):631–45.
- [203] Kim D-S, Chung Y-C, Kim JJ, Kim D, Yu K. Voronoi diagram as an analysis tool for spatial properties for ceramics. *J Ceram Process Res* 2002;3(3/2):150–2.
- [204] Zhang KS, Wu MS, Feng R. Simulation of microplasticity-induced deformation in uniaxially strained ceramics by 3-D Voronoi polycrystal modeling. *Int J Plast* 2005;21(4):801–34.
- [205] Coster M, Arnould X, Chermant J-L, El Moataz A, Chartier T. A microstructural model by space tessellation for a sintered ceramic: cerine. *Image Anal Stereol* 2011;24(2):105–16.
- [206] Mitić VV, Paunović V, Janković S, Pavlović V, Antolović I, Rančić D. Electronic ceramic structure within the Voronoi cells model and microstructure fractals contacts surfaces new frontier applications. *Sci Sinter* 2013;45(2):223–32.
- [207] Gao F, Stead D, Elmo D. Numerical simulation of microstructure of brittle rock using a grain-breakable distinct element grain-based model. *Comp Geotech* 2016;78:203–17.
- [208] Ghazvinian E, Diederichs M, Quey R. 3d random voronoi grain-based models for simulation of brittle rock damage and fabric-guided micro-fracturing. *J Rock Mech Geotech Eng* 2014;6(6):506–21.
- [209] Lebensohn RA, Montagnat M, Mansuy P, Duval P, Meysonnier J, Philip A. Modeling viscoplastic behavior and heterogeneous intracrystalline deformation of columnar ice polycrystals. *Acta Mater* 2009;57(5):1405–15.
- [210] Montagnat M, Castelnau O, Bons P, Faria S, Gagliardini O, Gillet-Chaulet F, et al. Multiscale modeling of ice deformation behavior. *J Struct Geol* 2014;61:78–108.
- [211] Suquet P, Mouligne H, Castelnau O, Montagnat M, Lahellec N, Grennerat F, et al. Multi-scale modeling of the mechanical behavior of polycrystalline ice under transient creep. *Proc IUTAM* 2012;3:76–90.
- [212] Williams W, Smith C. A study of grain shape in an aluminum alloy and other applications of stereoscopic microradiography. *Trans Am Inst Min Metal Engin* 1952;194(7):755–65.

- [213] Hull F. Plane section and spatial characteristics of equiaxed β -brass grains. *Mater Sci Technol* 1988;4(9):778–85.
- [214] Du Q, Faber V, Gunzburger M. Centroidal Voronoi tessellations: applications and algorithms. *SIAM Rev* 1999;41(4):637–76.
- [215] Imai H, Iri M, Murota K. Voronoi diagram in the Laguerre geometry and its applications. *SIAM J Comput* 1985;14(1):93–105.
- [216] Kumar S, Kurtz S. Simulation of material microstructure using a 3d Voronoi tessellation: Calculation of effective thermal expansion coefficient of polycrystalline materials. *Acta Metal Mater* 1994;42(12):3917–27.
- [217] Kumar S, Kurtz SK, Agarwala VK. Micro-stress distribution within polycrystalline aggregate. *Acta Mech* 1996;114(1):203–16.
- [218] Barber C, Dobkin D, Huhdanpaa H. The quickhull algorithm for convex hulls. *ACM Trans Math Softw (TOMS)* 1996;22(4):469–83.
- [219] Rycroft C. **Voro++: a three-dimensional Voronoi cell library in C++**. Lawrence Berkeley National Laboratory; 2009.
- [220] Raabe D, Zhao Z, Mao W. On the dependence of in-grain subdivision and deformation texture of aluminum on grain interaction. *Acta Mater* 2002;50(17):4379–94.
- [221] Zhao Z, Kuchnicki S, Radovitzky R, Cuitino A. Influence of in-grain mesh resolution on the prediction of deformation textures in fcc polycrystals by crystal plasticity FEM. *Acta Mater* 2007;55(7):2361–73.
- [222] Ritz H, Dawson P. Sensitivity to grain discretization of the simulated crystal stress distributions in fcc polycrystals. *Model Simul Mater Sci Eng* 2009;17(1):015001.
- [223] Kral MV, Mangan MA, Spanos G, Rosenberg RO. Three-dimensional analysis of microstructures. *Mater Character* 2000;45(1):17–23.
- [224] Adachi Y, Ojima M, Morooka S, Tomota Y. Hierarchical 3d/4d characterization on deformation behavior of austenitic and pearlitic steels. *Mater Sci Forum* 2010;638–643:2505–10.
- [225] Wang Y-T, Adachi Y, Nakajima K, Sugimoto Y. Quantitative three-dimensional characterization of pearlite spheroidization. *Acta Mater* 2010;58:4849–58.
- [226] Simonelli M. Microstructure evolution and mechanical properties of selective laser melted Ti-6Al-4v Ph.D. thesis. Loughborough University; 2014.
- [227] Barry E. Three-dimensional reconstruction of microstructures in $\alpha + \beta$ titanium alloys Master's thesis. Ohio State University; 2008.
- [228] Kato M, Ito T, Aoyama Y, Sawa K, Kaneko T, Kawase N, et al. Three-dimensional structural analysis of a block copolymer by scanning electron microscopy combined with a focused ion beam. *J Polym Sci: Part B Polym Phys* 2007;45:677–83.
- [229] Berisha B, Raemy C, Becker C, Gorji M, Hora P. Multiscale modeling of failure initiation in a ferritic-pearlitic steel. *Acta Mater* 2015;100:191–201.
- [230] Yamanaka A, Takaki T, Tomita Y. Coupled simulation of microstructural formation and deformation behavior of ferrite-pearlite steel by phase-field method and homogenization method. *Mater Sci Eng A* 2008;480:244–52.
- [231] Steinmetz P, Kellner M, Hötzer J, Dennstedt A, Nestler B. Phase-field study of the pattern formation in Al-Ag-Cu under the influence of the melt concentration. *Comput Mater Sci* 2016;121:6–13.
- [232] Yang J, Hu G, Zhang Y. Prediction of yield stress for polysynthetically twinned TiAl crystals. *Scripta Mater* 2001;45(3):293–9.
- [233] Marketz WT, Fischer FD, Clemens H. Deformation mechanisms in TiAl intermetallics - experiments and modeling. *Int J Plast* 2003;19(3):281–321.
- [234] Butzke JE, Bargmann S. Thermomechanical modelling of polysynthetically twinned TiAl crystals. *Philos Magaz* 2015;95(24):2607–26.
- [235] Schlögl SM, Fischer FD. Micromechanical modelling of TiAl intermetallics. *Comput Mater Sci* 1996;7(1–2):34–9.
- [236] Schlögl SM, Fischer FD. The role of slip and twinning in the deformation behaviour of polysynthetically twinned crystals of TiAl: a micromechanical model. *Philos Magaz A* 1997;75(3):621–36.
- [237] Schnabel J, Bargmann S. Accessing colony boundary strengthening of fully lamellar TiAl alloys via micromechanical modeling. *Materials* 2017;10(8):896.
- [238] Werwer M. Mikromechanische Modellierung des Verformungs- und Bruchverhaltens von lamellarem TiAl Ph.D. thesis. GKSS-Forschungszentrum; 2005.
- [239] Kowalczyk-Gajewska K. Micromechanical model of polycrystalline materials with lamellar substructure. *Arch Metal Mater* 2011;56(2):509–22.
- [240] Zambaldi C, Raabe D. Crystal plasticity modelling and experiments for deriving microstructure-property relationships in γ -TiAl based alloys. *J Phys: Conf Ser* 2010;240(1):012140.
- [241] Dodla S, Bertram A, Krüger M. Finite element simulation of lamellar copper-silver composites. *Comput Mater Sci* 2015;101:29–38.
- [242] Ekh M, Larjani N, Lindfeldt E. A comparison of approaches to model anisotropy evolution in pearlitic steel. In: *Proceedings of 11th world congress on computational mechanics (WCCM XI)*; 2014.
- [243] Abouridouane M, Klocke F, Lung D, Adams O. A new 3D multiphase FE model for micro cutting ferritic-pearlitic carbon steels. *Ann - Manuf Technol* 2012;61(1):71–4.
- [244] Venkatramani G, Ghosh S, Mills M. A size-dependent crystal plasticity finite-element model for creep and load shedding in polycrystalline titanium alloys. *Acta Mater* 2007;55(11):3971–86.
- [245] Brockman RA. Analysis of elastic-plastic deformation in TiAl polycrystals. *Int J Plast* 2003;19(10):1749–72.
- [246] Werwer M, Cornec A. Numerical simulation of plastic deformation and fracture in polysynthetically twinned (PST) crystals of TiAl. *Comput Mater Sci* 2000;19(1):97–107.
- [247] Venkataramani G, Deka D, Ghosh S. Crystal plasticity based FE model for understanding microstructural effects on creep and dwell fatigue in Ti-6242. *J Eng Mater Technol* 2006;128(3):356–65.
- [248] Zhang M, Zhang J, McDowell D. Microstructure-based crystal plasticity modeling of cyclic deformation of Ti-6Al-4V. *Int J Plast* 2007;23(8):1328–48.
- [249] Schaden T, Fischer FD, Clemens H, Appel F, Bartels A. Numerical modelling of kinking in lamellar γ -TiAl based alloys. *Adv Eng Mater* 2006;8(11):1109–13.
- [250] Morrissey R, Goh C-H, McDowell DL. Microstructure-scale modeling of HCF deformation. *Mech Mater* 2003;35(3):295–311.
- [251] Kabir MR, Chernova L, Bartsch M. Numerical investigation of room-temperature deformation behavior of a duplex type γ TiAl alloy using a multi-scale modeling approach. *Acta Mater* 2010;58(17):5834–47.
- [252] Roos A, Chaboche J-L, Gélébart L, Crépin J. Multiscale modelling of titanium aluminides. *Int J Plast* 2004;20(4):811–30.
- [253] Peng X, Pi W, Fan J. A microstructure-damage-based description for the size effect of the constitutive behavior of pearlitic steels. *Int J Damage Mech* 2010;19(7):821–49.
- [254] Lindfeldt E, Ekh M. Multiscale modeling of the mechanical behaviour of pearlitic steel. *Tech Mech* 2012;32:2–5.
- [255] Deka D, Joseph DS, Ghosh S, Mills MJ. Crystal plasticity modeling of deformation and creep in polycrystalline Ti-6242. *Metall Mater Trans A* 2006;37(5):1371–88.
- [256] Zambaldi C, Roters F, Raabe D. Analysis of the plastic anisotropy and pre-yielding of (γ/α_2)-phase titanium aluminide microstructures by crystal plasticity simulation. *Intermetallics* 2011;19(6):820–7.
- [257] Jeon C, Ha DJ, Kim CP, Lee S. Effects of dendrite size on tensile deformation behavior in Zr-based amorphous matrix composites containing ductile dendrites. *Metall Mater Trans A* 2012;43(10):3663–74.
- [258] Chen L-Q. Phase-field models for microstructure evolution. *Annu Rev Mater Res* 2002;32:113–40.
- [259] Gandin CA, Desbailles JL, Rappaz M, Thevoz P. A three-dimensional cellular automaton-finite element model for the prediction of solidification grain structures. *Metall Mater Trans A* 1999;30(12):3153–65.
- [260] Suzuki T, Kim MO ans SG, Kim WT. Phase-field model of dendritic growth. *J Cryst Growth* 2002;237–239:125–31.
- [261] Steinbach I. Phase-field models in materials science. *Model Simul Mater Sci Eng* 2009;17:073001.
- [262] Zhu M, Hong C. A modified cellular automaton model for the simulation of dendritic growth in solidification of alloys. *ISIJ Int* 2001;41(5):436–45.
- [263] Beltran-Sanchez L, Stefanescu D. Growth of solutal dendrites: a cellular automaton model and its quantitative capabilities. *Metall Mater Trans A* 2003;34A:367–82.
- [264] Yin H, Felicelli S, Wang L. Simulation of a dendritic microstructure with the lattice Boltzmann and cellular automaton methods. *Acta Mater* 2011;59:3124–36.

- [265] Nastac L. Numerical modeling of solidification morphologies and segregation patterns in cast dendritic alloys. *Acta Mater* 1999;47:4253–62.
- [266] Gibson LJ, Ashby MF. Cellular solids: structure and properties. Cambridge solid state science series. Cambridge University Press; 1997.
- [267] Wang L, Lau J, Thomas EL, Boyce MC. Co-continuous composite materials for stiffness, strength, and energy dissipation. *Adv Mater* 2011;23(13):1524–9.
- [268] Weissmüller J, Viswanath RN, Kramer D, Zimmer P, Würschum R, Gleiter H. Charge-induced reversible strain in a metal. *Science* 2003;300(5617):312–5.
- [269] Erlebacher J, Aziz MJ, Karma A, Dimitrov N, Sieradzki K. Evolution of nanoporosity in dealloying. *Nature* 2001;410(6827):450–3.
- [270] Okulov IV, Weissmüller J, Markmann J. Dealloying-based interpenetrating-phase nanocomposites matching the elastic behavior of human bone. *Scient Rep* 2017;7(1):20–6.
- [271] Zhang XF, Harley G, De Jonghe LC. Co-continuous metalceramic nanocomposites. *Nano Lett* 2005;5(6):1035–7. PMID: 15943438.
- [272] Utracki LA. Polymer alloys and blends. Hanser Gardner Publications; 1989.
- [273] Thomas EL, Anderson DM, Henke CS, Hoffman D. Periodic area-minimizing surfaces in block copolymers. *Nature* 1988;334(6183):598–601.
- [274] Lee J-H, Wang L, Boyce MC, Thomas EL. Periodic bicontinuous composites for high specific energy absorption. *Nano Lett* 2012;12(8):4392–6.
- [275] Al-Ketan O, Al-Rub RKA, Rowshan R. Mechanical properties of a new type of architected interpenetrating phase composite materials. *Adv Mater Technol* 2017;2(2). 1600235-n/a, 1600235.
- [276] Soyarslan C, Pradas M, Bargmann S. Effective elastic properties of 3D stochastic bicontinuous composites 2018, [submitted for publication].
- [277] Spowart JE. Automated serial sectioning for 3-D analysis of microstructures. *Scripta Mater* 2006;55(1):5–10.
- [278] Mertens J, Henderson K, Cordes N, Pacheco R, Xiao X, Williams J, et al. Analysis of thermal history effects on mechanical anisotropy of 3d-printed polymer matrix composites via in situ x-ray tomography. *J Mater Sci* 2017;52(20):12185–206.
- [279] Rösner H, Parida S, Kramer D, Volkert CA, Weissmüller J. Reconstructing a nanoporous metal in three dimensions: an electron tomography study of dealloyed gold leaf. *Adv Eng Mater* 2007;9(7):535–41.
- [280] Fujita T, Qian L, Inoke K, Erlebacher J, Chen M. Three-dimensional morphology of nanoporous gold. *Appl Phys Lett* 2008;92(25):251902.
- [281] Chen Y-T, Lo T-N, Chu YS, Yi J, Liu C-J, Wang J-Y, et al. Full-field hard X-ray microscopy below 30 nm: a challenging nanofabrication achievement. *Nanotechnology* 2008;19(39):395302.
- [282] Glover P, Mansfield P. Limits to magnetic resonance microscopy. *Rep Prog Phys* 2002;65(10):1489.
- [283] Cahn J, Hilliard J. Free energy of a nonuniform system. I. Interfacial free energy. *J Chem Phys* 1958;28(2):258–67.
- [284] Gaylord RJ, Nishidate K. Modeling nature: cellular automata simulations with Mathematica. New York: Springer-Verlag; 1996.
- [285] Zhang J, Zhou C, Wang Y, Ju L, Du Q, Chi X, et al. Extreme-scale phase field simulations of coarsening dynamics on the sunway taihu light supercomputer. In: Proceedings of the international conference for high performance computing, networking, storage and analysis. Piscataway (NJ, USA): IEEE Press; 2016. p. 34–45.
- [286] Carolan D, Chong H, Ivankovic A, Kinloch A, Taylor A. Co-continuous polymer systems: a numerical investigation. *Comput Mater Sci* 2015;98:24–33.
- [287] Ngô B-N, Roschning B, Albe K, Weissmüller J, Markmann J. On the origin of the anomalous compliance of dealloying-derived nanoporous gold. *Scripta Mater* 2017;130:74–7.
- [288] Sun X-Y, Xu G-K, Li X, Feng X-Q, Gao H. Mechanical properties and scaling laws of nanoporous gold. *J Appl Phys* 2013;113(2):023505.
- [289] Schwarz HA. *Gesammelte Mathematische Abhandlungen*. Berlin: Springer; 1933.
- [290] Schoen AH. Infinite periodic minimal surfaces without self-intersections, NASA Technical Note TN D-5541; 1970.
- [291] Massey WSA. Basic course in algebraic topology. Springer-Verlag; 1997.
- [292] Almsherqi ZA, Landt H, Kohlwein SD, Deng Y. Chapter 6 cubic membranes: the missing dimension of cell membrane organization. In: International review of cell and molecular biology. International review of cell and molecular biology, vol. 274. Academic Press; 2009. p. 275–342.
- [293] Wohlgenuth M, Yufa N, Hoffman J, Thomas EL. Triply periodic bicontinuous cubic microdomain morphologies by symmetries. *Macromolecules* 2001;34(17):6083–9.
- [294] Lambert CA, Radzilowski LH, Thomas EL. Triply periodic level surfaces as models for cubic tricontinuous block copolymer morphologies. *Philos Trans R Soc Lond A: Math, Phys Eng Sci* 1996;354(1715):2009–23.
- [295] Lin Z, Liu S, Mao W, Tian H, Wang N, Zhang N, et al. Tunable self-assembly of diblock copolymers into colloidal particles with triply periodic minimal surfaces. *Angew Chem* 2017;129(25):7241–6.
- [296] Soyarslan C, Bargmann S, Pradas M, Weissmüller J. 3D stochastic bicontinuous microstructures: generation, topology and elasticity. *Acta Mater* 2018;149:326–40. <https://doi.org/10.1016/j.actamat.2018.01.005>
- [297] Roberts A, Garboczi E. Computation of the linear elastic properties of random porous materials with a wide variety of microstructure. *Proc R Soc Lond A: Math, Phys Eng Sci* 2002;458(2021):1033–54.
- [298] Cahn JW. Phase separation by spinodal decomposition in isotropic systems. *J Chem Phys* 1965;42(1):93–9.
- [299] Teubner M. Level surfaces of gaussian random fields and microemulsions. *EPL (Europhys Lett)* 1991;14(5):403.
- [300] Lombardo BS, Keskkula H, Paul D. Influence of ABS type on morphology and mechanical properties of PC/ABS blends. *J Appl Polym Sci* 1994;54(11):1697–720.
- [301] Donald AM. The use of environmental scanning electron microscopy for imaging wet and insulating materials. *Nat Mater* 2003;2(8):511–6. <https://doi.org/10.1038/nmat898>.
- [302] Scott W. Use of phase imaging in atomic force microscopy for measurement of viscoelastic contrast in polymer nanocomposites and molecularly thick lubricant films. *Ultramicroscopy* 2003;97(1–4):151–69. [https://doi.org/10.1016/S0304-3991\(03\)00040-8](https://doi.org/10.1016/S0304-3991(03)00040-8).
- [303] Efimov AE, Tonevitsky AG, Dittrich M, Matsko NB. Atomic force microscope (AFM) combined with the ultramicrotome: a novel device for the serial section tomography and AFM/TEM complementary structural analysis of biological and polymer samples. *J Microsc* 2007;226(3):207–16. <https://doi.org/10.1111/j.1365-2818.2007.01773.x>.
- [304] Eaton P, West P. Atomic force microscopy. Oxford Univ Pr; 2010.
- [305] Chawla N, Sidhu R, Ganesh V. Three-dimensional visualization and microstructure-based modeling of deformation in particle-reinforced composites. *Acta Mater* 2006;54(6):1541–8.
- [306] Jung JM, Yoo JH, Jeong HJ, Lee S, Kim HS. Three-dimensional characterization of SiC particle-reinforced Al composites using serial sectioning tomography and thermo-mechanical finite element simulation. *Metall Mater Trans A* 2014;45(12):5679–90. <https://doi.org/10.1007/s11661-014-2520-x>.
- [307] Zankel A, Wagner J, Poelt P. Serial sectioning methods for 3D investigations in materials science. *Micron* 2014;62:66–78. <https://doi.org/10.1016/j.micron.2014.03.002>.
- [308] Trueman A, Knight S, Colwell J, Hashimoto T, Carr J, Skeldon P, et al. 3-d tomography by automated in situ block face ultramicrotome imaging using an FEG-SEM to study complex corrosion protective paint coatings. *Corr Sci* 2013;75:376–85. <https://doi.org/10.1016/j.corsci.2013.06.021>.
- [309] Ender M, Joos J, Carraro T, Ivers-Tiffée E. Three-dimensional reconstruction of a composite cathode for lithium-ion cells. *Electrochem Commun* 2011;13(2):166–8. <https://doi.org/10.1016/j.elecom.2010.12.004>.
- [310] Rodenas T, Luz I, Prieto G, Seoane B, Miro H, Corma A, et al. Metal-organic framework nanosheets in polymer composite materials for gas separation. *Nat Mater* 2014;14(1):48–55. <https://doi.org/10.1038/nmat4113>.
- [311] Sheidaei A, Baniassadi M, Banu M, Askeland P, Pahlavanpour M, Kuuttila N, et al. 3-d microstructure reconstruction of polymer nano-composite using FIB-SEM and statistical correlation function. *Compos Sci Technol* 2013;80:47–54. <https://doi.org/10.1016/j.compscitech.2013.03.001>.
- [312] Echlin MP, Straw M, Randolph S, Filevich J, Pollock TM. The TriBeam system: femtosecond laser ablation in situ SEM. *Mater Character* 2015;100:1–12. <https://doi.org/10.1016/j.matchar.2014.10.023>.

- [313] Uchic M, Groeber M, Rollett A. Automated serial sectioning methods for rapid collection of 3d microstructure data. *JOM* 2011;63(3):25–9. <https://doi.org/10.1007/s11837-011-0041-2>.
- [314] Miller MK, Kelly TF, Rajan K, Ringer SP. The future of atom probe tomography. *Mater Today* 2012;15(4):158–65.
- [315] Seol J-B, Kim Y-T, Park C-G. A brief comment on atom probe tomography applications. *Appl Microsc* 2016;46(3):127–33. <https://doi.org/10.9729/am.2016.46.3.127>.
- [316] Cairney J, Rajan K, Haley D, Gault B, Bagot P, Choi P-P, et al. Mining information from atom probe data. *Ultramicroscopy* 2015;159:324–37. <https://doi.org/10.1016/j.ultramicro.2015.05.006>.
- [317] Withers P. X-ray nanotomography. *Mater Today* 2007;10(12):26–34. [https://doi.org/10.1016/S1369-7021\(07\)70305-X](https://doi.org/10.1016/S1369-7021(07)70305-X).
- [318] Huang M, Li Y. X-ray tomography image-based reconstruction of microstructural finite element mesh models for heterogeneous materials. *Comput Mater Sci* 2013;67:63–72.
- [319] Haboub A, Bale H, Nasiatka J, Cox B, Marshall D, Ritchie R, et al. Tensile testing of materials at high temperatures above 1700 °C with in situ synchrotron X-ray micro-tomography. *Rev Scient Instrum* 2014;85(8):083702. <https://doi.org/10.1063/1.4892437>.
- [320] Krause M, Hausherr JM, Burgeth B, Herrmann C, Krenkel W. Determination of the fibre orientation in composites using the structure tensor and local X-ray transform. *J Mater Sci* 2009;45(4):888–96.
- [321] Braut R, Germaneau A, Dupré JC, Doumalin P, Mistou S, Fazzini M. In-situ analysis of laminated composite materials by x-ray micro-computed tomography and digital volume correlation. *Exp Mech* 2013;53(7):1143–51.
- [322] Madra A, Breittkopf P, Rassineux A, Trochu F. Image-based model reconstruction and meshing of woven reinforcements in composites. *Int J Numer Meth Eng*.
- [323] Emerson MJ, Jespersen KM, Dahl A, Conradsen K, Mikkelsen LP. Individual fibre segmentation from 3D X-ray computed tomography for characterising the fibre orientation in unidirectional composite materials. *Compos Part A: Appl Sci Manuf* 2017;97:83–92.
- [324] Möbus G, Inkson BJ. Nanoscale tomography in materials science. *Mater Today* 2007;10(12):18–25.
- [325] Li M, Yang YQ, Huang B, Luo X, Zhang W, Han M, et al. Development of advanced electron tomography in materials science based on TEM and STEM. *Trans Nonferrous Metals Soc China* 2014;24(10):3031–50.
- [326] Kardjilov N, Manke I, Hilger A, Strobl M, Banhart J. Neutron imaging in materials science. *Mater Today* 2011;14(6):248–56. [https://doi.org/10.1016/S1369-7021\(11\)70139-0](https://doi.org/10.1016/S1369-7021(11)70139-0).
- [327] Recur B, Younus A, Salort S, Mounaix P, Chassagne B, Desbarats P, et al. Investigation on reconstruction methods applied to 3d terahertz computed tomography. *Optics Exp* 2011;19(6):5105. <https://doi.org/10.1364/oe.19.005105>.
- [328] Eberhardt C, Clarke A. Automated reconstruction of curvilinear fibres from 3D datasets acquired by X-ray microtomography. *J Microsc* 2002;206(1):41–53. <https://doi.org/10.1046/j.1365-2818.2002.01009.x>.
- [329] Liu X, Shapiro V. Random heterogeneous materials via texture synthesis. *Comput Mater Sci* 2015;99:177–89.
- [330] Sreeranganathan A, Gokhale AM, Young P. Realistic micromechanical modeling of discontinuously reinforced composites. *Comput Mater Sci* 2010;49(2):407–13.
- [331] Coleri E, Harvey JT, Yang K, Boone JM. Development of a micromechanical finite element model from computed tomography images for shear modulus simulation of asphalt mixtures. *Construct Build Mater* 2012;30:783–93.
- [332] Bodla KK, Murthy JY, Garimella SV. Microtomography-based simulation of transport through open-cell metal foams. *Numer Heat Transfer, Part A: Appl* 2010;58(7):527–44.
- [333] Cundall PA, Strack ODL. A discrete numerical model for granular assemblies. *Géotechnique* 1979;29(1):47–65.
- [334] Williams S, Philipse A. Random packings of spheres and spherocylinders simulated by mechanical contraction. *Phys Rev E* 2003;67(5):1–9.
- [335] Visscher W, Bolsterli M. Random packing of equal and unequal spheres in two and three dimensions. *Nature* 1972;239:504–7.
- [336] Feng Y, Han K, Owen D. Filling domains with disks: an advancing front approach. *Int J Numer Meth Eng* 2003;56:699–713.
- [337] Gaiselmann G, Froning D, Tötze C, Quick C, Manke I, Lehnert W, et al. Stochastic 3d modeling of non-woven materials with wet-proofing agent. *Int J Hydrogen Energy* 2013;38(20):8448–60.
- [338] Yamamoto S, Matsuoka T. Dynamic simulation of microstructure and rheology of fiber suspensions. *Polym Eng Sci* 1996;36(19):2396–403.
- [339] Schmid CF, Switzer LH, Klingenberg DJ. Simulations of fiber flocculation: effects of fiber properties and interfiber friction. *J Rheol* 2000;44(4):781–809. <https://doi.org/10.1122/1.551116>.
- [340] Folgar F, Tucker CL. Orientation behavior of fibers in concentrated suspensions. *J Reinf Plast Compos* 1984;3(2):98–119. <https://doi.org/10.1177/073168448400300201>.
- [341] Wang J, O'Gara JF, Tucker CL. An objective model for slow orientation kinetics in concentrated fiber suspensions: theory and rheological evidence. *J Rheol* 2008;52(5):1179–200. <https://doi.org/10.1122/1.2946437>.
- [342] Phelps J, Abd El-Rahman A, Kunc V, Tucker C. A model for fiber length attrition in injection-molded long-fiber composites. *Compos Part A: Appl Sci Manuf* 2013;51:11–21.
- [343] Tseng H-C, Chang R-Y, Hsu C-H. Numerical predictions of fiber orientation and mechanical properties for injection-molded long-carbon-fiber thermoplastic composites. *Polym Compos*. <https://doi.org/10.1002/pc.24403>.
- [344] Park JM, Park SJ. Modeling and simulation of fiber orientation in injection molding of polymer composites. *Math Prob Eng* 2011;2011:1–14. <https://doi.org/10.1155/2011/105637>.
- [345] Advani SG, Tucker CL. The use of tensors to describe and predict fiber orientation in short fiber composites. *J Rheol* 1987;31(8):751–84. <https://doi.org/10.1122/1.549945>.
- [346] Müller V, Kabel M, Andrä H, Böhlke T. Homogenization of linear elastic properties of short-fiber reinforced composites – A comparison of mean field and voxel-based methods. *Int J Solids Struct* 2015;67–68:56–70. <https://doi.org/10.1016/j.ijsolstr.2015.02.030>.
- [347] Stoyan D. Simulation and characterization of random systems of hard particles. *Image Anal Stereol* 2002;1(21):41–8.
- [348] Schneider P, Eberly DH. Geometric tools for computer graphics. Morgan Kaufman; 2002.
- [349] Eberly D. 3D game engine design: a practical approach to real-time computer graphics. CRC Press; 2006.
- [350] Jaeger H, Nagel S. Physics of the granular state. *Science* 1992;255(5051):1523–31.
- [351] Eberly D. Distance between two line segments in 3D. Magic Software Inc.
- [352] Eberly D. Intersection of cylinders. Geometric Tools, Inc; 2000. p. 1–12.
- [353] Lin A, Han S-P. On the distance between two ellipsoids. *SIAM J Optim* 2002;13(1):298–308.
- [354] Biermann D, Joliet R, Michelitsch T. Distance Computation between cylinders for the design of mold temperature control systems. *Adv Comput Intell-Theory Pract, Series CI 258/08, SFB 531*. Technical University of Dortmund; 2008.
- [355] Widom B. Random sequential addition of hard spheres to a volume. *J Chem Phys* 1966;44(10):3888–94.
- [356] Feder J. Random sequential adsorption. *J Theoret Biol* 1980;87(2):237–54.
- [357] Cooper DW. Random-sequential-packing simulations in three dimensions for spheres. *Phys Rev A* 1988;38(1):522.
- [358] Böhm H, Eckschlagner A, Han W. Multi-inclusion unit cell models for metal matrix composites with randomly oriented discontinuous reinforcements. *Comput Mater Sci* 2002;25(1):42–53.
- [359] Tu S-T, Cai W-Z, Yin Y, Ling X. Numerical simulation of saturation behavior of physical properties in composites with randomly distributed second-phase. *J Compos Mater* 2005;39(7):617–31.
- [360] Kari S, Berger H, Gabbert U. Numerical evaluation of effective material properties of randomly distributed short cylindrical fibre composites. *Comput Mater Sci* 2007;39:198–204.
- [361] Schneider K, Klusemann B, Bargmann S. Automatic three-dimensional geometry and mesh generation of periodic representative volume elements for matrix-inclusion composites. *Adv Eng Softw* 2016;99:177–88.

- [362] Bailakanavar M, Liu Y, Fish J, Zheng Y. Automated modeling of random inclusion composites. *Eng Comput* 2014;30(4):609–25.
- [363] Jodrey W, Tory E. Computer simulation of close random packing of equal spheres. *Phys Rev A* 1985;32(4):2347–51.
- [364] Pathan M, Tagarielli V, Patsias S, Baiz-Villafranca P. A new algorithm to generate representative volume elements of composites with cylindrical or spherical fillers. *Compos Part B: Eng* 2017;110(Supplement C):267–78.
- [365] Balzani D, Scheunemann L, Brands D, Schröder J. Construction of two- and three-dimensional statistically similar RVEs for coupled micro-macro simulations. *Comput Mech* 2014;54(5):1269–84.
- [366] Alder BJ, Wainwright TE. Studies in molecular dynamics. II. Behavior of a small number of elastic spheres. *J Chem Phys* 1960;33(5):1439–51.
- [367] Ghossein E, Lévesque M. Random generation of periodic hard ellipsoids based on molecular dynamics: a computationally-efficient algorithm. *J Comput Phys* 2013;253:471–90.
- [368] Salnikov V, Choï D, Karamian-Surville P. On efficient and reliable stochastic generation of RVEs for analysis of composites within the framework of homogenization. *Comput Mech* 2015;55(1):1–20.
- [369] Han K, Feng Y, Owen D. Sphere packing with a geometric based compression algorithm. *Powder Technol* 2005;155(1):33–41.
- [370] Yu Y, Cui J, Han F. An effective computer generation method for the composites with random distribution of large numbers of heterogeneous grains. *Compos Sci Technol* 2008;68(12):2543–50.
- [371] Gaiselmann G, Tötze C, Manke I, Lehnert W, Schmidt V. 3D microstructure modeling of compressed fiber-based materials. *J Power Sour* 2014;257:52–64.
- [372] Harper L, Qian C, Luchoo R, Warrior N. 3D geometric modelling of discontinuous fibre composites using a force-directed algorithm. *J Compos Mater* 2016;1–17.
- [373] Islam M, Tudryn G, Picu C. Microstructure modeling of random composites with cylindrical inclusions having high volume fraction and broad aspect ratio distribution. *Comput Mater Sci* 2016;125:309–18.
- [374] Sheng P, Zhang J, Ji Z. An advanced 3D modeling method for concrete-like particle-reinforced composites with high volume fraction of randomly distributed particles. *Compos Sci Technol* 2016;134:26–35.
- [375] Wang X, Zhang M, Jivkov AP. Computational technology for analysis of 3d meso-structure effects on damage and failure of concrete. *Int J Solids Struct* 2016;80:310–33.
- [376] Catalanotti G. On the generation of RVE-based models of composites reinforced with long fibres or spherical particles. *Compos Struct* 2016;138:84–95.
- [377] Mościński J, Bargieł M, Rycerz Z, Jacobs P. The force-biased algorithm for the irregular close packing of equal hard spheres. *Molec Simul* 1989;3(4):201–12.
- [378] Bargieł M, Mościński J. C-language program for the irregular close packing of hard spheres. *Comp Phys Commun* 1991;64(1):183–92.
- [379] Maggi F, Stafford S, Jackson T, Buckmaster J. Nature of packs used in propellant modeling. *Phys Rev E* 2008;77:046107.
- [380] Benabbou A, Borouchaki H, Laug P, Lu J. Geometrical modeling of granular structures in two and three dimensions. Application to nanostructures. *Int J Numer Meth Eng* 2009;80(4):425–54.
- [381] Benabbou A, Borouchaki H, Laug P, Lu J. Numerical modeling of nanostructured materials. *Finite Elem Anal Des* 2010;46(1):165–80.
- [382] Fritzen F, Böhlke T. Periodic three-dimensional mesh generation for particle reinforced composites with application to metal matrix composites. *Int J Solids Struct* 2011;48:706–18.
- [383] Schüler T, Jänicke R, Steeb H. Nonlinear modeling and computational homogenization of asphalt concrete on the basis of XRCT scans. *Construct Build Mater* 2016;109:96–108.
- [384] Klusemann B, Svendsen B. Homogenization methods for multi-phase elastic composites: comparisons and benchmarks. *Tech Mech* 2010;30(4):374–86.
- [385] Yi I, Wiedmaier J, Schmauder S. Modeling and simulation of mechanical properties of nano particle modified polyamide 6. *J Mater Sci Chem Eng* 2015;3(1):80–7.
- [386] Ogierman W, Kokot G. A study on fiber orientation influence on the mechanical response of a short fiber composite structure. *Acta Mech* 2016;227(1):173–83.
- [387] Soni G, Singh R, Mitra M, Falzon BG. Modelling matrix damage and fibre matrix interfacial decohesion in composite laminates via a multi-fibre multi-layer representative volume element (M2RVE). *Int J Solids Struct* 2014;51(2):449–61.
- [388] Scheider I, Xiao T, Yilmaz E, Schneider G, Huber N, Bargmann S. Damage modeling of small-scale experiments on dental enamel with hierarchical microstructure. *Acta Biomater* 2015;15:244–53.
- [389] Barthelat F, Tang H, Zavattieri P, Li C-M, Espinosa H. On the mechanics of mother-of-pearl: a key feature in the material hierarchical structure. *J Mech Phys Solids* 2007;55(2):306–37.
- [390] Spaeth A. The black gold of stade. *Lufthansa Magazin* 01/2017; 2017.
- [391] Wongsto A, Li S. Micromechanical FE analysis of UD fibre-reinforced composites with fibres distributed at random over the transverse cross-section. *Compos Part A: Appl Sci Manuf* 2005;36(9):1246–66.
- [392] Dastgerdi JN, Marquis G, Salimi M. The effect of nanotubes waviness on mechanical properties of CNT/SMP composites. *Compos Sci Technol* 2013;86:164–9.
- [393] Li S. On the unit cell for micromechanical analysis of fibre-reinforced composites. *Proc R Soc A: Math, Phys Eng Sci* 1999;455(1983):815–38.
- [394] Matsuda T, Okumura D, Ohno N, Kawai M. Three-dimensional microscopic interlaminar analysis of cross-ply laminates based on a homogenization theory. *Int J Solids Struct* 2007;44(25):8274–84.
- [395] Zeman J, Šejnoha M. From random microstructures to representative volume elements. *Model Simul Mater Sci Eng* 2007;15(4):S325–35.
- [396] Gusev AA, Hine PJ, Ward IM. Fiber packing and elastic properties of a transversely random unidirectional glass/epoxy composite. *Compos Sci Technol* 2000;60(4):535–41.
- [397] Feng L, Xie N, Zhong J. Carbon nanofibers and their composites: a review of synthesizing, properties and applications. *Materials* 2014;7(5):3919–45.
- [398] Stapleton SE, Appel L, Simon J-W, Reese S. Representative volume element for parallel fiber bundles: Model and size convergence. *Compos Part A: Appl Sci Manuf* 2016;87:170–85.
- [399] Melro AR, Camanho PP, Pinho ST. Generation of random distribution of fibres in long-fibre reinforced composites. *Compos Sci Technol* 2008;68(9):2092–102.
- [400] Swolfs Y, Gorbatikh L, Verpoest I. Stress concentrations in hybrid unidirectional fibre-reinforced composites with random fibre packings. *Compos Sci Technol* 2013;85:10–6.
- [401] Romanov V, Lomov SV, Swolfs Y, Orlova S, Gorbatikh L, Verpoest I. Statistical analysis of real and simulated fibre arrangements in unidirectional composites. *Compos Sci Technol* 2013;87:126–34.
- [402] Yang L, Yan Y, Ran Z, Liu Y. A new method for generating random fibre distributions for fibre reinforced composites. *Compos Sci Technol* 2013;76:14–20.
- [403] Vaughan TJ, McCarthy CT. A combined experimental-numerical approach for generating statistically equivalent fibre distributions for high strength laminated composite materials. *Compos Sci Technol* 2010;70(2):291–7.
- [404] Wang W, Dai Y, Zhang C, Gao X, Zhao M. Micromechanical modeling of fiber-reinforced composites with statistically equivalent random fiber distribution. *Materials* 2016;9(8):624.
- [405] Lu Z, Yuan Z, Liu Q. 3D numerical simulation for the elastic properties of random fiber composites with a wide range of fiber aspect ratios. *Comput Mater Sci* 2014;90:123–9.
- [406] Monteiro SN, Lopes FPD, Ferreira AS, Nascimento DCO. Natural-fiber polymer-matrix composites: cheaper, tougher, and environmentally friendly. *JOM* 2009;61(1):17–22.

- [407] Mallick PK. Fiber-reinforced composites: materials, manufacturing, and design. CRC PR INC; 2007.
- [408] Fisher F, Bradshaw R, Brinson L. Fiber waviness in nanotube-reinforced polymer composites – I: modulus predictions using effective nanotube properties. *Compos Sci Technol* 2003;63(11):1689–703.
- [409] Nam TH, Goto K, Nakayama H, Oshima K, Premalal V, Shimamura Y, et al. Effects of stretching on mechanical properties of aligned multi-walled carbon nanotube/epoxy composites. *Compos Part A: Appl Sci Manuf* 2014;64:194–202.
- [410] Paunikaar S, Kumar S. Effect of CNT waviness on the effective mechanical properties of long and short CNT reinforced composites. *Comput Mater Sci* 2014;95:21–8.
- [411] Garnich MR, Karami G. Finite element micromechanics for stiffness and strength of wavy fiber composites. *J Compos Mater* 2004;38(4):273–92.
- [412] Shi DL, Feng XQ, Huang YY, Hwang KC. Critical evaluation of the stiffening effect of carbon nanotubes in composites. *Key Eng Mater* 2004;261:1487–92.
- [413] Shady E, Gowayed Y. Effect of nanotube geometry on the elastic properties of nanocomposites. *Compos Sci Technol* 2010;70(10):1476–81.
- [414] Stein IY, Lewis DJ, Wardle BL. Aligned carbon nanotube array stiffness from stochastic three-dimensional morphology. *Nanoscale* 2015;7(46):19426–31.
- [415] Recchia S, Zheng J, Pelegri AA. Fiberwalk: a random walk approach to fiber representative volume element creation. *Acta Mech* 2014;225(4–5):1301–12.
- [416] Herasati S, Zhang L. A new method for characterizing and modeling the waviness and alignment of carbon nanotubes in composites. *Compos Sci Technol* 2014;100:136–42.
- [417] Drücker S, Wilmers J, Bargmann S. Influence of the microstructure on effective mechanical properties of carbon nanotube composites. *Coupled Syst Mech* 2017;6(1):1–15.
- [418] Faessel M, Delisée C, Bos F, Castéra P. 3D modelling of random cellulosic fibrous networks based on X-ray tomography and image analysis. *Compos Sci Technol* 2005;65(13):1931–40.
- [419] Altendorf H, Jeulin D. Random-walk-based stochastic modeling of three-dimensional fiber systems. *Phys Rev E* 2011;83(4):041804.
- [420] Chapelle L, Lévesque M, Brøndsted P, Foldschack MR, Kusano Y. Generation of non-overlapping fiber architecture. In: *Proceedings of the 20th international conference on composite materials*; 2015.
- [421] Rouquerol J, Avnir D, Fairbridge CW, Everett DH, Haynes JM, Pernicone N, et al. Recommendations for the characterization of porous solids (technical report). *Pure Appl Chem* 2009;66(8):1739–58.
- [422] Ansar M, Xinwei W, Chouwei Z. Modeling strategies of 3d woven composites: a review. *Compos Struct* 2011;93(8):1947–63.
- [423] Fang G, Liang J. A review of numerical modeling of three-dimensional braided textile composites. *J Compos Mater* 2011;45(23):2415–36.
- [424] Barbero E, Damiani T, Trovillion J. Micromechanics of fabric reinforced composites with periodic microstructure. *Int J Solids Struct* 2005;42(9):2489–504.
- [425] Mahadik Y, Brown KR, Hallett S. Characterisation of 3d woven composite internal architecture and effect of compaction. *Compos Part A: Appl Sci Manuf* 2010;41(7):872–80.
- [426] Bale H, Blacklock M, Begley M, Marshall D, Cox B, Ritchie R. Characterizing three-dimensional textile ceramic composites using synchrotron X-ray micro-computed-tomography. *J Am Ceram Soc* 2012;95(1):392–402.
- [427] Jacques S, Baere ID, Paepegem WV. Application of periodic boundary conditions on multiple part finite element meshes for the meso-scale homogenization of textile fabric composites. *Compos Sci Technol* 2014;92:41–54.
- [428] Straumit I, Lomov SV, Wevers M. Quantification of the internal structure and automatic generation of voxel models of textile composites from X-ray computed tomography data. *Compos Part A: Appl Sci Manuf* 2015;69:150–8.
- [429] Naouar N, Vidal-Salle E, Schneider J, Maire E, Boisse P. 3D composite reinforcement meso FE analyses based on X-ray computed tomography. *Compos Struct* 2015;132:1094–104.
- [430] Barbero EJ, Trovillion J, Mayugo JA, Sikkil KK. Finite element modeling of plain weave fabrics from photomicrograph measurements. *Compos Struct* 2006;73(1):41–52.
- [431] Sevenois R, Garoz D, Gilabert F, Spronk S, Fonteyn S, Heyndrickx M, et al. Avoiding interpenetrations and the importance of nesting in analytic geometry construction for representative unit cells of woven composite laminates. *Compos Sci Technol* 2016;136:119–32.
- [432] Said BE, Ivanov D, Long A, Hallett S. Multi-scale modelling of strongly heterogeneous 3D composite structures using spatial voronoi tessellation. *J Mech Phys Solids* 2016;88:50–71.
- [433] Mahadik Y, Hallett S. Finite element modelling of tow geometry in 3d woven fabrics. *Compos Part A: Appl Sci Manuf* 2010;41(9):1192–200.
- [434] El Said B, Green S, Hallett SR. Kinematic modelling of 3d woven fabric deformation for structural scale features. *Compos Part A: Appl Sci Manuf* 2014;57:95–107.
- [435] Green S, Long A, Said BE, Hallett S. Numerical modelling of 3D woven preform deformations. *Compos Struct* 2014;108:747–56.
- [436] Green SD, Matveev MY, Long AC, Ivanov D, Hallett SR. Mechanical modelling of 3D woven composites considering realistic unit cell geometry. *Compos Struct* 2014;118:284–93.
- [437] Joglekar S, Pankow M. Modeling of 3d woven composites using the digital element approach for accurate prediction of kinking under compressive loads. *Compos Struct* 2017;160:547–59.
- [438] Badel P, Vidal-Sallé E, Boisse P. Large deformation analysis of fibrous materials using rate constitutive equations. *Comp Struct* 2008;86(11):1164–75.
- [439] Khan M, Mabrouki T, Vidal-Sallé E, Boisse P. Numerical and experimental analyses of woven composite reinforcement forming using a hypoelastic behaviour. Application to the double dome benchmark. *J Mater Process Technol* 2010;210(2):378–88.
- [440] Stig F, Hallström S. Spatial modelling of 3D-woven textiles. *Compos Struct* 2012;94(5):1495–502.
- [441] Grail G, Hirsekorn M, Wendling A, Hivet G, Hambli R. Consistent finite element mesh generation for meso-scale modeling of textile composites with preformed and compacted reinforcements. *Compos Part A: Appl Sci Manuf* 2013;55:143–51.
- [442] Daelemans L, Faes J, Allaoui S, Hivet G, Dierick M, Van Hoorebeke L, et al. Finite element simulation of the woven geometry and mechanical behaviour of a 3d woven dry fabric under tensile and shear loading using the digital element method. *Compos Sci Technol* 2016;137:177–87.
- [443] Zhou G, Sun X, Wang Y. Multi-chain digital element analysis in textile mechanics. *Compos Sci Technol* 2004;64(2):239–44.
- [444] Isart N, El Said B, Ivanov D, Hallett S, Mayugo J, Blanco N. Internal geometric modelling of 3d woven composites: a comparison between different approaches. *Compos Struct* 2015;132:1219–30.
- [445] Isart N, Mayugo J, Blanco N, Ripoll L, Sola A, Soler M. Geometric model for 3d through-thickness orthogonal interlock composites. *Compos Struct* 2015;119:787–98.
- [446] Kuhn J, Charalambides P. Modeling of plain weave fabric composite geometry. *J Compos Mater* 1999;33(3):188–220.
- [447] Lomov SV, Huysmans G, Luo Y, Parnas RS, Prodromou A, Verpoest I, et al. Textile composites: modelling strategies. *Compos Part A: Appl Sci Manuf* 2001;32(10):1379–94.
- [448] Dong W, Xiao J, Li Y. Finite element analysis of the tensile properties of 2.5 d braided composites. *Mater Sci Eng: A* 2007;457(1):199–204.
- [449] Adumitroaie A, Barbero EJ. Beyond plain weave fabrics—I. Geometrical model. *Compos Struct* 2011;93(5):1424–32.
- [450] Bednarczyk BA, Stier B, Simon J-W, Reese S, Pineda EJ. Meso-and micro-scale modeling of damage in plain weave composites. *Compos Struct* 2015;121:258–70.
- [451] Kowalczyk P. Enhanced geometric model for numerical microstructure analysis of plain-weave fabric-reinforced composite. *Adv Compos Mater* 2015;24(5):411–29.
- [452] Xiao X, Hua T, Li L, Wang J. Geometrical modeling of honeycomb woven fabric architecture. *Text Res J* 2015;85(16):1651–65.
- [453] Jendrysik N, Schneider K, Bargmann S. Automatic generation and discretization of fully periodic unit cells of plain woven composites. *J Compos Mater*, 2018 [accepted for publication].

- [454] Hivet G, Boisse P. Consistent 3D geometrical model of fabric elementary cell. Application to a meshing preprocessor for 3D finite element analysis. *Finite Elem Anal Des* 2005;42(1):25–49.
- [455] Lomov SV, Ivanov DS, Verpoest I, Zako M, Kurashiki T, Nakai H, et al. Meso-FE modelling of textile composites: road map, data flow and algorithms. *Compos Sci Technol* 2007;67(9):1870–91.
- [456] Lin H, Sherburn M, Crookston J, Long A, Clifford M, Jones I. Finite element modelling of fabric compression. *Model Simul Mater Sci Eng* 2008;16(3):035010.
- [457] Li D, Fang D, Jiang N, Xuefeng Y. Finite element modeling of mechanical properties of 3d five-directional rectangular braided composites. *Compos Part B: Eng* 2011;42(6):1373–85.
- [458] Fagianio C, Genet M, Baranger E, Ladeveze P. Computational geometrical and mechanical modeling of woven ceramic composites at the mesoscale. *Compos Struct* 2014;112:146–56.
- [459] Sonon B, Massart TJ. A level-set based representative volume element generator and XFEM simulations for textile and 3D-reinforced composites. *Materials* 2013;6(12):5568–92.
- [460] Wendling A, Hivet G, Vidal-Sallé E, Boisse P. Consistent geometrical modelling of interlock fabrics. *Finite Elem Anal Des* 2014;90:93–105.
- [461] Tabatabaei S, Lomov S. Eliminating the volume redundancy of embedded elements and yarn interpenetrations in meso-finite element modelling of textile composites. *Comp Struct* 2015;152:142–54.
- [462] Ji X, Khatri AM, Chia ES, Cha RK, Yeo BT, Joshi SC, et al. Multi-scale simulation and finite-element-assisted computation of elastic properties of braided textile reinforced composites. *J Compos Mater* 2014;48(8):931–49. <https://doi.org/10.1177/0021998313480198>.
- [463] Wang C, Zhong Y, Bernad Adaikalaraj PF, Ji X, Roy A, Silberschmidt VV, et al. Strength prediction for bi-axial braided composites by a multi-scale modelling approach. *J Mater Sci* 2016;51(12):6002–18.
- [464] Brown D, Morgan M, McIlhagger R. A system for the automatic generation of solid models of woven structures. *Compos Part A: Appl Sci Manuf* 2003;34(6):511–5.
- [465] Doitrand A, Fagianio C, Irisarri F-X, Hirsekorn M. Comparison between voxel and consistent meso-scale models of woven composites. *Compos Part A: Appl Sci Manuf* 2015;73:143–54.
- [466] Hewitt J, Brown D, Clarke R. Modelling, evaluation and manufacture of woven composite materials. *Compos Part A: Appl Sci Manuf* 1996;27(4):295–9.
- [467] Stier B, Simon J-W, Reese S. Comparing experimental results to a numerical meso-scale approach for woven fiber reinforced plastics. *Compos Struct* 2015;122:553–60.
- [468] Zhang C, Xu X. Finite element analysis of 3d braided composites based on three unit-cells models. *Compos Struct* 2013;98:130–42.
- [469] Tal D, Fish J. Generating a statistically equivalent representative volume element with discrete defects. *Compos Struct* 2016;153:791–803.
- [470] Lomov SV, Gusakov AV, Huysmans G, Prodromou A, Verpoest I. Textile geometry preprocessor for meso-mechanical models of woven composites. *Compos Sci Technol* 2000;60(11):2083–95.
- [471] Verpoest I, Lomov SV. Virtual textile composites software WiseTex: Integration with micro-mechanical, permeability and structural analysis. *Compos Sci Technol* 2005;65(15):2563–74.
- [472] Lomov SV. Modelling the geometry of textile reinforcements for composites: WiseTex. In: Boisse P, editor. *Composite reinforcements for optimum performance*. Woodhead Publishing series in composites science and engineering. Woodhead Publishing; 2011. p. 200–38.
- [473] Ha-Minh C. Numerical analysis of the ballistic performance of textile fabrics. In: Chen X, editor. *Advances fibrous composite materials for ballistic protection*. Woodhead Publishing; 2016. p. 457–500.
- [474] Lin H, Zeng X, Sherburn M, Long AC, Clifford MJ. Automated geometric modelling of textile structures. *Text Res J* 2012;82(16):1689–702.
- [475] Zeng X, Brown L, Endruweit A, Matveev M, Long A. Geometrical modelling of 3D woven reinforcements for polymer composites: Prediction of fabric permeability and composite mechanical properties. *Compos Part A: Appl Sci Manuf* 2014;56:150–60.
- [476] Russell S. *Handbook of nonwovens*. Woodhead Pub; 2007.
- [477] Hoferer J, Lehmann M, Hardy E, Meyer J, Kasper G. Highly resolved determination of structure and particle deposition in fibrous filters by MRI. *Chem Eng Technol* 2006;29(7):816–9. <https://doi.org/10.1002/ceat.200600047>.
- [478] Hosseini S, Tafreshi HV. Modeling permeability of 3-d nanofiber media in slip flow regime. *Chem Eng Sci* 2010;65(6):2249–54. <https://doi.org/10.1016/j.ces.2009.12.002>.
- [479] Shah S, Crawshaw J, Boek E. Three-dimensional imaging of porous media using confocal laser scanning microscopy. *J Microsc* 2016;265(2):261–71.
- [480] Sambaer W, Zatloukal M, Kimmer D. 3d modeling of filtration process via polyurethane nanofiber based nonwoven filters prepared by electrospinning process. *Chem Eng Sci* 2011;66(4):613–23.
- [481] Jagannathan S, Tafreshi HV, Pourdeyhimi B. A realistic approach for modeling permeability of fibrous media: 3-d imaging coupled with CFD simulation. *Chem Eng Sci* 2008;63(1):244–52.
- [482] Manickam SS, McCutcheon JR. Characterization of polymeric nonwovens using porosimetry, porometry and X-ray computed tomography. *J Memb Sci* 2012;407–408:108–15.
- [483] Soltani P, Johari MS, Zarrebini M. 3D fiber orientation characterization of nonwoven fabrics using X-ray micro-computed tomography. *World J Text Eng Technol* 2015;1:41–7.
- [484] Tausif M, Duffy B, Grishanov S, Carr H, Russell SJ. Three-dimensional fiber segment orientation distribution using X-ray microtomography. *Microsc Microanal* 2014;20(04):1294–303.
- [485] Klar A, Maringer J, Wegener R. A 3d model for fiber lay-down in nonwoven production processes. *Math Models Meth Appl Sci* 2012;22(09):1250020.
- [486] Gramsch S, Klar A, Leugering G, Marheineke N, Nessler C, Strohmeyer C, et al. Aerodynamic web forming: process simulation and material properties. *J Math Indust* 2016;6(1):13.
- [487] Wang Q, Maze B, Tafreshi HV, Pourdeyhimi B. A case study of simulating submicron aerosol filtration via lightweight spun-bonded filter media. *Chem Eng Sci* 2006;61(15):4871–83.
- [488] Mueller DH, Kochmann M. Numerical modeling of thermobonded nonwovens. *Int Nonwovens J* 2004;13(1):56–62.
- [489] Demirci E, Hou XN, Acar M, Pourdeyhimi B, Silberschmidt VV. Numerical modelling of thermally bonded nonwovens: continuous and discontinuous approaches. *Solid State Phenom* 2012;188:164–9.
- [490] Niskanen K, Alava M. Planar random networks with flexible fibers. *Phys Rev Lett* 1994;73(25):3475–8.
- [491] Torquato S. Random heterogeneous media: microstructure and improved bounds on effective properties. *Appl Mech Rev* 1991;44(2):37–76.
- [492] Wilmers J, McBride A, Bargmann S. Interface elasticity effects in polymer-filled nanoporous metals. *J Mech Phys Solids* 2017;99:163–77.
- [493] Alkemper J, Voorhees PW. Quantitative serial sectioning analysis. *J Microsc* 2001;201(3):388–94.
- [494] Maire Éric, Adrien J, Petit C. Structural characterization of solid foams. *Comp Rend Phys* 2014;15(8–9):674–82.
- [495] Maire E, Fizek A, Salvo L, Dendievel R, Youssef S, Cloetens P, et al. X-ray tomography applied to the characterization of cellular materials. Related finite element modeling problems. *Compos Sci Technol* 2003;63(16):2431–43.
- [496] Youssef S, Maire E, Gaertner R. Finite element modelling of the actual structure of cellular materials determined by X-ray tomography. *Acta Mater* 2005;53(3):719–30.
- [497] McDonald SA, Mummery PM, Johnson G, Withers PJ. Characterization of the three-dimensional structure of a metallic foam during compressive deformation. *J Microsc* 2006;223(2):150–8.
- [498] Mayer J, Giannuzzi LA, Kamino T, Michael J. TEM sample preparation and FIB-induced damage. *MRS Bull* 2007;32(05):400–7.
- [499] Sun Y, Balk TJ. A multi-step dealloying method to produce nanoporous gold with no volume change and minimal cracking. *Scripta Mater* 2008;58(9):727–30.

- [500] Körner C, Thies M, Hofmann T, Thürey N, Rüde U. Lattice Boltzmann model for free surface flow for modeling foaming. *J Statist Phys* 2005;121(1–2):179–96.
- [501] Seol D, Hu S, Li Y, Shen J, Oh K, Chen L. Computer simulation of spinodal decomposition in constrained films. *Acta Mater* 2003;51(17):5173–85.
- [502] Farkas D, Caro A, Bringa E, Crowson D. Mechanical response of nanoporous gold. *Acta Mater* 2013;61(9):3249–56.
- [503] Saane S, Mangipudi K, Loos K, Hosson JD, Onck P. Multiscale modeling of charge-induced deformation of nanoporous gold structures. *J Mech Phys Solids* 2014;66:1–15.
- [504] Fujita T, Guan P, McKenna K, Lang X, Hirata A, Zhang L, et al. Atomic origins of the high catalytic activity of nanoporous gold. *Nat Mater* 2012;11:775–80.
- [505] Xia R, Wu RN, Liu YL, Sun XY. The role of computer simulation in nanoporous metals a review. *Materials* 2015;8(8):5060–83.
- [506] Erlebacher J, McCue I. Geometric characterization of nanoporous metals. *Acta Mater* 2012;60(17):6164–74.
- [507] Erlebacher J. An atomistic description of dealloying: porosity evolution, the critical potential, and rate-limiting behavior. *J Electrochem Soc* 2004;151(10):C614–26.
- [508] Zinchenko O, Raedt HD, Detsi E, Onck P, Hosson JD. Nanoporous gold formation by dealloying: a metropolis Monte Carlo study. *Comp Phys Commun* 2013;184(6):1562–9.
- [509] Krekeler T, Straer AV, Graf M, Wang K, Hartig C, Ritter M, et al. Silver-rich clusters in nanoporous gold. *Mater Res Lett* 2017;5:1–8.
- [510] Oono Y, Puri S. Study of phase-separation dynamics by use of cell dynamical systems. I. Modeling. *Phys Rev A* 1988;38(1):434–53.
- [511] Puri S, Oono Y. Study of phase-separation dynamics by use of cell dynamical systems. II. two-dimensional demonstrations. *Phys Rev A* 1988;38(3):1542–65.
- [512] do Rosário J, Berger J, Lilleodden E, McMeeking R, Schneider G. The stiffness and strength of metamaterials based on the inverse opal architecture. *Extreme Mech Lett* 2017;12:86–96.
- [513] Silberschmidt V, Matveenko V. *Mechanics of advanced materials: analysis of properties and performance, engineering materials*. Springer International Publishing; 2015.
- [514] Lakes R. Foam structures with a negative Poisson's ratio. *Science* 1987;235(4792):1038–41.
- [515] Babae S, Shim J, Weaver J, Chen E, Patel N, Bertoldi K. 3D soft metamaterials with negative Poisson's ratio. *Adv Mater* 2013;25(36):5044–9.
- [516] Shim J, Perdigou C, Chen ER, Bertoldi K, Reis PM. Buckling-induced encapsulation of structured elastic shells under pressure. *Proc Nat Acad Sci* 2012;109(16):5978–83.
- [517] Shen J, Zhou S, Huang X, Xie YM. Simple cubic three-dimensional auxetic metamaterials. *Phys Status Solidi (b)* 2014;251(8):1515–22.
- [518] Ren X, Shen J, Ghaedizadeh A, Tian H, Xie YM. Experiments and parametric studies on 3D metallic auxetic metamaterials with tuneable mechanical properties. *Smart Mater Struct* 2015;24(9):095016.
- [519] Bückmann T, Schittny R, Thiel M, Kadic M, Milton G, Wegener M. On three-dimensional dilational elastic metamaterials. *New J Phys* 2014;16(3):033032.
- [520] Milton G. Complete characterization of the macroscopic deformations of periodic unimode metamaterials of rigid bars and pivots. *J Mech Phys Solids* 2013;61(7):1543–60.
- [521] Fu M, Chen Y, Zhang W, Zheng B. Experimental and numerical analysis of a novel three-dimensional auxetic metamaterial. *Phys Status Solidi (b)* 2016;253(8):1565–75.
- [522] Lim T-C. A 3D auxetic material based on intersecting double arrowheads. *Phys Status Solidi (b)* 2016;253(7):1252–60.
- [523] Cabras L, Brun M. A class of auxetic three-dimensional lattices. *J Mech Phys Solids* 2016;91:56–72.
- [524] Thomson W. On the division of space with minimum partitioned area. *Acta Math* 1887;11:121–34.
- [525] Weaire D, Phelan R. A counter-example to Kelvin's conjecture on minimal surfaces. *Philos Magaz Lett* 1994;69(2):107–10.
- [526] Gibson LJ, Ashby MF. The mechanics of three-dimensional cellular materials. *Proc R Soc Lond A: Math, Phys Eng Sci* 1982;382(1782):43–59.
- [527] Pia G, Delogu F. On the elastic deformation behavior of nanoporous metal foams. *Scripta Mater* 2013;69(11):781–4.
- [528] Liu R, Antoniou A. A relationship between the geometrical structure of a nanoporous metal foam and its modulus. *Acta Mater* 2013;61(7):2390–402.
- [529] Soyarslan C, Husser E, Bargmann S. Effect of surface elasticity on the elastic response of nanoporous gold. *J Nanomech Micromech* 2017;7(4):04017013.
- [530] Huber N, Viswanath RN, Mameka N, Markmann J, Weissmüller J. Scaling laws of nanoporous metals under uniaxial compression. *Acta Mater* 2014;67:252–65.
- [531] Roschning B, Huber N. Scaling laws of nanoporous gold under uniaxial compression: effects of structural disorder on the solid fraction, elastic Poisson's ratio, Young's modulus and yield strength. *J Mech Phys Solids* 2016;92:55–71.
- [532] Stavans J. The evolution of cellular structures. *Rep Prog Phys* 1993;56(6):733.
- [533] Glazier JA, Weaire D. The kinetics of cellular patterns. *J Phys: Cond Matter* 1992;4(8):1867.
- [534] Roberts A, Garboczi E. Elastic moduli of model random three-dimensional closed-cell cellular solids. *Acta Mater* 2001;49(2):189–97.
- [535] Mangipudi K, Onck P. Multiscale modelling of damage and failure in two-dimensional metallic foams. *J Mech Phys Solids* 2011;59(7):1437–61.
- [536] Beckmann C, Hohe J. Assessment of material uncertainties in solid foams based on local homogenization procedures. *Int J Solids Struct* 2012;49(19–20):2807–22.
- [537] Redenbach C, Shklyar I, Andrä H. Laguerre tessellations for elastic stiffness simulations of closed foams with strongly varying cell sizes. *Int J Eng Sci* 2012;50(1):70–8.
- [538] Sonon B, Francois B, Massart TJ. An advanced approach for the generation of complex cellular material representative volume elements using distance fields and level sets. *Comput Mech* 2015;56(2):221–42.
- [539] Berk N. Scattering properties of the leveled-wave model of random morphologies. *Phys Rev A* 1991;44(8):5069–79.
- [540] Gurson A. Continuum theory of ductile rupture by void nucleation and growth: part I – yield criteria and flow rules for porous ductile media. *J Eng Mater Technol* 1977;99(1):2–15.
- [541] Tvergaard V. Influence of voids on shear band instabilities under plane strain conditions. *Int J Fract* 1981;17(4):389–407.
- [542] Needleman A. A continuum model for void nucleation by inclusion debonding. *J Appl Mech* 1987;54(3):525–31.
- [543] Sopp D, Soyarslan C, Sarac B, Bargmann S, Stoica M, Eckert J. Structure-property relationships in nanoporous metallic glasses. *Acta Mater* 2016;106:199–207.
- [544] Javid F, Wang P, Shanian A, Bertoldi K. Architected materials with ultra-low porosity for vibration control. *Adv Mater* 2016;28(28):5943–8.
- [545] Weck A, Wilkinson D, Maire E, Toda H. Visualization by X-ray tomography of void growth and coalescence leading to fracture in model materials. *Acta Mater* 2008;56(12):2919–28.
- [546] Millett P, Tonks M. Application of phase-field modeling to irradiation effects in materials. *Curr Opin Solid State Mater Sci* 2011;15(3):125–33.
- [547] Bacon D, Gao F, Ossetsky Y. The primary damage state in fcc, bcc and hcp metals as seen in molecular dynamics simulations. *J Nucl Mater* 2000;276(13):1–12.
- [548] Millett PC, Rokkam S, El-Azab A, Tonks M, Wolf D. Void nucleation and growth in irradiated polycrystalline metals: a phase-field model. *Model Simul Mater Sci Eng* 2009;17(6):064003.
- [549] Hu S, H Jr CH. Phase-field modeling of void lattice formation under irradiation. *J Nucl Mater* 2009;394(2–3):155–9.
- [550] Sonedá N, Ishino S, Takahashi A, Dohi K. Modeling the microstructural evolution in bcc-Fe during irradiation using kinetic Monte Carlo computer simulation. *J Nucl Mater* 2003;323(23):169–80.
- [551] Domain C, Becquart C, Malerba L. Simulation of radiation damage in Fe alloys: an object kinetic Monte Carlo approach. *J Nucl Mater* 2004;335(1):121–45.

- [552] Guessasma S, Valle GD. Generation of anisotropic cellular solid model and related elasticity parameters: Finite element simulation. *J Cell Plast* 2009;45(2):119–36.
- [553] Paterson MS. Deformation mechanisms: granular flow. Netherlands (Dordrecht): Springer; 2013. p. 209–43.
- [554] Hamilton EL. Variations of density and porosity with depth in deep-sea sediments. *J Sediment Res* 1976;46(2):280–300.
- [555] Thevanayagam S, Martin GR. Liquefaction in silty soils – screening and remediation issues. *Soil Dynam Earthq Eng* 2002;22(9):1035–42.
- [556] Bentz D, Stutzman P. SEM analysis and computer modelling of hydration of Portland cement particles, ASTM STP 1215. In: DeHayes S, Stark D, editors. *Petrography of cementitious materials*; 1993. p. 60–73.
- [557] Isola R. Packing of granular materials Ph.D. thesis. The University of Nottingham; 2008.
- [558] Zhao D, Nezami EG, Hashash YM, Ghaboussi J. Three-dimensional discrete element simulation for granular materials. *Eng Comput* 2006;23(7):749–70.
- [559] Winkler P, Sadaghiani MS, Jentsch H, Witt K. Granular packing generation using DEM - modified force-biased-algorithm. *Scour Eros* 2014;345–9.
- [560] González-Montellano C, Ayuga F, Ooi JY. Discrete element modelling of grain flow in a planar silo: influence of simulation parameters. *Granul Matter* 2011;13(2):149–58.
- [561] He D, Ekere N, Cai L. Computer simulation of random packing of unequal particles. *Phys Rev E* 1999;60(6):7098.
- [562] Lee Y, Fang C, Tsou Y-R, Lu L-S, Yang C-T. A packing algorithm for three-dimensional convex particles. *Granul Matter* 2009;11(5):307–15.
- [563] Stroeven M, Askes H, Sluys L. Numerical determination of representative volumes for granular materials. *Comp Meth Appl Mech Eng* 2004;193(30):3221–38.
- [564] Atwater MA, Darling KA, Tschopp MA. Synthesis, characterization and quantitative analysis of porous metal microstructures: application to microporous copper produced by solid state foaming. *AIMS Mater Sci* 2016;3(2):573–90.
- [565] Liberato M, Kogikoski S, Da Silva E, De Araujo D, Guha S, Alves W. Polycaprolactone fibers with self-assembled peptide micro/nanotubes: a practical route towards enhanced mechanical strength and drug delivery applications. *J Mater Chem B* 2016;4(8):1405–13.
- [566] Kerschnitzki M, Kollmannsberger P, Burghammer M, Duda G, Weinkamer R, Wagermaier W, Fratzl P. Architecture of the osteocyte network correlates with bone material quality. *J Bone Min Res* 2013;28(8):1837–45.
- [567] Soyarslan C, Argeso H, Bargmann S. Skeletonization-based beam-FE models for stochastic bicontinuous materials: Application to simulations of nanoporous gold; 2018 [submitted for publication].
- [568] Bostanabad R, Zhang Y, Burghammer X, Li M, Kearney T, Brinson LC, Apley DW, Liu WK, Chen W. Computational microstructure characterization and reconstruction: Review of the state-of-the-art techniques. *Prog Mater Sci* 2018;95:1–41.